

SIMULATION OF ANEURYSM HEMODYNAMICS TO PREDICT
INTRALUMINAL THROMBUS FORMATION REGION

A THESIS SUBMITTED TO
THE GRADUATE SCHOOL OF NATURAL AND APPLIED SCIENCES
OF
MIDDLE EAST TECHNICAL UNIVERSITY

BY

BURCU RAMAZANLI

IN PARTIAL FULFILLMENT OF THE REQUIREMENTS
FOR
THE DEGREE OF DOCTOR OF PHILOSOPHY
IN
MECHANICAL ENGINEERING

DECEMBER 2022

Approval of the thesis:

**SIMULATION OF ANEURYSM HEMODYNAMICS TO PREDICT
INTRALUMINAL THROMBUS FORMATION REGION**

submitted by **BURCU RAMAZANLI** in partial fulfillment of the requirements for
the degree of **Doctor of Philosophy in Mechanical Engineering, Middle East
Technical University** by,

Prof. Dr. Halil Kalıpçılar
Dean, Graduate School of **Natural and Applied Sciences**

Prof. Dr. M. A. Sahir Arıkan
Head of the Department, **Mechanical Engineering**

Prof. Dr. Mehmet Metin Yavuz
Supervisor, **Mechanical Engineering, METU**

Prof. Dr. Cüneyt Sert
Co-Supervisor, **Mechanical Engineering, METU**

Examining Committee Members:

Assoc. Prof. Dr. Özgür Bayer
Mechanical Engineering, METU

Prof. Dr. Mehmet Metin Yavuz
Mechanical Engineering, METU

Prof. Dr. Selin Aradağ Çelebioğlu
Mechanical Engineering, TED University

Assist. Prof. Dr. Özgür Uğraş Baran
Mechanical Engineering, METU

Assist. Prof. Dr. Hüseyin Enes Salman
Mechanical Engineering, TOBB-ETÜ University

Date: 02.12.2022

I hereby declare that all information in this document has been obtained and presented in accordance with academic rules and ethical conduct. I also declare that, as required by these rules and conduct, I have fully cited and referenced all material and results that are not original to this work.

Name Last name : Burcu Ramazanlı

Signature :

ABSTRACT

SIMULATION OF ANEURYSM HEMODYNAMICS TO PREDICT INTRALUMINAL THROMBUS FORMATION REGION

Ramazanlı, Burcu
Doctor of Philosophy, Mechanical Engineering
Supervisor: Prof. Dr. Mehmet Metin Yavuz
Co-Supervisor: Prof. Dr. Cüneyt Sert

December 2022, 149 pages

Intraluminal thrombus (ILT) is a fibrin structure which might affect rupture characteristics and be observed 80% of abdominal aortic aneurysms (AAA). Disturbed hemodynamics inside AAA might affect ILT formation, that are generally quantified by wall shear stress (WSS) parameters in literature. Together with WSS parameters, vortex structures observed inside arterial systems can also be counted as indicators of disturbed hemodynamics, and might contribute the generation of ILT. To understand the effect of disturbed hemodynamics on ILT formation, blood flow through AAAs can be simulated by using computational methods. In computational models, setting up inlet boundary conditions (BC) and fluid properties are very important steps which affect the reliability and accuracy of the hemodynamic assessment. The aim of this study is understanding the effect of inlet boundary conditions and rheology model selection on predicting the WSS parameters and vortex structures, and determining a correlation between those hemodynamic parameters.

To understand the effect of inlet different BCs on hemodynamic parameters, *Womersley*, *Parabolic* and *Plug* velocity profiles, with different entrance lengths, $L_{ent} = D, 3D$ and $11D$, are examined. Results reveal that *Parabolic* profile even with a short entrance length can be utilized instead of complex *Womersley* profile. To investigate the effect of inlet flow waveform pattern on rheology model selection, three waveform patterns, Base, Case 1 and 2, are tested for eight viscous shear thinning models, along with the viscoelastic Oldroyd-B and Newtonian models. Newtonian model might obtain different OSI and ECAP distributions from shear-thinning models even for high mean flow rates, albeit the differences introduced by elasticity might be negligible. Also, vortex transport mechanism might affect the rheology model selection. To observe the correlation between WSS parameters and vortex structures, time-averaged wall shear stress (TAWSS), oscillatory shear index (OSI), endothelial cell activation potential (ECAP) and relative residence time (RRT) distributions and contours of time-averaged $\overline{\lambda_{ci}}$ -criterion, \overline{Q} -criterion and $\overline{\lambda_2}$ -criterion are plotted. Regions with high $|\overline{\lambda_{ci}}|$, $|\overline{\lambda_2}|$ and $|\overline{Q}|$ are correlated with high TAWSS and low OSI, ECAP and RRT. To conclude, vortex identification methods have the potential to be utilized to predict ILT accumulation and rupture sites.

Keywords: Intraluminal thrombus formation, Womersley profile, Blood rheology, Wall shear stress parameters, Vortex identification methods.

ÖZ

İNTRALÜMİNAL TROMBÜS OLUŞUM BÖLGESİNİ ÖNGÖRMEK İÇİN ANEVİZMA HEMODİNAMİĞİNİN SİMÜLASYONU

Ramazanlı, Burcu
Doktora, Makina Mühendisliği
Tez Yöneticisi: Prof. Dr. Mehmet Metin Yavuz
Ortak Tez Yöneticisi: Prof. Dr. Cüneyt Sert

Aralık 2022, 149 sayfa

İntraluminal trombus (ILT), abdominal aort anevrizmalarının (AAA) %80'inde görülen ve anevrizma rüptürünü tetikleyebilen bir fibrin yapısıdır. AAA içindeki bozulmuş hemodinamikler, literatürde genellikle duvar kesme gerilimi (WSS) parametreleriyle nicelenir ve ILT oluşumunu etkileyebilir. WSS parametreleri ile birlikte, arteriyel sistemlerde gözlenen vorteks yapıları da bozulmuş hemodinamiğin göstergeleri olarak sayılabilir ve onlar da ILT oluşumuna katkıda bulunabilir. Bozulmuş hemodinamiğin ILT oluşumu üzerindeki etkisini anlamak için, hesaplamalı yöntemler kullanılarak AAA'ların içerisindeki kan akışı simüle edilebilir. Hesaplamalı modellerde sınır koşullarının (BC) ve sıvı özelliklerinin ayarlanması hemodinamik değerlendirmenin güvenilirliğini ve doğruluğunu etkileyen çok önemli adımlardır. Bu çalışmanın amacı, giriş sınır koşullarının ve reoloji model seçiminin WSS parametrelerini ve vorteks yapılarını tahmin etme üzerindeki etkisini anlamak ve bu parametre ve yapılar arasında bir korelasyon belirlemektir.

Bu çalışmada, farklı giriş uzunluklarına sahip geometrilere ($L_{ent} = D, 3D$ and $11D$) idealleştirilmiş sınır koşulları (*Womersley*, *Parabolik* ve *Plug*) karşılaştırılarak incelenmiştir. Sonuçlar, karmaşık Womersley profili yerine kısa bir giriş uzunluğunda bile Parabolik profilin kullanılabilceğini ortaya koymaktadır. Giriş akış dalga biçimi modelinin reoloji modeli seçimi üzerindeki etkisini araştırmak için, üç dalga biçimi modeli, Temel, Durum 1 ve 2, viskoelastik Oldroyd-B ve Newton modelleriyle birlikte sekiz viskoz kayma inceltme modeli için test edilmiştir. Sonuçlar, Newtonyen modelin, yüksek ortalama akış hızları için bile kayma inceltme modellerinden farklı OSI ve ECAP dağılımları elde edebileceğini, ancak esnekliğin getirdiği farkların ihmal edilebilir düzeyde olabileceğini göstermektedir. Ayrıca girdap taşıma mekanizması reoloji modeli seçimini etkileyebilir. WSS parametreleri ve girdap yapıları arasındaki ilişkiyi gözlemlemek için, zaman ortalamalı duvar kesme gerilimi (TAWSS), salınımlı kesme indeksi (OSI), endotel hücre aktivasyon potansiyeli (ECAP) ve bağıl kalma süresi (RRT) dağılımları zaman ortalamalı $\overline{\lambda_{ci}}$ -kriteri, \overline{Q} - kriteri and $\overline{\lambda_2}$ - kriteri konturlarıyla kıyaslanmıştır. Yüksek $|\overline{\lambda_{ci}}|$, $|\overline{\lambda_2}|$ ve $|\overline{Q}|$ olan bölgeler, yüksek TAWSS ve düşük OSI, ECAP ve RRT ile ilişkilidir. Sonuç olarak, girdap tanımlama yöntemleri, ILT oluşumunu ve rüptür bölgelerini tahmin etmek için kullanılma potansiyeline sahiptir.

Anahtar Kelimeler: İntralüminal trombüs oluşumu, Womersley profili, Kan reolojisi, Duvar kesme gerilmesi parametreleri, Girdap tanımlama metotları.

To my painful losses, my dears,
Şaban Sarıçakır and Prof. Dr. Mehemmedeli Ramazanov

and

To my dearest, my son,
Muhammet Ali Ramazanlı

ACKNOWLEDGMENTS

I would like to express my sincere gratitude to my thesis supervisors, Prof. Dr. Mehmet Metin Yavuz and Prof. Dr. Cüneyt Sert, for their guidance, support and distinguished supervision throughout these years.

As well, I am very grateful to my committee members, Assoc. Prof. Dr. Özgür Bayer, Prof. Dr. Selin Aradağ Çelebioğlu, Assist. Prof. Dr. Özgür Uğraş Baran and Assist. Prof. Dr. Hüseyin Enes Salman for their valuable suggestions and spending time to my study.

My deepest gratitude goes to my husband Ahmet Ramazanlı. I would like to express my endless appreciation and thanks to him for being in my life and for taking care of me through hard times. Also, I am very grateful to my parents, Emir Sultan Karagöz and Mustafa Karagöz, for their great supports throughout my life and my brother Melih Karagöz, for his love and belief. Also, my deepest gratitude and love go to my grandparents Necla Sarıçakır and Şaban Sarıçakır, who have a great effort and guidance from my childhood to this day. Without their existence and love, I could not reach to these years. I am so thankful to my parents-in-law, Dr. Zekiye Panahova and Prof. Dr. Mehemmedeli Ramazanov, also my brother-in-law Dr. İlqar Ramazanlı for their endless support and love. Also, I want to express my gratitude to Dr. Zemine Panahova and Dr. Panah Panahlı for their guidance and motivational approach throughout my study.

Throughout this Ph.D. journey, I have lost two wonderful people, my grandfather Şaban Sarıçakır and my father-in-law Prof. Dr. Mehemmedeli Ramazanov. Rest in peace. No matter how painful your absence is, I will cherish what you left us for the rest of my life.

Together with these painful losses, at the beginning of my thesis study, a very dear person, who is my son Muhammet Ali Ramazanlı was born. I am very thankful to you, my dearest, for giving me strength and helping me to find myself since the day that you were born.

I would like to thank my dears Aslı Gülbike Uluyurt, Hülya Uluyurt, Abdullah Uluyurt and Bilge Tunçel for their love, belief, support and endless hospitality. I am very thankful to my friends from Mechanical Engineering Department, Dr. Cihat Duru and Kayacan Kestel for their support and friendship. Moreover, I would like to thank to Dr. Kamil Özden and Assist. Prof. Dr. Hüseyin Enes Salman for their guidance and support during the first years of my Ph.D. Their positive feedbacks encouraged me all through this work. Also, I am very grateful to Assist. Prof. Dr. Özgür Uğraş Baran and Assist. Prof. Dr. Ali Karakuş for their valuable advices, guidance and support throughout my thesis study.

Computing resources used in this work were provided by the National Center for High Performance Computing of Turkey (UHcM) under grant number 4007212019.

TABLE OF CONTENTS

ABSTRACT	v
ÖZ.....	viii
ACKNOWLEDGMENTS	x
TABLE OF CONTENTS	xii
LIST OF TABLES	xv
LIST OF FIGURES	xvi
LIST OF ABBREVIATIONS	xx
LIST OF SYMBOLS.....	xxi
CHAPTERS	
1 INTRODUCTION	1
1.1 Motivation of the Study	9
1.2 Aim of the Study.....	10
1.3 Structure of the Thesis	11
2 LITERATURE REVIEW	13
2.1 Computational investigation of hemodynamics of AAAs	15
2.1.1 Geometry of the problem.....	15
2.1.2 Generation of Patient Specific Model Geometry	18
2.1.3 Boundary Conditions.....	20
2.1.4 Modeling non-Newtonian fluid viscosity	26

2.1.5	Important hemodynamic parameters.....	28
2.2	Experimental studies on hemodynamics of AAAs	30
3	METHODOLOGY	37
3.1	Numerical Simulation Details	37
3.1.1	Effect of Inlet Velocity Profile and Entrance Length Study	37
3.1.2	Effect of Infrarenal Flow Waveform Pattern on Rheology Model Selection and AAA Hemodynamics Study	46
3.1.3	Correlation between vortex identification methods and wall shear stress parameters study	54
3.2	WSS Parameters and Vortex Identification Techniques	59
3.3	Validation of Numerical Model and 2D/3D Model Comparison.....	60
4	EFFECT OF INLET VELOCITY PROFILE AND ENTRANCE LENGTH ON ABDOMINAL AORTIC ANEURYSM HEMODYNAMICS	63
4.1	Results	63
4.2	Discussion	72
5	EFFECT OF INFRARENAL FLOW WAVEFORM PATTERN ON RHEOLOGY MODEL SELECTION AND ABDOMINAL AORTIC ANEURYSM HEMODYNAMICS	73
5.1	Results	73
5.2	Discussion	84
6	A CORRELATION BETWEEN WALL SHEAR STRESS PARAMETERS AND VORTEX IDENTIFICATION METHODS	89
6.1	Results	89

6.2 Discussion.....	97
7 CONCLUSION	101
REFERENCES	107
APPENDICES	
A. APPENDIX A.....	10725
B. APPENDIX B	10731
C. APPENDIX C	10733
D. APPENDIX D.....	10736
CURRICULUM VITAE	14747

LIST OF TABLES

TABLES

Table 3.1. Aneurysm models with respect to entrance lengths and applied inlet velocity profiles	39
Table 3.2. Phases of cardiac cycle with period $T = 1$ s.....	41
Table 3.3. Selected shear-thinning rheology models	50

LIST OF FIGURES

FIGURES

Figure 1.1. Magnetic resonance imaging of an abdominal aortic aneurysm (AAA).	2
Figure 1.2. A comparison of measured physiological infrarenal flow rate during rest for two different patients (Les et al., 2010)	8
Figure 2.1. Six different patient-specific medical images and corresponding reconstructed AAA geometries (Les et al., 2010).	17
Figure 2.2. Main geometric parameters for a patient-specific AAA geometry. (Soudah et al., 2013).	18
Figure 2.3. Reconstruction procedure for a patient-specific AAA model (Les et al., 2010).	20
Figure 2.4. Waveforms of applied boundary conditions (a) Sample inlet flow velocity profile. (b) Sample outlet pressure profile (Scotti et al., 2008).	21
Figure 2.5. Womersley velocity profiles in a dog’s femoral artery (Womersley et al., 1957).	24
Figure 2.6. Blood viscosity vs. shear rate. The percentage of hematocrit is in the range of 33 - 45 (Cho and Kensey, 1991).	27
Figure 2.7. TAWSS, OSI and ECAP contour plots on a patient specific AAA model (Kelsey et al., 2016)).	30
Figure 3.1. Sectional views of flow domains for aneurysm models, which is out of scale. Flow is from left to right.	38
Figure 3.2. a. Physiological inlet flow rate waveforms for $Rem = 340$ and 1160 , from left to right, respectively b. Womersley velocity profiles for those waveforms at selected time instants (Finol and Amon, 2001)	40
Figure 3.3. Four meshes generated for mesh independency check	44

Figure 3.4. a. Axial velocity profiles obtained with four different meshes at $x/LB = 0.5$, and swirling strength contours, b. OSI and ECAP distributions of four meshes for $Rem = 1160$	45
Figure 3.5. a. 2D axisymmetric flow domain, b. Physiological inlet flow rate waveform patterns, Base (Finol and Amon, 2001), Case 1 and 2.....	48
Figure 3.6. Four meshes used for the mesh independence check	52
Figure 3.7. a. Axial velocity profiles obtained with four different meshes at $x/LB = 0.5$, and swirling strength contours, b. OSI and ECAP distributions of four meshes for Case 2	53
Figure 3.8. a. 2D axisymmetric flow domains for aneurysm models with three different bulge radii, b. Physiological inlet flow rate waveform (Finol and Amon, 2001)	55
Figure 3.9. Four meshes used for the mesh independence check	57
Figure 3.10. Axial velocity profiles obtained with four different meshes $x/LB = 0.5$, and swirling strength contours	58
Figure 3.11. a. Comparison of the normalized axial velocity profile with results of Stamatopoulos et al. (2010) for a steady inlet velocity, b. Comparison of the streamline patterns of different time instants with results of Ohtaroglu (2020), c. Comparison of the axial velocity profiles of 2D axisymmetric and 3D geometries at $x/LB = 0.5$ at $t = 0.3$ sec.....	62
Figure 4.1. Comparison of time-averaged axial velocity profiles obtained by different inlet velocity profiles and entrance lengths for $Rem = 340$	65
Figure 4.2. Comparison of time-averaged axial velocity profiles obtained by different inlet velocity profiles and entrance lengths for $Rem = 1160$	67
Figure 4.3. Comparison of OSI distributions obtained by different inlet velocity profiles and entrance lengths for $Rem = 340$ and 1160, from left to right, respectively	68

Figure 4.4. Comparison of ECAP distributions obtained by different inlet velocity profiles and entrance lengths for $Rem = 340$ and 1160 , from left to right, respectively.....	69
Figure 4.5. Comparison of instantaneous WSS distributions, contours of swirling strength and streamline patterns for $Rem = 1160$	71
Figure 5.1. Comparison of swirl strength contours for Base.....	75
Figure 5.2. Comparison of swirl strength contours for Case 1.....	76
Figure 5.3. Comparison of swirl strength contours for Case 2.....	77
Figure 5.4. Comparison of time-averaged swirl strength contours, streamline patterns and the variation of WSS measures on the aneurysm wall, for the waveform patterns, Base, Case 1 and 2.....	78
Figure 5.5. Comparison of WSS distributions, swirl strength and shear rate contours of Newtonian and selected shear-thinning rheology models for the Case 1 and 2..	80
Figure 5.6. Comparison of time-averaged streamline patterns, swirl strength and shear rate contours of selected rheology models for the waveform patterns, Base, Case 1 and 2.....	82
Figure 5.7. Comparison of OSI and ECAP distribution on the aneurysm wall of selected rheology models the waveform patterns, Base, Case 1 and 2	83
Figure 5.8. Comparison of a. swirl strength contours and streamline patterns b. time-averaged swirl strength contours and streamline patterns of different rheology models for Base	85
Figure 6.1. Temporal evolution of instantaneous WSS, contours of swirl strength, λci , and streamline patterns for the Model 1.....	91
Figure 6.2. Contours of Q -criterion, $\lambda 2$ -criterion, swirl strength, λci , streamline pattern, and TAWSS, ECAP, OSI and RRT variations on the aneurysm wall for Model 1.....	93

Figure 6.3. Temporal evolution of instantaneous WSS, contours of swirl strength and streamline patterns obtained for Models 2 and 3	95
Figure 6.4. Comparison of swirl strength contours, streamline patterns and the variation of WSS measures on the aneurysm wall.....	99
Figure B.1. Temporal evolution of swirling strength for Model 1 and $Rem = 670$	133
Figure B.2. Temporal evolution of swirling strength for Model 2 and $Rem = 670$	134
Figure B.3. Temporal evolution of swirling strength for Model 3 and $Rem = 670$	135
Figure D.4. Temporal evolution of shear rate for Base case.....	143
Figure D.5. Temporal evolution of shear rate for Case 1	144
Figure D.6. Temporal evolution of shear rate for Case 2	145

LIST OF ABBREVIATIONS

ABBREVIATIONS

<i>AAA</i>	=	abdominal aortic aneurysm
<i>ILT</i>	=	intraluminal thrombus
<i>L_{ent}</i>	=	entrance length
<i>L_B</i>	=	bulge length
<i>L_{ex}</i>	=	exit length
<i>R_B</i>	=	bulge radius
<i>R</i>	=	aorta radius
τ_w	=	wall shear stress
<i>WSS</i>	=	wall shear stress
<i>TAWSS</i>	=	time-averaged wall shear stress
<i>OSI</i>	=	oscillatory shear index
<i>ECAP</i>	=	endothelial cell activation potential
<i>RRT</i>	=	relative residence time

LIST OF SYMBOLS

SYMBOLS

x	=	axial direction
r	=	radial direction
u_x	=	axial velocity component
u_r	=	radial velocity component
$\overline{U_x}$	=	time – averaged axial velocity
Q	=	Q-criterion
λ_2	=	λ_2 -criterion
λ_{ci}	=	λ_{ci} -criterion, swirling strength
\overline{Q}	=	time – averaged Q-criterion
$\overline{\lambda_2}$	=	time – averaged λ_2 -criterion
$\overline{\lambda_{ci}}$	=	time – averaged λ_{ci} -criterion
τ_e	=	elastic stress tensor
τ_s	=	viscous stress tensor
λ_1	=	relaxation time constant for elastic stress tensor
μ_e	=	elastic dynamic viscosity
μ_s	=	viscous dynamic viscosity
$\dot{\gamma}$	=	shear rate
$\overline{\dot{\gamma}}$	=	time – averaged shear rate

μ_{∞}	=	viscosity at infinite shear rate
μ_0	=	viscosity at zero shear rate
λ	=	relaxation time constant for shear-thinning rheology models
K	=	flow consistency index
n	=	power law index
ω	=	frequency of cardiac cycle
ν	=	kinematic viscosity
T	=	period of cardiac cycle
Re_m	=	mean Reynolds number
U_m	=	mean velocity

CHAPTER 1

INTRODUCTION

Abdominal aortic aneurysm (AAA) is the dilatation of the abdominal aorta beyond 50% of the normal vessel diameter, due to degeneration of the arterial wall (McGloughlin Timothy and Doyle Barry, 2010). It is reported that 4–8% of men and 0.5–1% of women above 50 years of age bear an AAA and it accounts for approximately 15,000 deaths per year in the United States alone (Sakalihan et al., 2005; Kontopodis et al., 2014). In Figure 1.1, an illustration of AAA is presented. AAA may result in rupture of the vessel wall, which is a fatal surgical emergency because of reduced blood flow to vital organs and hemothorax (i.e. swelling caused by blood collecting in a body cavity). Currently, there are two frequently utilized techniques to treat AAAs, which are open surgical repair and endovascular aneurysm repair via stenting (EVAR). Although open surgical repair has been used for many decades as a treatment technique, it is a procedure with 5% elective repair post-operative mortality and 47% emergency operations post-operative mortality (Hallin et al., 2001). Alternatively, EVAR is a minimally-invasive technique, and it is becoming more common procedure for AAA, with the potential advantages of reductions in mortality, morbidity, blood loss, hospital stay, and discomfort. However, even this approach is subject to post-procedural complications, mostly caused by the development of endoleaks or to the mechanical failure of the device, which can occur in 15% to 52% of cases (Vorp David and Geest Jonathan, 2005).

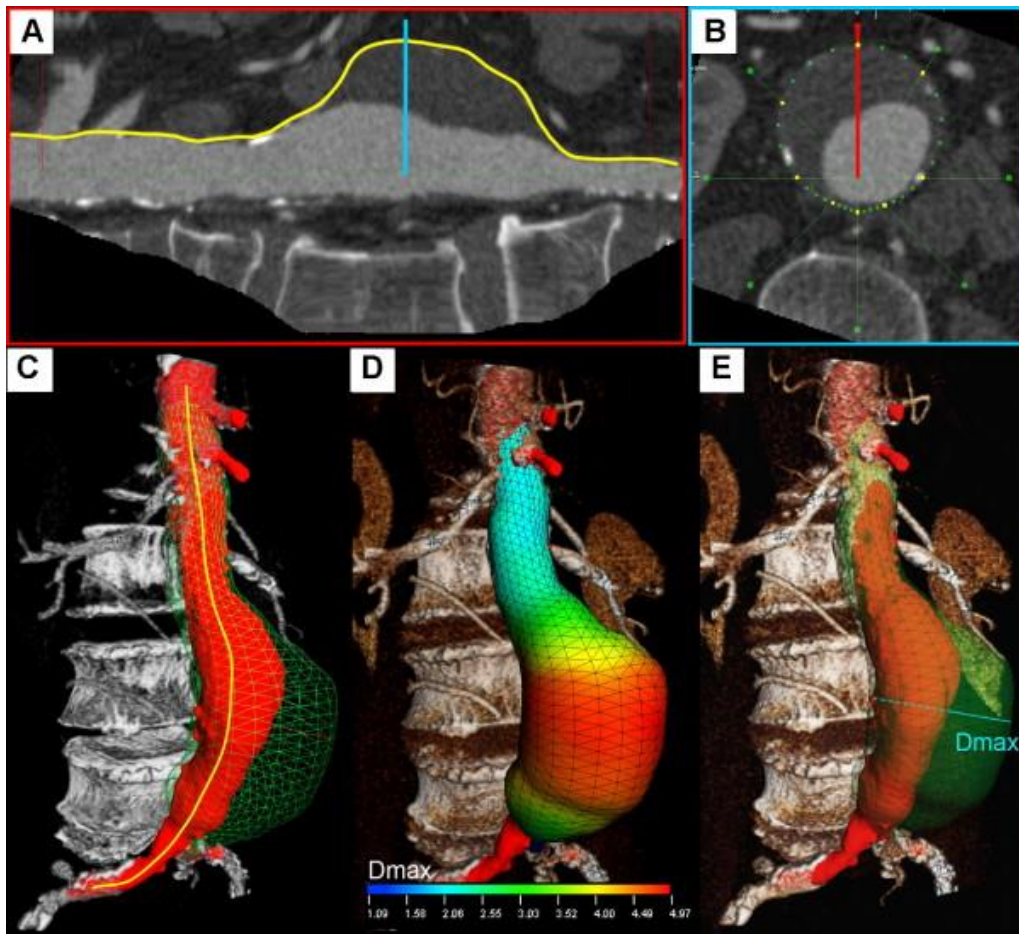


Figure 1.1. Magnetic resonance imaging of an abdominal aortic aneurysm (AAA)

Given these limitations and risks of current repair techniques, it is important to determine when, during the course of an aneurysm, the risk of rupture justifies repair. Therefore, predicting the risk of rupture for an aneurysm is critical in the decision of treatment. It is reported that only 25% of AAAs rupture in a patient's lifetime (Darling et al., 1977), and it is also known that smaller aneurysms can also rupture, for example, in an autopsy study, Darling et al. (1977) show that 13% of the aneurysms smaller than 5 cm diameter are ruptured. Indeed, there are reports also showing that aneurysms having diameter larger than 9 cm can remain stable (Vorp, 2007; Moll et al., 2011). Thus, along with AAA size, other factors should also be considered for rupture risk assessment.

The precise mechanisms leading to AAA rupture remains unclear. From a purely mechanical point of view, rupture of an AAA occurs when the mechanical stresses (i.e. internal forces per unit area) acting on the aneurysm exceeds the ability of the wall tissue to withstand these stresses (i.e. the wall's failure strength). Together with variations of the mechanical morphology of wall, effect of dynamics of blood flow, which is known as blood hemodynamics, is considered as a contributing factor for growth and rupture mechanism. Wall shear stress (i.e. WSS, the frictional force exerted by blood flow on the luminal surface) is also thought to play an important role (Peattie et al., 1996). While the blood flow in normal aorta (diameter within 2-2.5 cm) is mainly antegrade with high WSS, during AAA, circulatory flows emerge within the vessel. Hence, flow becomes disturbed with oscillatory characteristics leading to low WSS (Tanweer et al., 2014). The disturbance of flow in AAA is believed to contribute to the progression of the disease by activating the inflammatory markers of the endothelial cells lining the vessel wall which might lead to degeneration and weakening of the vessel wall (Ryan et al., 2016).

To quantify the disturbance in hemodynamics inside aneurysm sac, wall shear stress (WSS) parameters such as time-averaged wall shear stress (TAWSS), oscillatory shear index (OSI), endothelial cell activation potential (ECAP) and relative residence time (RRT) are used. In literature, a vast number of studies have postulated a correlation between the WSS parameters and intraluminal thrombus (ILT) formation (Arzani et al., 2014; Boyd et al., 2016; Les et al., 2010; Kelsey et al., 2016). In terms of aneurysm growth characteristics, the role of ILT is a controversial issue. From a biomechanical point of view, it is interpreted as beneficial to prevent rupture due to its pressure-wave dampening feature (Di Martino and Vorp, 2003). However, in a clinical study it is reported that ILT is observed near the site of rupture for 80% of the autopsies (Simão da Silva et al., 2000), and it can also be seen as a source of proteolytic activity, local wall thinning, wall weakening, and hypoxia (Swedenborg and Eriksson, 2006). Different theories exist in literature regarding the relation between ILT formation and aneurysm hemodynamics. The most well-known approach is that the low and oscillatory WSS may stimulate the endothelial cells and

promote the inflammatory process, causing wall-cell adhesion due to platelet accumulation, forming ILT (Boyd et al., 2016; Kelsey et al., 2017). Most researchers agree that the locations with low WSS, high OSI and high ECAP are prone to thrombus formation and have a higher risk of rupture (Les et al., 2010; Kelsey et al., 2016). On the other hand, in some studies reporting contradicting results (Arzani et al., 2014; Singh et al., 2018; Biasetti et al., 2011; Biasetti et al., 2012), it is stated that low WSS and high OSI regions do not necessarily coincide with thrombus deposition and atherosclerosis formation. Especially, Arzani et al. (2014) specified that low OSI with moderate TAWSS values (between 0.2 - 0.3 Pa) are prone to develop ILT, while very low TAWSS (< 0.1 Pa) with high OSI (> 0.4) prevent thrombus deposition. In literature, several studies also reported a correlation between recirculation zones and ILT formation. Arzani et al. (2014) reported that near-wall recirculation zones contribute to low OSI and enhanced thrombus deposition. Kelsey et al. (2017) stated that low-velocity recirculation zones are located near the regions where ILT has formed. They concluded that high residence time, flow stagnation, vortex structure, and high ECAP all correlate spatially with the regions where ILT develops. Biasetti et al. (2011; 2012) correlated vortical structures with high WSS and attributed bursting of the vortical structures to thrombus deposition at low WSS areas. Therefore, together with WSS parameters, quantifying the vortical structures may lead to better understanding of their effect on ILT formation and rupture mechanism of aneurysms.

Over several decades, in order to investigate the hemodynamics inside the abdominal aortic aneurysms, a vast amount of numerical studies is performed (Finol and Amon; Kelsey et al., 2016; Arzani et al., 2014), and accuracy depending on the boundary conditions and modeling parameters used in computational models (Salman et al., 2019). Computational models enable researchers to approximate behavior of blood hemodynamics under realistic conditions. The models are generated by defining the conditions on the boundaries and numerically solving governing equations in the fluid domain. Together with adjusting the problem geometry, mesh, turbulence models; setting up boundary conditions (BC) and fluid properties are also very

important steps which affect the reliability and accuracy of the hemodynamic assessment. Inlet and outlet boundary conditions are defined considering the physiological pulsatile flow. Time-dependent inlet flow rate obtained at the infrarenal section of aorta can be applied considering different velocity profiles. The most accurate application is utilizing PC-MRI measured patient-specific velocity profiles as an inlet velocity BC, obtained from the human aorta (Chandra et al., 2013; Youssefi et al., 2018). However, accessing to complete high quality patient-specific geometry and inlet profile data is not always possible due to lack of imaging facilities (Armour et al., 2021). Furthermore, directly measuring in vivo inflow conditions is still challenging because of the cardiac motion and resolution (Lodi Rizzini et al., 2020). Indeed, in several studies it is reported that there is no significant difference between profiles obtained from PC-MRI and artificial ones (Morris et al., 2006; Wei et al., 2019). Therefore, many studies in literature frequently use the idealized profiles such as *Plug* (Chen et al., 2020; Drewe et al., 2017), *Parabolic* (Bit et al., 2020; Boyd et al., 2016; Li and Kleinstreuer, 2005; Bilgi and Atalik, 2020) and *Womersley* (Arzani et al., 2014; San and Staples, 2012).

Plug profile is the uniform velocity at the inlet, while *Parabolic* profile obtained from Poiseuille's equation and therefore they cannot present all the characteristics generated due to transitional effects. Although *Womersley* profile is necessary to present transient effects especially for large α values, applicability and implementation of Womersley equation as an inlet boundary condition can be difficult because of the Bessel functions and imaginary numbers that it contains (Campbell et al., 2012; Impiombato et al., 2021). Therefore, in literature, most of the studies utilize *Plug* or *Parabolic* profiles with long entrance lengths to obtain fully developed condition, rather than the *Womersley* profile, which increases the computation time (Stamatopoulos et al., 2010). Indeed, necessary entrance length to obtain fully developed conditions is also a controversial issue. In general, researchers concerned about the inlet velocity boundary conditions and to be on the safe side, they tend to be extend the size of entrance region to ensure fully developed conditions (Madhavan and Kemmerling, 2018). In literature, recommended entrance

length values to reach the fully developed state are significantly large (Durst et al., 2005; Salman et al., 2019). On the other hand, Hoi et al. (2010) reported that an entrance length at least three diameters of the artery is sufficient to avoid negligible errors in hemodynamics of the carotid arteries (Hoi et al., 2010). However, from a different point of view, Madhavan and Kemmerling (2018) stated that in the actual human arterial system, obtaining the fully developed hemodynamic conditions is not realistic due to the orientation of the vasculature, such as the thoracic aorta is located immediately distal to the heart. Campbell et al. (2012) hypothesized that *Womersley* and *Parabolic* inlet velocity BCs give nearly the same result in carotid bifurcation, where $\alpha = 4.1$ and average radius is 3 mm. However, they highlighted that the results are not applicable for large arteries like aorta, in which α is larger than 10, and they require further studies. In 2019, Wei et al. (2019) stated that no significant difference between realistic, *Womersley* and *Parabolic* inlet profiles while *Plug* is notably different than the others for Fontan hemodynamics.

In addition to boundary conditions, replicating the patient-specific rheological behavior of the human blood is also a determinant in the accuracy of the hemodynamic predictions. Blood is a concentrated suspension of various cellular elements, which are red blood cells (RBCs), white blood cells (WBCs) and thrombocytes, inside the plasma which is composed of 93% water and 3% particles, which are organic molecules, electrolytes, proteins and wastes gathered from organism (Bessonov et al., 2016). The plasma behavior is very similar to a Newtonian fluid. However, at very low shear rates, non-Newtonian behavior of blood becomes more apparent. At shear rates less than 100 s^{-1} , red blood cells (RBCs) aggregate and form rouleaux, which is rod shaped stacks of individual cells (Bessonov et al., 2016). Aggregation and disaggregation of rouleaux lead the blood to exhibit a shear-thinning and elastic behavior (Bessonov et al., 2016; Bilgi and Atalık, 2020; Bodnár et al., 2011). Abdominal aortic aneurysm (AAA) is the dilatation of the abdominal aorta beyond 50% of the normal vessel diameter, due to degeneration of the arterial wall (McGloughlin Timothy and Doyle Barry, 2010). Abdominal aorta is a large artery where the flow rate is also larger compared to other

arteries, which leads to a high shear rate distribution. However, inside the aneurysm sac, there are stagnant and low velocity recirculation regions due to the separation of bulk flow at diastolic phase (Salman et al., 2019), causing low shear rates at that zones.

In literature, a vast amount of studies agrees that non-Newtonian effects diminish with increasing flow rate (Shibeshi and Collins, 2005; Soulis et al., 2008), because they generate high shear rate distribution. Skiadopoulos et al. (2008) have reported that Newtonian approach is satisfactory in high shear and flow rates to estimate AAA hemodynamics. Also, Fisher et al. (2009) stated that non-Newtonian properties of blood are more influential during diastole due to lower flow rate. Indeed, there are various flow waveform patterns available in literature for infrarenal section of the aorta, which is just upstream part of the abdominal aneurysm. The flow waveform at that section shows different characteristics from patient to patient. Measured infrarenal flow waveforms of two different patients during resting condition is presented in Figure 1.2 (Les et al., 2010). It is obvious that, for resting condition, especially the peak systolic flow rate value is significantly different for different patients. Also, diastolic flow rate, which is the flow rate value at the beginning of the cardiac cycle is equal to zero for most of the patients during resting. However, for different cardiac conditions, diastolic flow rate might be higher than zero. For example, according to Les et al. (2010), diastolic flow rate might reach to 100 ml/sec during exercise condition. Such variations in infrarenal flow waveform pattern might lead different shear rate distributions through abdominal aortic aneurysms during systolic and diastolic phases, and might affect the rheology model selection. From that point of view, it might be useful to observe the behavior of different rheology models utilized in blood modeling for different inlet flow conditions. The most common non-Newtonian models that have been considered in the literature for the shear dependent viscosity of whole human blood are Carreau, Carreau-Yasuda, Casson, Power, Quemada, Cross, Modified and Simplified Cross models (Cho and Kensey, 1991).

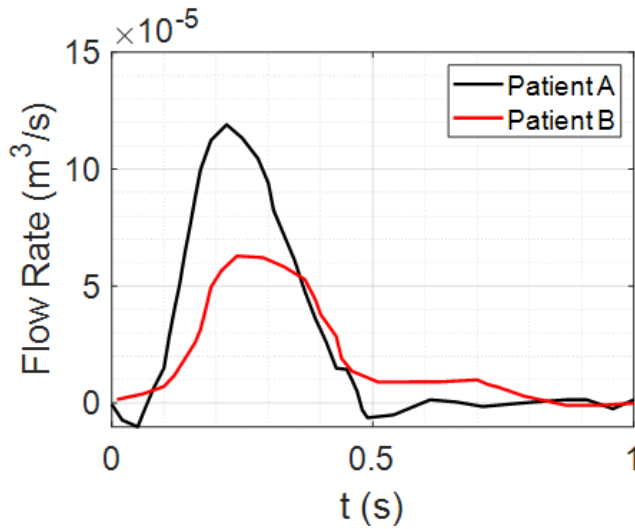


Figure 1.2. A comparison of measured physiological infrarenal flow rate during rest for two different patients (Les et al., 2010)

Although disturbed flow is generally quantified by WSS parameters such as TAWSS, OSI, ECAP and RRT, in a meta literature analysis study, Saqr et al. (2020) have reported that WSS parameters solely are not enough to bridge hemodynamics and aneurysm pathology. In addition to such a scalar-tensor field comparison, quantifying the vector fields, such as vortex structures, may lead to better understanding of their effect on ILT formation and rupture mechanism of aneurysms. In early studies, vorticity magnitude is utilized to define vortices. However, it is not able to discriminate between the shear motions and vortex cores (Chen et al., 2015). Therefore, in later studies, different criteria have been postulated to analyze vortex dominated behavior isolated from the shear motion. Vortex structures can be quantified by Q -criterion, Δ -criterion, λ_2 -criterion, and swirling strength (λ_{ci}) criterion (Chen et al., 2015; Epps, 2017). Moreover, due to limitations arising from low spatial resolution and optical constraints in proximity to the wall, obtaining WSS parameters using experimental methods is a challenging issue (Bauer et al., 2020). However, acquiring vortex structures is a very common approach in experimental studies, and it does not require exact wall data (Deplano et al., 2016). Thus, a correlation between WSS parameters and vortex structure might be a useful tool

especially for determining ILT formation region using experimental methods, such as Particle Image Velocimetry (PIV).

1.1 Motivation of the Study

In simulation of exact patient-specific hemodynamics to determining ILT formation and rupture region inside AAAs, selection of boundary conditions and fluid properties are very effective. Although *Womersley* profile is necessary to present transient effects especially for large α values, applicability and implementation of Womersley equation as an inlet BC might be difficult because of the Bessel functions and imaginary numbers that it contains. On the other hand, studies applying *Parabolic* and *Plug* inlet velocity BCs utilize significantly long entrance lengths to reach fully developed Womersley condition, which might increase the computational cost. Therefore, it might be significant to observe the differences in hemodynamic parameters arising from utilization of common inlet BCs, which are *Womersley*, *Parabolic* and *Plug*, to criticize the necessity of *Womersley* profile and significantly long entrance lengths. To the author's best knowledge, there is a deficiency in literature to compare the effect of ideal velocity profiles on abdominal aortic aneurysm hemodynamics, where Womersley number is larger than 10, with different entrance lengths.

Modeling the patient-specific rheological behavior of the human blood is also crucial in obtaining the exact ILT formation region because properties of fluid domain affects hemodynamic predictions significantly. Although blood behaves as Newtonian fluid for higher shear rates, its viscous shear-thinning and elastic nature arises for shear rates lower than 100 s^{-1} . Inside the aneurysm sac, low shear rate regions exist due to flow stagnation, especially at diastolic phase. Moreover, infrarenal flow waveform pattern, especially peak and diastolic flow rate, differs from patient to patient. Such variations in infrarenal flow rate might lead different shear rate distributions through abdominal aorta during systolic and diastolic phases, and might affect the rheology model predictions. Moreover, the effect of various

shear thinning models on hemodynamic parameters is studied previously for the carotid (Razavi et al., 2011; Morbiducci et al., 2011; Lee and Steinman, 2007; Medienta et al., 2020), thoracic (Karimi et al., 2014; Faraji et al., 2022) and cerebral (Fisher and Rossmann, 2009) arteries, but a comprehensive comparison of them together with viscoelastic model in AAA is not available in literature.

Quantifying disturbed aneurysm hemodynamics by only a scalar-tensor field WSS parameters might not be enough to understand the reasons of ILT formation. Moreover, determining the WSS parameters experimentally is a challenge due to limitations arising from low spatial resolution and optical constraints in proximity to the wall. Therefore, to better understand the effect of blood flow on ILT formation and to serve a facility for experimental studies in order to determine ILT region, a correlation between WSS parameters and vortex identification methods might be determined. To the authors' best knowledge, no correlations of these parameters exist in the literature.

1.2 Aim of the Study

Boundary conditions and fluid properties significantly affect the hemodynamic predictions inside AAAs, which might mislead the prediction of ILT formation region. The aim of this study is understanding the effect of inlet boundary conditions and rheology model selection on predicting the WSS parameters and vortex structures, which are frequently used hemodynamic parameters to predict ILT formation, and determining a correlation between those parameters. First of all, to characterize the differences generated by *Plug*, *Parabolic* and *Womersley* inlet velocity profiles at different entrance lengths, $L_{ent} = D, 3D, 11D$ and $50D$, axial velocity profiles, OSI and ECAP distributions and swirling strength contours are plotted and compared. Secondly, to observe the effect of rheology model selection on predicting hemodynamic parameters, eight viscous shear-thinning models at three different infrarenal flow waveforms, which are Base, Case 1 and 2, are tested and the results are compared with the Newtonian model. Moreover, the effect of elasticity

of blood is also studied using Oldroyd-B model and compared with Newtonian and viscous shear-thinning models. WSS parameters together with instantaneous and time-averaged shear rate and swirling strength contours are plotted and compared. Finally, to determine the correlation between WSS parameters and vortex identification methods, numerical experiments are conducted for three different aneurysm models with bulge radius to aorta radius ratio, $R_B/R = 2.44, 3.66$ and 4.88 . Vortex structures are quantified by Q -criterion, Δ -criterion, λ_2 -criterion, and swirling strength (λ_{ci} -criterion), and instantaneous WSS distributions and streamlines are compared with swirling strength contours. Moreover distributions of WSS parameters are compared with contours of time averaged swirling strength, $\overline{\lambda_{ci}}$, to identify whether correlations can be established between wall shear stress parameters and vortex identification methods.

1.3 Structure of the Thesis

This thesis is composed of seven main chapters. Chapter 1 provides introductory information abdominal aortic aneurysms and summarizes the aim and the motivation of the current study.

Chapter 2 presents the detailed literature review including the general hemodynamics for AAAs, and their modeling techniques that are frequently used in literature.

Chapter 3 explains the mathematical equations, numerical methods and their validations that are utilized in this study. Also, matrices of numeric experiments are given in that chapter.

Chapter 4 shows a characterization of the behavior of idealized inlet velocity profiles at different entrance lengths and Reynolds numbers, while Chapter 5 presents comparison of shear-thinning and viscoelastic rheology models with Newtonian model for three different waveform patterns. Also, Chapter 6 examines the possible correlations between wall shear stress parameters and vortex identification methods.

Finally, Chapter 7 provides the conclusions throughout the study together with the possible future work recommendations.

CHAPTER 2

LITERATURE REVIEW

Computational modeling has been used frequently in recent years to investigate rupture mechanics for AAA tissue. Comparison of ruptured and electively repaired AAA cases via FEA, revealed elevated wall stress levels for ruptured tissue (Fillinger et al., 2002). Several observations on excised tissue suggest that AAA formation is accompanied by an increase in wall stress as well as a corresponding decrease in wall strength (Vorp et al., 1996; Raghavan et al., 2000) and rupture point on AAA is usually coincides with peak wall stress locations (Fillinger et al., 2002). In very few studies where previous medical images for ruptured AAA tissue were available, patient-specific FEA could successfully identify known exact future rupture locations as high wall stress regions (Doyle et al., 2014). The FEA results prove the potential significant contribution of computational analysis for rupture risk assessment for AAA.

Additionally, disturbed hemodynamics through AAA should be characterized for locations of low WSS and oscillatory flow as potential rupture locations (Les et al., 2010). Because of geometrical complexities, it is clinically challenging to map hemodynamics for AAA. Computational fluid dynamics (CFD) simulations can potentially be used for biomechanical assessment to determine critical hemodynamic parameters affecting the growth and progression of AAA (Khanafar et al., 2007). Previous studies show that oscillatory flows (i.e. flow to oscillate forward and backward) in AAA can cause damage to endothelial cells (ECs), resulting in inflammation and thrombus and/or calcification formations in the wall (Tanweer et al., 2014). Therefore, spatial determination of these disturbed flow regions will help to identify potential rupture locations at very early stages during the course of the condition.

Despite the potential benefits, CFD simulations can only investigate the disturbed AAA hemodynamics in fluid domain without considering wall behavior and FEA models enable only wall stress analysis in solid domain without blood flow behavior. However, there are strong interactions between blood flow and AAA wall, which significantly affects the rupture mechanism. For increased accuracy, the mutual effects between the blood flow and vessel wall should be considered. Most recent computational models are based on this approach which is known as fluid-structure interaction (FSI) modeling (Drewe et al., 2017; Canchi et al., 2018). In this technique, hemodynamic forces deform the tissue and tissue wall displacements affect the behavior of blood flow. FSI requires simultaneous and coupled solution of governing fluid flow and tissue displacement equations. Even though, FSI modeling is more complex, it is shown that FSI models can predict native AAA tissue behavior better with increased wall stress results up to 20% compared to FEA models without fluid flow (Scotti et al., 2008).

As computational methods have widely been used in investigation of hemodynamics and mechanical behavior of arterial tissue, the experimental techniques are also utilized in characterization of flow dynamics through abdominal aortic aneurysms. Both approaches are crucial and complement each other with offering in depth analysis where the level of its intensity and accuracy depend on the assumptions in computational models and simplifications in experimental methods. In line with the aforementioned computational studies, many experimental investigations of the hemodynamics through AAAs have been conducted in literature, and various qualitative and quantitative flow measurement techniques have been utilized for that purpose. A typical experimental set up for the analysis of hemodynamics contains physiological flow circulatory system including pump, piping, and pressure compliance, test section that contains artery model (phantoms), blood mimicking fluid, and flow measurement systems (like particle image velocimetry) to track the movement of fluid particles to calculate the velocities first, and then WSS levels on the phantoms. Previously, this approach has been adapted by several researchers to investigate AAA rupture mechanism (Tanweer et al., 2014; Wang et al., 2016).

2.1 Computational investigation of hemodynamics of AAAs

Computational models enable researchers to approximate biomechanical behavior of tissue stress and blood flow hemodynamics under realistic conditions. The models are generated by defining the conditions on the boundaries and numerically solving governing equations in fluid and solid domains. Generation of the problem geometry, setting up solid and fluid models, coupling the solutions through FSI procedure are important steps which contribute to enhance the reliability and accuracy of the biomechanical assessment as will be mentioned in the forthcoming sections.

2.1.1 Geometry of the problem

AAA has unique, patient-specific and complex geometry with a wall thickness around 1.5 mm (Raghavan et al., 2004) and mostly does not represent an axisymmetric form. Healthy abdominal aortic diameter is around 2 cm and in case of dilatation, AAA diameter can expand up to 9 cm. Proximal AAA neck angle, distal iliac bifurcation angle, heterogenous wall thickness are patient-specific geometric parameters. Left and right renal arteries, left and right iliac arteries and superior mesenteric artery are the main branching arteries in abdominal aorta. In Figure 2.1, different patient-specific AAA geometries, branching arteries and disturbed flow in AAA sac is presented. As seen in the figure, geometry differs significantly from patient to patient.

Main geometric parameters for a patient-specific AAA are presented in Figure 2.2. The AAA asymmetry is defined using the relation defined by Vorp et al. (1998). β is the parameter of asymmetry defined according to the central axis of undilated diameter, as shown in Figure 2.2. In Eq. (1), r and R are the radii measured from center of the undilated portion to the posterior and anterior walls, respectively. In addition to the maximum aneurysm diameter, tortuosity, curvature, proximal neck angle, iliac bifurcation angle and complex shape of the aneurysm itself are influencing factors on the wall stress (Stringfellow et al., 1987; Vorp et al., 1998;

Hua and Mower, 2001). Up to 80% of AAA rupture are observed on the posterior wall (Darling et al., 1977), demonstrating the importance of asymmetry and curved AAA geometry in rupture. Loss of curvature on the posterior wall and AAA asymmetry are suggested as dominant wall stress increasing factors (Scotti et al., 2008). Different levels of asymmetry were modeled using idealized geometries with the same patient-specific inlet velocity boundary conditions asymmetry (Scotti et al., 2008). For the most asymmetric model with $\beta=0.2$ (see Eq. (2.1) for definition of β), AAA diameter expanded by 15.2% at the peak systolic pressure. When an axisymmetric ($\beta=1$) AAA model is considered, the diameter expansion is observed as 12.8%, implying that increasing asymmetry resulted in higher AAA deformation and therefore higher peak wall stress on the wall. As AAA becomes more asymmetric, location of peak wall stress shifted from anterior to the posterior wall. Drewe et al. (2017) performed FSI simulations to investigate the effects of proximal neck and lateral iliac bifurcation angles considering idealized AAA models. Recent morphological comparisons showed that AAAs with large iliac bifurcation angle have a lower rupture risk (Drewe et al., 2017). Proximal neck angle has less impact on the AAA hemodynamics compared to the iliac bifurcation angle. When the iliac bifurcation angle increased from 30° to 150°, peak WSS increased more than two-fold (from 2.91 to 6.19 Pa), peak von Mises wall stress increased about 30% (from 0.186 to 0.243 MPa) and ECAP decreased by 57% (from 11.41 to 7.25). These results indicated that larger iliac bifurcation angle was more protective of ILT formation and AAA expansion due to provoking high WSS and low ECAP conditions (Drewe et al., 2017). However, excessive load on the iliac arteries with increased bifurcation angle may increase the risk of an iliac artery aneurysm initiation (Xenos et al., 2010).

$$\beta = \frac{r}{R} \quad (2.1)$$

The maximum AAA diameter is the first indicator for the treatment. For the current practice, when maximum AAA diameter exceeds 5-6 cm or diameter growth rate is higher than 1 cm per year, open surgery or endovascular treatment methods are

performed considering the life expectancy of the patient (Scott et al., 2002; Longo and Upchurch, 2005; Chandra et al., 2013). Canchi et al. (2018) performed a comparative FSI study, considering two patient-specific AAAs with maximum aneurysmal diameters of 3.5 and 7 cm. Maximum principle stresses were determined as 0.30 and 0.22 MPa for 3.5 and 7 cm AAA diameters, respectively, implying that size of AAA is not the sole determinant for the rupture risk, and biomechanical assessment is needed for further identification of the case. Similarly, (Fillinger et al., 2002; Fillinger et al., 2003) reported that maximum wall stress was 12% more accurate for predicting rupture compared to using maximum AAA diameter alone as an indicator.

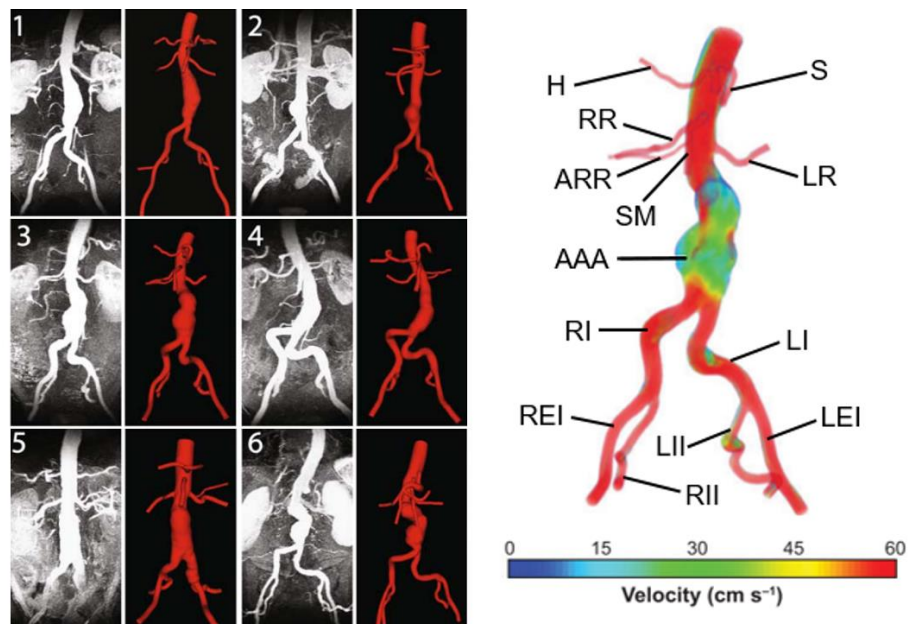


Figure 2.1. Six different patient-specific medical images and corresponding reconstructed AAA geometries (Les et al., 2010).

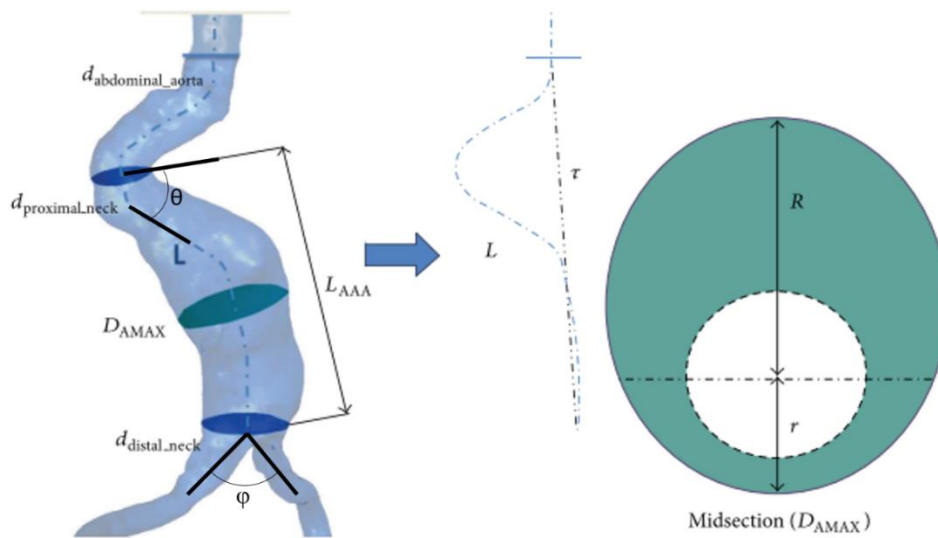


Figure 2.2. Main geometric parameters for a patient-specific AAA geometry. (Soudah et al., 2013).

2.1.2 Generation of Patient Specific Model Geometry

Magnetic resonance imaging (MRI), three-dimensional ultrasound, computerized tomography (CT) are the most common medical imaging techniques used to extract the realistic geometry of AAAs. Here, 2D slices are obtained within one breath-hold period to prevent artefacts due to the motion of the patient (Wolters et al., 2005). At present, primary imaging method is CT. However due to its high cost, significant radiation dose, injection of ionated contrast medium associated with nephrotoxicity and relatively less availability, alternative methods such as three-dimensional (3D) ultrasound can be used to widespread the biomechanical assessments. Owen et al. (2016) performed CFD simulations using either CT or 3D ultrasound generated AAA geometries from same patients and the comparison of two extraction methods exhibited similar qualitative results in terms of WSS, flow velocity and vorticity. WSS difference between CT and 3D ultrasound-derived models was within 10% for locations away from the AAA inlet and outlet. However, around the iliac bifurcation region at the outlet, 3D ultrasound-derived model led to approximately 1.5 times increased WSS. The discrepancy is most likely due to the challenges to obtain

upstream aorta geometry using 3D ultrasound imaging, since ultrasound cannot pass well through the rib cage due to high acoustic impedance of bones. Also it may become difficult to image iliac arteries when the distance between skin-to-artery increases (Owen et al., 2016), limiting utilization of 3D ultrasound modality in AAA imaging.

After obtaining patient-specific medical images in DICOM (Digital Imaging and Communications in Medicine) format, 3D AAA models can be reconstructed using segmentation softwares such as MIMICS (Materialise, Leuven, Belgium), VESSEG (Carnegie Mellon University, Pittsburgh, PA) and ImFusion Suite (ImFusion GmbH, Munich, Germany). Here, lumen, ILT and AAA wall are segmented separately to differentiate these zones. After completing the segmentation process, further geometrical improvement and smoothing are typically necessary to successively discretize the problem domain into finite elements. Segmented 3D model might include protrusions and tight internal corners, which requires application of smoothing algorithms, to prepare a suitable geometry for CFD and FEA simulations. Autodesk MeshMixer, AngioLab and MeshLab softwares can be used for further smoothing and mesh optimization processes. For smoothing process, different algorithms can be applied such as Laplacian (Field, 1988), HC Laplacian (Vollmer et al., 2001) and Taubin's low pass filter (Taubin, 1995). For the same patient specific AAA geometry, rates of shrinkage (i.e. percentage of remaining volume after smoothing) for the smoothed geometries are reported as 98.27%, 99.11% and 99.85% for Laplacian algorithm, HC Laplacian algorithm and Taubin's low pass filter, respectively (Owen et al., 2016). HC Laplacian algorithm and Taubin's low pass filter are suitable due to their superior quality of smoothed AAA geometry. In Figure 2.3, the reconstruction procedure of a patient-specific AAA model is given.

It should be noted that in some cases, the reconstructed AAA geometry is obtained in an already pressurized form during the systolic phase. To better estimate wall mechanics, AAA geometry may be constructed utilizing clinical images during the diastolic phase with minimum intraluminal pressure. Alternatively, an already pressurized state of clinical image-based AAA wall geometry can be modified

according to a zero-pressure configuration, meaning a virtual contraction is applied in AAA model until reaching zero-stress on the wall. Otherwise, applied physiologic boundary conditions would result in underestimated wall stress results (Chandra et al., 2013).

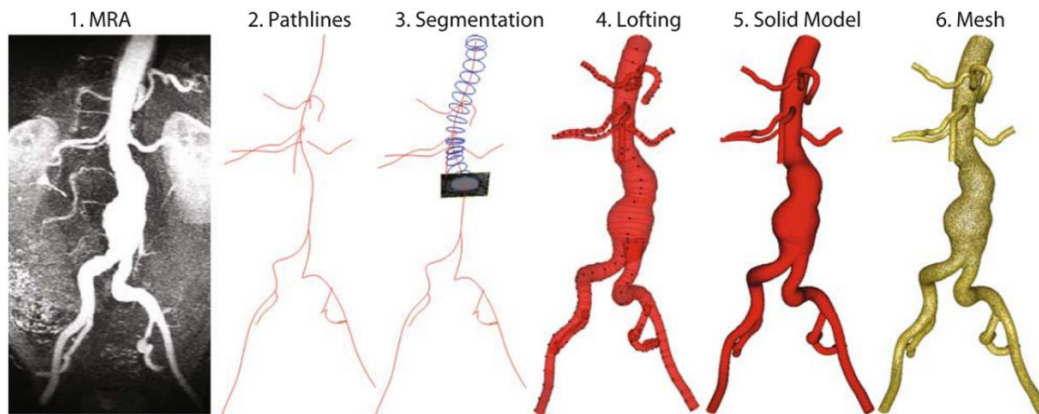


Figure 2.3. Reconstruction procedure for a patient-specific AAA model (Les et al., 2010).

2.1.3 Boundary Conditions

Inlet and outlet boundary conditions (BC) are defined considering the physiological pulsatile flow. Commonly, time-varying flow velocity given in Figure 2.4(a) is defined at the inlet of fluid domain and time-varying intraluminal pressure given in Figure 2.4(b) is prescribed at the outlet of fluid domain (Scotti et al., 2008). The incidences of peak flow velocity and peak intraluminal pressure may not be at the same time in the cardiac cycle. The time lag between these two peaks results in a phase difference contributing to the generation of recirculating vortex formation. No slip BC is applied on the wall of fluid domain considering the viscous blood flow.

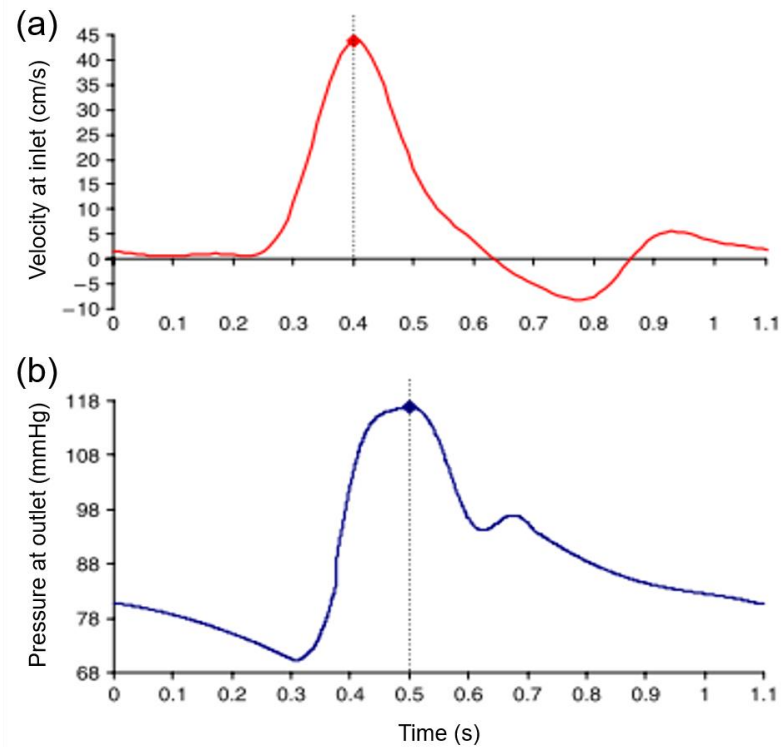


Figure 2.4. Waveforms of applied boundary conditions (a) Sample inlet flow velocity profile. (b) Sample outlet pressure profile (Scotti et al., 2008).

The time-dependent inlet flow rate given in Figure 2.4(a) can be applied considering different velocity profiles. For the velocity inlet conditions, applying the flow rates obtained from healthy cases can mislead the results. This is due to the specific conditions in patients with hypertension or atherosclerosis leading a serious disturbance in whole body circulation and hemodynamics (Lakatta, 2002). In similar way, the outflow BC can show a difference depending on the impedance of the distal parts in the arterial tree (Wolters et al., 2005). Therefore, patient-specific inlet and outlet BC significantly affect AAA hemodynamics and associated wall stresses. After determining patient-specific inlet BC, distribution of mass flow rate to the branches of mesenteric, renal and iliac arteries should also be considered, since they are significantly affecting the mass flow rate at the outlet of AAA model. A one-dimensional arterial tree model can be used to determine appropriate inflow and outflow conditions to better reflect the reality for biological relevance (Formaggia et

al., 2003; Wolters et al., 2005). Les et al. (2010) modeled the effect of branch arteries at the downstream vasculature using three-element Windkessel model considering the capacitance, proximal resistance and distal resistance at the downstream. Using PC-MRI scanning, mean flow rates at supraceliac and infrarenal locations are measured as 3.51 L/min and 1.31 L/min, respectively. The difference of 2.2 L/min is distributed to the arterial branches between supraceliac (1 cm above celiac artery) and infrarenal (1 cm below the most distal renal artery) levels using three-element Windkessel model (Les et al., 2010).

The most accurate application is utilizing PC-MRI measured patient-specific velocity profiles as an inlet velocity BC, obtained from the human aorta (Chandra et al., 2013; Youssefi et al., 2018). Indeed, in several studies it is reported that there is no significant difference between profiles obtained from PC-MRI and artificial ones (Morris et al., 2006; Wei et al., 2019). Therefore, many studies in literature frequently use the idealized profiles such as *Plug* (Drewe et al., 2017; Chen et al., 2020), *Parabolic* (Bit et al., 2020; Arzani and Shadden, 2015; Li and Kleinstreuer, 2005; Bilgi and Atalik, 2020) and *Womersley* (Arzani et al., 2014; San and Staples, 2012). Although Womersley profile is required to present transient effects especially for large Womersley number (α) cases, applicability and implementation of Womersley equation as an inlet boundary condition can be nontrivial due to the nature of the Bessel functions involved in the equation (San and Staples, 2012; Womersley, 1955; Campbell et al., 2012). Therefore, in literature, most of the studies utilize *Plug* or *Parabolic* profile with long entrance lengths to obtain fully developed condition, rather than using the *Womersley* profile directly (Madhavan and Kemmerling, 2018).

Plug profile is the uniform velocity at the inlet, while *Parabolic* profile obtained from Poiseuille's equation and therefore they cannot present all the characteristics generated due to transitional effects. At 1955, Womersley derived the exact solution of laminar, incompressible, Newtonian fluid flow through a cylindrical and rigid blood vessel, in which a pressure gradient, which is periodic function of time, drives the flow (Womersley, 1955). The well-known non-dimensional parameter used in

simulating transient and pulsatile blood flow problems is the Womersley number, $\alpha = R\sqrt{\omega/\nu}$, where ω is the frequency of pulsation and ν is the kinematic viscosity. This non-dimensional number relates the transient inertial forces due to pulsatility to viscous forces. Womersley number has a strong effect on velocity profile throughout the arteries. For flows with small Womersley number, $\alpha < 1$, velocity profile is very similar to parabolic shape, while for $\alpha > 1$, the velocity profiles are no longer parabolic. For large Womersley number flows, especially for $\alpha > 10$, transient inertia forces start to dominate the flow; therefore, velocity profiles resemble plug-like form with flattened central profile, and flow reversal areas are also observed due to harmonic contributions coming from transient inertial effects (Womersley, 1955). In Figure 2.5, velocity profiles in a dog's femoral artery with $\alpha = 6.67$ calculated from Womersley's function at different times of a pulse cycle are given. As can be seen, especially at low flow rates, central profile is flattened, and unlike the Poiseuille flow, flow reversal is frequently observed throughout the pulse cycle. On the other hand, increasing flow rate at the systolic phase makes the steady flow component more dominant, which dampens the harmonic fluctuations and decreases the effects of transient inertial forces due to increasing effect of steady inertial forces. Therefore, velocity profiles are no longer plug-like, but more parabolic instead.

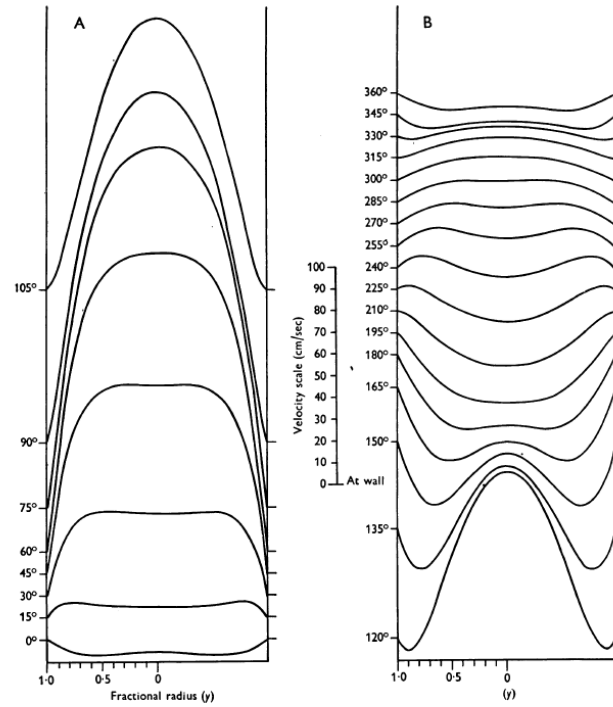


Figure 2.5. Womersley velocity profiles in a dog's femoral artery (Womersley et al., 1957).

Although *Womersley* profile is necessary to present transient effects especially for large α values, applicability and implementation of Womersley equation as an inlet boundary condition can be difficult because of the Bessel functions and imaginary numbers that it contains (Campbell et al., 2012; Impiombato et al., 2021). Therefore, in literature, most of the studies utilize *Plug* or *Parabolic* profiles with long entrance lengths to obtain fully developed condition, rather than the *Womersley* profile, which increases the computation time (Stamatopoulos et al., 2010). Indeed, necessary entrance length to obtain fully developed conditions is also a controversial issue. In general, researchers concerned about the inlet velocity boundary conditions and to be on the safe side, they tend to be extend the size of entrance region to ensure fully developed conditions (Madhavan and Kemmerling, 2018). In literature, recommended entrance length values to reach the fully developed state are significantly large (Durst et al., 2005; Salman et al., 2019). On the other hand, Hoi

et al. (2010) reported that an entrance length at least three diameters of the artery is sufficient to avoid negligible errors in hemodynamics of the carotid arteries (Hoi et al., 2010). However, from a different point of view, Madhavan and Kemmerling (2018) stated that in the actual human arterial system, obtaining the fully developed hemodynamic conditions is not realistic due to the orientation of the vasculature, such as the thoracic aorta is located immediately distal to the heart. Campbell et al. (2012) hypothesized that *Womersley* and *Parabolic* inlet velocity BCs give nearly the same result in carotid bifurcation, where $\alpha = 4.1$ and average radius is 3 mm. However, they highlighted that the results are not applicable for large arteries like aorta, in which α is larger than 10, and they require further studies. In 2019, Wei et al. (2019) stated that no significant difference between realistic, *Womersley* and *Parabolic* inlet profiles while *Plug* is notably different than the others for Fontan hemodynamics.

For determining patient-specific outlet pressure BC, a catheter can be placed inside AAA sac, however this invasive procedure is not preferred by clinicians during AAA repair (Chandra et al., 2013). Alternatively, a noninvasive method can be applied to obtain patient-specific outlet pressure. van't Veer et al. (2008) compared noninvasive brachial cuff blood pressure measurements with invasive catheter pressure measurements inside AAA sac. Brachial cuff pressure measurements resulted in 5% underestimation for systolic phase, and 12% overestimation for diastolic phase compared to the intraluminal pressure in AAA. Using these correlations, a patient-specific estimation of fluid outlet pressure can be predicted noninvasively. On the other hand, in literature, a constant reference pressure of 0 Pa at the outlet is utilized, which is a frequently utilized approach in literature for hemodynamic studies (Qiu et al., 2018; Kenjeres and Loo, 2014; Kanaris et al., 2012; Reza and Arzani, 2019).

2.1.4 Modeling non-Newtonian fluid viscosity

Computational fluid dynamics (CFD) simulations are performed to numerically determine the flow variables such as flow velocity, pressure and WSS by modeling the fluid viscosity. Blood is a concentrated suspension of various cellular elements, which are red blood cells (RBCs), white blood cells (WBCs) and thrombocytes, inside the plasma which is composed of 93% water and 3% particles, which are organic molecules, electrolytes, proteins and wastes gathered from organisms (Bessonov et al., 2016). The plasma behavior is very similar to a Newtonian fluid. However, at very low shear rates, non-Newtonian behavior of blood becomes more apparent (Young, 1979). Through the arterial system, shear rate might reach 1200 s^{-1} , while through small size vessels or regions of stable recirculation and stagnation, like downstream of a stenosis and inside an abdominal aortic aneurysm, the shear rate might be significantly small. At shear rates less than 100 s^{-1} , RBCs aggregate and form rouleaux, which is rod shaped stacks of individual cells (Bessonov et al., 2016). Rouleaux aggregation disperses as the shear rate increases, reducing the viscosity of blood. The resulting shear-thinning behavior caused by rouleaux disaggregation in blood plasma is the principal cause of the non-Newtonian behavior of blood. The shear-thinning behavior of blood is presented in Figure 2.6. On the other hand, behavior of RBCs cannot be fully characterized by viscous phenomenon because they can be regarded as fluid filled elastic cells (Bilgi and Atalık, 2020; Bodnar et al., 2011). During the aggregation of RBCs at low shear rates, they store elastic energy, leading an elastic behavior. Albeit the storage capability is no longer applicable for high shear rates due to disaggregation of rouleaux. Therefore, at low shear rates, blood exhibits a viscoelastic nature due to RBCs viscous shear-thinning and elastic properties (Bodnar et al., 2011).

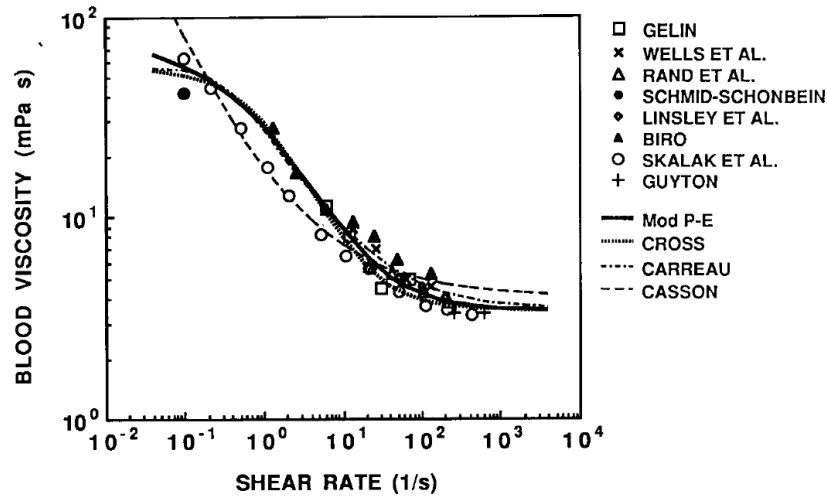


Figure 2.6. Blood viscosity vs. shear rate. The percentage of hematocrit is in the range of 33 - 45 (Cho and Kensey, 1991).

Modeling the blood as a Newtonian fluid is a common approach for the AAA flow. Blood mass density is usually taken as 1.05 g/cm^3 with a constant dynamic viscosity (μ) of 0.035 Poise (Chandra et al., 2013). Khanafer et al. (2006) compared Newtonian and non-Newtonian fluid models for the same AAA geometry and stated that the maximum pressure and maximum WSS differences were 2.53% and 26.7%, respectively. The higher difference in maximum WSS is due to the effect of near-wall turbulence which is underestimated by Newtonian models. Karimi et al. (2014) studied several rheology models which are Cross, Power, Modified and Generalized Power, Carreau, Carreau-Yasuda and three Casson variants, to investigate the flow through a patient-specific aorta with bifurcation. According to their results, the largest WSS deviations from Newtonian model occurs at bifurcation area at diastolic flow rate, where shear rates are significantly small. Also, they reported that all rheology models are well-in-line with each other, except the Cross model. Another patient-specific study for abdominal aorta bifurcation area is conducted by Skiadopoulos et al. (2017). The differences between instantaneous WSS distributions and WSS parameters such as OSI and TAWSS are compared for Newtonian, Casson and Quemada models. They reported that, Casson and Quemada

models demonstrate good agreement and Newtonian model can be utilized for high flow and shear rates. In a numerical pipe flow study conducted by Jahangiri et al. (2018), among many rheology models such as Power, Generalized Power, Carreau, Carreau-Yasuda, Walburn Schneck and Modified Casson variants, Generalized Power model give unexpected result, while the others obtain graphically same velocity profiles. Liepsch et al (2018) performed a numerical study on a patient-specific intracranial aneurysm by using Bird-Carreau, Casson, Power, Local Viscosity models and compared the results with Newtonian model. Results demonstrate that, flow patterns are similar for all models; however, an average 12% difference between shear-thinning and Newtonian models is observed from monitor points. It is reported that; Newtonian rheology model might overestimate atherosclerotic lesion generation due to predicting highly oscillatory WSS patterns. Medienta et al. (2020) performed a numerical study in a stenosed carotid artery model. WSS parameters such as OSI and TAWSS obtained by Casson, Carreau, Quemada, Power and Newtonian models are compared, and 12% difference in OSI between Newtonian and non-Newtonian models is reported. They concluded that, Newtonian model can be utilized, but in low TAWSS regions, non-Newtonian models should be used. Molla and Paul (2012) have performed a numerical study by using Large Eddy Simulations (LES) to understand the effect of rheology model on turbulent flows. Carreau, Modified Casson, Cross, Quemada and Power models are utilized and shear rate and stress values are compared, together with turbulence parameters such as turbulent kinetic energy (TKE). They reported that, at the downstream of stenosis, shear-thinning models reduce the TKE and extend the recirculation zone.

2.1.5 Important hemodynamic parameters

WSS and OSI are important hemodynamic parameters in turbulent AAA flow. The increase in maximum aneurysm diameter leads to additional turbulence-induced stresses, and increased stresses result in increased diameter, which is a self-

perpetuating mechanism for further dilatation. In a rigid walled CFD simulation, laminar and turbulent flow models are compared and it is stated that the inclusion of turbulent effects resulted in 32.5% and 23.6% increased pressure and WSS at the distal end of AAA, respectively (Khanafar et al., 2007).

Les et al. (2010) investigated patient-specific AAA hemodynamics using high-resolution CFD simulations (about 8-million mesh elements), hypothesizing that physical lower limb exercise might decrease the growth rate of AAA, since exercise resulted in a high amplitude WSS pattern and lowered OSI on AAA wall. Moderate turbulence was observed in AAA during exercise, while resting conditions led to mild turbulence. Rest-to-exercise TAWSS changes were found to be statistically significant. For example, at supraceliac level, TAWSS at rest was 3.6 dyn/cm², and it increased to 9.2 dyn/cm² during the exercise. At mid-aneurysm level, TAWSS at rest was 7.3 dyn/cm², while at exercise it was 21.7 dyn/cm². OSI values at rest were 0.28 and 0.27 for supraceliac and mid-aneurysm locations, respectively. These OSI values decreased to 0.18 and 0.21 during the exercise.

Qiu et al. (2018) performed CFD simulations using three ruptured and one non-ruptured patient-specific AAA models. The rupture sites were found to be near the fluid stagnation regions which have nearly zero WSS with high WSS gradients (WSSG). Helicity (i.e. dot product of the velocity and vorticity) was introduced as a quantitative measure for rupture risk assessment, since the rupture sites had zero helicity representing a purely axial or circumferential flow. For three ruptured AAAs, common iliac arteries had lower WSS compared to non-ruptured AAA. In the aneurysm sac, rupture sites had WSS lower than 0.1 Pa, and no rupture occurred at the location with peak pressure or large pressure gradient. In Figure 2.7, the distribution of WSS and OSI are provided on a patient-specific model. Most researchers agree that the locations with low WSS, high OSI and high ECAP are prone to thrombus formation and have a higher risk of rupture (Les et al., 2010; Kelsey et al., 2016). On the other hand, in some studies reporting controversial results (Arzani et al., 2014; Mohamied et al., 2015), it is stated that low WSS and high OSI regions do not coincide with thrombus deposition sites. Therefore, the exact

effect of these hemodynamic parameters on the rupture mechanism is not yet fully understood.

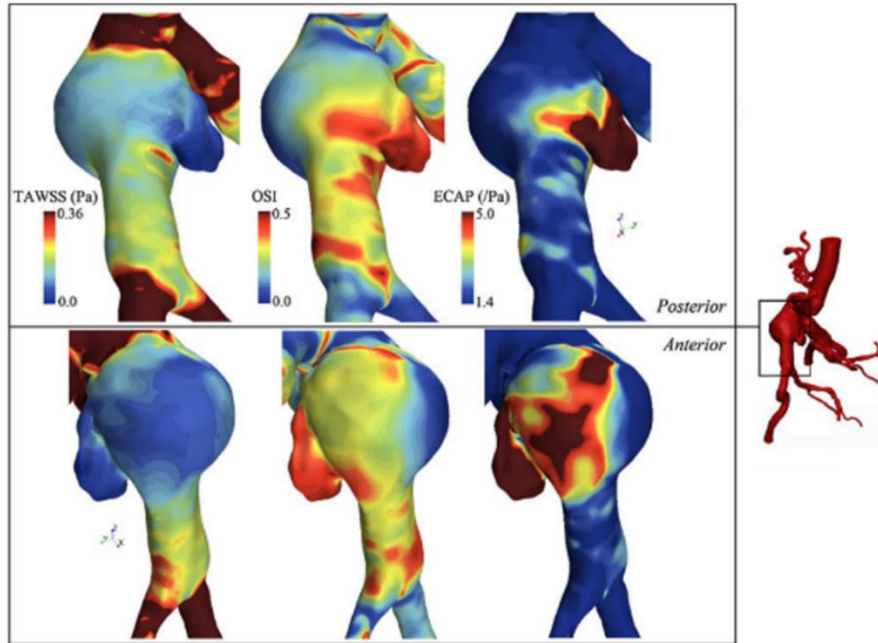


Figure 2.7. TAWSS, OSI and ECAP contour plots on a patient specific AAA model (Kelsey et al., 2016)).

2.2 Experimental studies on hemodynamics of AAAs

Hemodynamics of the abdominal aortic aneurysms is quite complex primarily due to the nature of the system involving irregular shape and flexible arteries, three-dimensional physiological and turbulent flow, and non-Newtonian working fluid of blood. As computational methods have widely been used in investigation of hemodynamics and mechanical behavior of arterial tissue, the experimental techniques are also utilized in characterization of flow dynamics through abdominal aortic aneurysms. Both approaches are crucial and complement each other with offering in depth analysis where the level of its intensity and the corresponding results depend on the assumptions in computational models and simplifications in experimental methods.

In that sense, in line with the aforementioned computational studies, many experimental investigations of the hemodynamics through AAAs have been conducted in literature, and various qualitative and quantitative flow measurement techniques have been utilized for that purpose so far. In early studies, qualitative flow visualization techniques have been widely implemented, in which using localized injections, the patterns of dye as streaklines were generated (Ku et al., 1989). This simple method provides insights on overall behavior of flow structure in the region of interest. In terms of detailed velocity information in the abdominal aortic aneurysms, non-intrusive and quantitative techniques such as Magnetic Resonance Imaging (MRI) and Doppler Ultrasound Imaging (DUS) are appropriate for detailed anatomical analysis by means of tomographic slices are provided. In MRI based system encoding the flow velocity is obtained by means of the changes in MR signal phase along a magnetic field gradient (Wang et al., 2016). Moreover, for experimental studies, laser-based techniques including Laser Doppler Anemometry (LDA) and Particle Image Velocimetry (PIV) are also implemented for detailed velocity information. In LDA, pointwise velocity measurements are performed by means of Doppler effect using two laser beams for each velocity component. This method has very high spatial and temporal resolutions (\sim kHz) and allows to measure reverse flow and turbulent fluctuations, which is quite critical for understanding the growth and the rupture mechanics of AAAs (Yip and Yu, 2002). In PIV, two component velocity information on 2-D plane is obtained at relatively lower temporal resolution (\sim Hz) using two laser sheets and an advanced camera, where in stereoscopic PIV three-velocity components are obtained on 2-D plane using two cameras. This method is quite effective in understanding the key parameters of disturbed hemodynamics of AAAs since it provides detailed velocity field information and therefore have widely been used recently (2-D PIV, Deplano et al., 2013), (Stereo PIV, Chen et al., 2014). For the quantification of three-dimensional velocity field, PIV offers two recent state of the art versions: Tomographic PIV and Holographic PIV, which are expected to appear in the studies of disturbed hemodynamics through AAAs in near future. Tomographic PIV has

recently been applied to the hemodynamics of intracranial aneurysms (Roloff et al., 2017), (Roloff et al. 2018).

Experimental studies on blood flow inside AAAs is primarily categorized and populated in two major groups: the properties of the aorta phantom used and conditions of the flow. Major consideration for the aorta phantom are elasticity of arterial wall and geometry of the aorta (change in wall diameter, aneurysm shape, artery bifurcation, etc.) whereas major considerations in flow conditions, include flow waveform (steady or physiological), type of working fluid (Newtonian, non-Newtonian), and pulse rate (exercise or resting). Considering the overall flow structure in aorta and AAAs, fully developed flow at the entrance of the AAA expands and creates counter rotating recirculation along with a jet flow at the center, which are due to the adverse pressure gradient imposed at the aneurysm bulge. Location and strength of the recirculation vortex primarily depend on the inlet flow waveform, bulge shape, and elasticity of arterial wall. For the steady inlet flow condition, which is not realistic, the recirculating vortex is larger in extent in average and located closer to downstream of the bulge, whereas in physiological flow condition recirculation region is alternating and moving back and forth due to periodic flow condition. It is also indicated that the spatial extent, the location, and the strength of the recirculation vortex are significantly affected by the bulge shape and the wall rigidity (Yu, 2000) (Egelhoff et al., 1999) (Deplano et al., 2007) (Meyer et al., 2011).

Therefore, because of the complexities in geometry and flow conditions, the experimental set up for AAA investigations need to be designed to mimic natural realistic in-vivo conditions within AAA as close as possible to obtain accurate results. A typical experimental set up for the analysis of hemodynamics contains flow circulatory system including pump, piping, and pressure compliance, test section that contains artery model, blood mimicking fluid, and flow measurement systems as briefly mentioned previously such as MRI, LDA or PIV.

In numerical studies, many researchers have focused on high, low and oscillating wall shear stress values and the corresponding gradients (WSSG), along with the pressure fluctuations, and claimed that high and low wall shear stresses and pressure fluctuations created by flow are related with aneurysm growth and rupture (Khanafar et al., 2007), (Kelsey et al., 2016), (Qiu et al., 2018). In these studies, on hemodynamics inside AAA, the distal end of aneurysm is reported to be the critical location for the rupture (Stamatopoulos et al., 2010), (Egelhoff et al., 1999), (Yu, 2000). Considering the experimental studies alone, researchers have generally reported the results of the hemodynamics in AAA in terms of velocity and vorticity parameters (Salsac et al., 2006), (Stamatopoulos et al., 2010) obtained using several vortex identification techniques, such as swirling strength (Deplano et al., 2007). Swirling strength, λ_{ci} , is obtained by calculating the imaginary part of the complex eigenvalue of velocity gradient tensor, which is $\mathbf{D} = \nabla \mathbf{u}$ and the idea which is based on decomposition of that velocity gradient tensor in Cartesian coordinates. The swirling strength of the vortex is defined by λ_{ci} , while λ_{ci}^2 is called as enstrophy, which is energy of vorticity. Defining vortices in that manner decreases the background noise; therefore, the vortical structures can easily be identified (Zhou et al., 1999). In hemodynamic investigations, this phenomenon is critical in eliminating the regions having vorticity without local spiraling motion like shear layers (Deplano et al., 2012). Obtaining WSS by post-processing PIV data is quite challenging due to the reflection problems at the solid-liquid interfaces; i.e., laser light scattering at the solid-liquid interface creates underestimation in WSS results during post processing (Stamatopoulos et al., 2010). Chen et al., (2014) claims that more accurate WSS calculations can be performed using Stereo PIV data.

In most of the experimental studies, rigid axisymmetric models were used to investigate the hemodynamics in aneurysm bulge (Yu, 2000), (Salsac et al., 2006), (Stamatopoulos et al., 2010). Deplano et al. (2007), and Meyer et al. (2011) have tested two aneurysm models one having rigid and the other with compliant walls to quantify the effect of wall compliance on hemodynamics. The rigid aneurysm was made of glass while the compliant one was made of molded polyurethane, and both

had the identical geometry as a simple bulge for comparison purposes. As can be seen in Figure 2.8, there is a significant difference between the flow fields inside both of the aneurysms. In rigid model, there is only viscous dissipation, while in compliant model, viscoelastic dissipation is also observed, which is indicated as more critical. During the accelerating phase of the cycle, compliant walls absorb kinetic energy in the potential energy form, leading the walls become expanded. While the flow is decelerating, this stored kinetic energy retracts the walls. This expansion and retraction contribute the progression of vortices at the distal end of aneurysm during the deceleration phase. The flow rates are higher in deceleration phase for the compliant wall than the rigid wall, which is leading to vortex shedding and consequently causing more interaction with the walls of aneurysm model. In Figure 2.8, generation of the vortex shedding is also presented. They conclude that increasing wall compliance causes collision of vortices with the walls, increasing both the local pressures and wall stresses especially at the distal end (Deplano et al., 2007), (Meyer et al., 2011).

For mimicking the shear stress and shear strain rate relation of blood, Deplano et al. (2014) have used Xanthane Gum dissolved in aqueous solutions of glycerol, a shear thinning fluid, where they report that shear thinning fluid model imposes higher shear stress values throughout the aneurysm bulge than Newtonian model. They conclude that the rheology of working fluid affects the hemodynamics inside aneurysm model, and should be taken into account for more realistic experimentation. On the other hand, in another study which is performed on a curved artery model with again a shear thinning fluid, mixture of fluids like Xanthane Gum, glycerin, water and sodium iodide (Najjari et al., 2016). The results are very similar to the studies for curved arteries with Newtonian fluids, concluding that for large arteries with large flow rates, rheology of the blood does not affect the flow structure. However, at that point it is important to note that, they have utilized comparatively high sodium iodide concentration in their mixture than required to resolve the refractive index problems, leading that their working fluid is less viscoelastic than the blood.

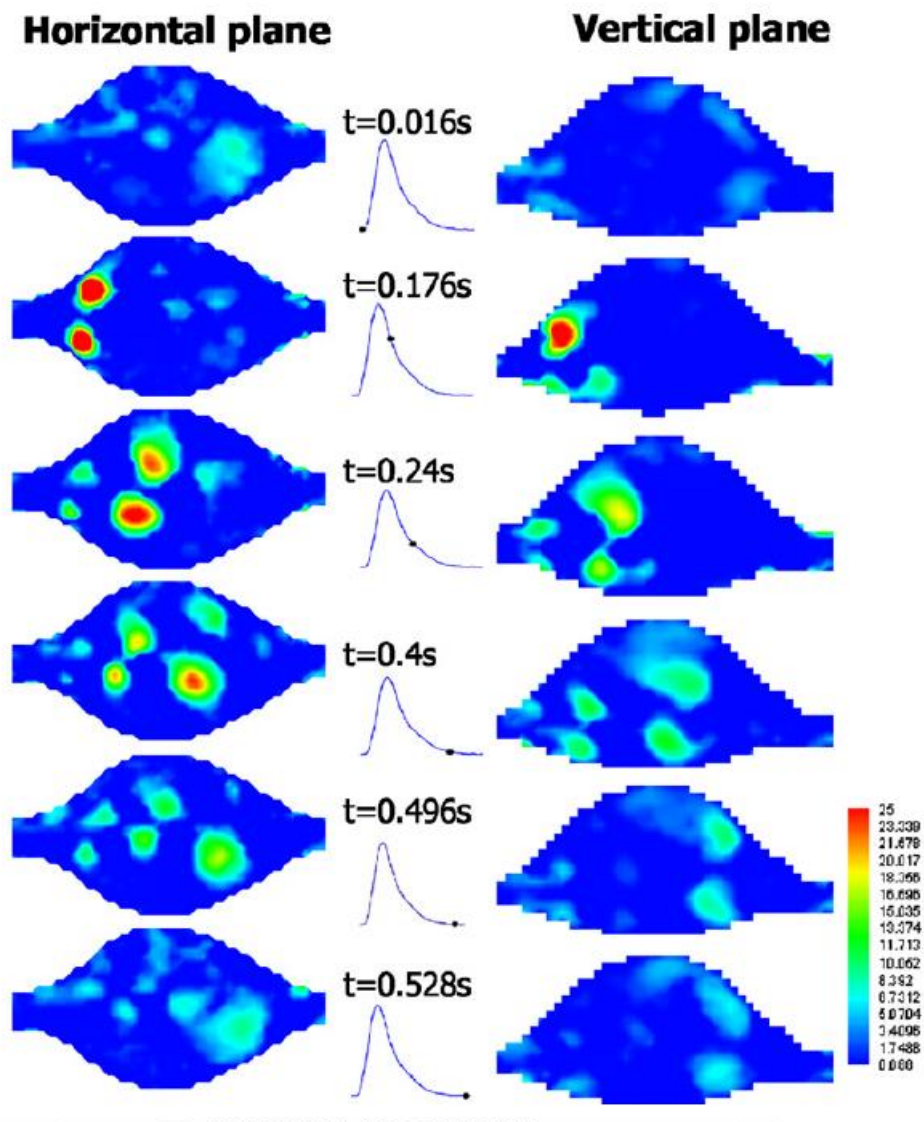


Figure 2.8. Temporal evolution of the swirling strength λ_{ci} at different time instants in a. the rigid model and the compliant model in horizontal plane, and b. the compliant model at horizontal and vertical planes (Deplano et al., 2016)

CHAPTER 3

METHODOLOGY

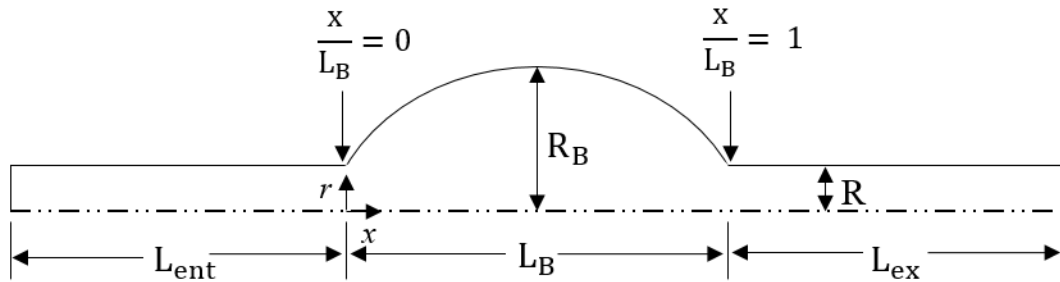
3.1 Numerical Simulation Details

3.1.1 Effect of Inlet Velocity Profile and Entrance Length Study

The idealized axisymmetric abdominal aortic aneurysm models used in this study are given in Figure 3.1. Geometries are two dimensional axisymmetric, and created based on those used in Stamatopoulos et. al's study (2010). Inlet and exit parts are straight and cylindrical, while the aneurysm bulge is elliptical with a major radius of 0.034 m. The artery and bulge radii are, $R = 9$ mm and $R_B = 22$ mm. The lengths of the bulge and exit part are $L_B = 62$ mm and $L_{ex} = 206$ mm, while entrance lengths, L_{ent} , are different. As presented in Figure 3.1b, entrance lengths are equal to $L_{ent} = D, 3D, 11D$ and $50D$, from top to bottom and left to right, respectively. At the inlet of the models with $L_{ent} = D, 3D$ and $11D$, all the velocity profiles, *Womersley*, *Parabolic* and *Plug*, are applied. To compare the results obtained with three different entrance lengths and velocity profiles, a Base condition is generated with the model having an entrance length $L_{ent} = 50D$ with only *Plug* velocity profile at the inlet. The Base condition is checked to ensure the fully developed condition at each time steps before entering the aneurysm sac. In Table 3.1, the models with applied inlet velocity profiles are also presented. The vessel and bulge dimensions of all models are consistent with realistic arteries and aneurysms (Brewster et al, 2003). Actually, the idealization of aneurysm bulge rather than utilizing patient-specific geometry may fail to simulate exact aneurysm hemodynamics. However, an idealized axisymmetric geometry is sufficient for a comparative parametric study to

characterize the behavior of a vast number of rheology models at different inlet flow waveform patterns, which is actually independent of geometric details.

In the current study, simulations are performed at two mean Reynolds numbers, $Re_m = U_m D / \nu = 340$ and 1160 , based on the mean flow velocity, where $U_m = 0.065$ and 0.22 m/s are the time averaged velocities over one period and $\nu = 3.14 \times 10^{-5}$ m/s² is the kinematic viscosity. The period of all waveform patterns is the same and equal to $T = 1$ s, yielding a Womersley number of $\alpha = 0.5D\sqrt{\omega/\nu} = 12.14$, where D is the artery diameter, ω is the frequency and equals to $2\pi/T$.



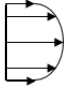
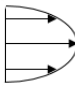
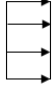
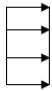
a.



b.

Figure 3.1. Sectional views of flow domains for aneurysm models, which is out of scale. Flow is from left to right.

Table 3.1. Aneurysm models with respect to entrance lengths and applied inlet velocity profiles.

L_{ent} (m)	Inlet Velocity Profile		
D, 3D, 11D		Womersley	
		Parabolic	
		Plug	
50D		Plug	Base Case

The waveform pattern for two flows are adapted from the study of Finol and Amon (2001) and the same as presented in Figure 3.2a; however, diastolic flow rate for $Re_m = 1160$ is higher. The reason of using two waveform patterns is investigating the effect of increasing mean flow rate on applicability of *Parabolic* and *Plug* inlet velocity boundary conditions, rather than Womersley profile. In Figure 3.2b, Womersley profiles obtained by corresponding waveforms at specified time instants are demonstrated. As can be seen from figure, with increasing flow rate, profiles obtained by Womersley formula are very similar to Parabolic form. Cardiac cycle is divided into six phases, which are early/mid/late systole and diastole. Location of each phase in the cardiac cycle is shown in Figure 3.2a, while time ranges for these phases are presented in Table 3.2. In literature, generally a physiological flow rate is utilized at the inlet as the inlet boundary condition. However, several studies apply a physiological pressure pattern at the inlet, instead of flow rate (Les et al., 2010; Joly et al., 2018; Fonken et al., 2021).

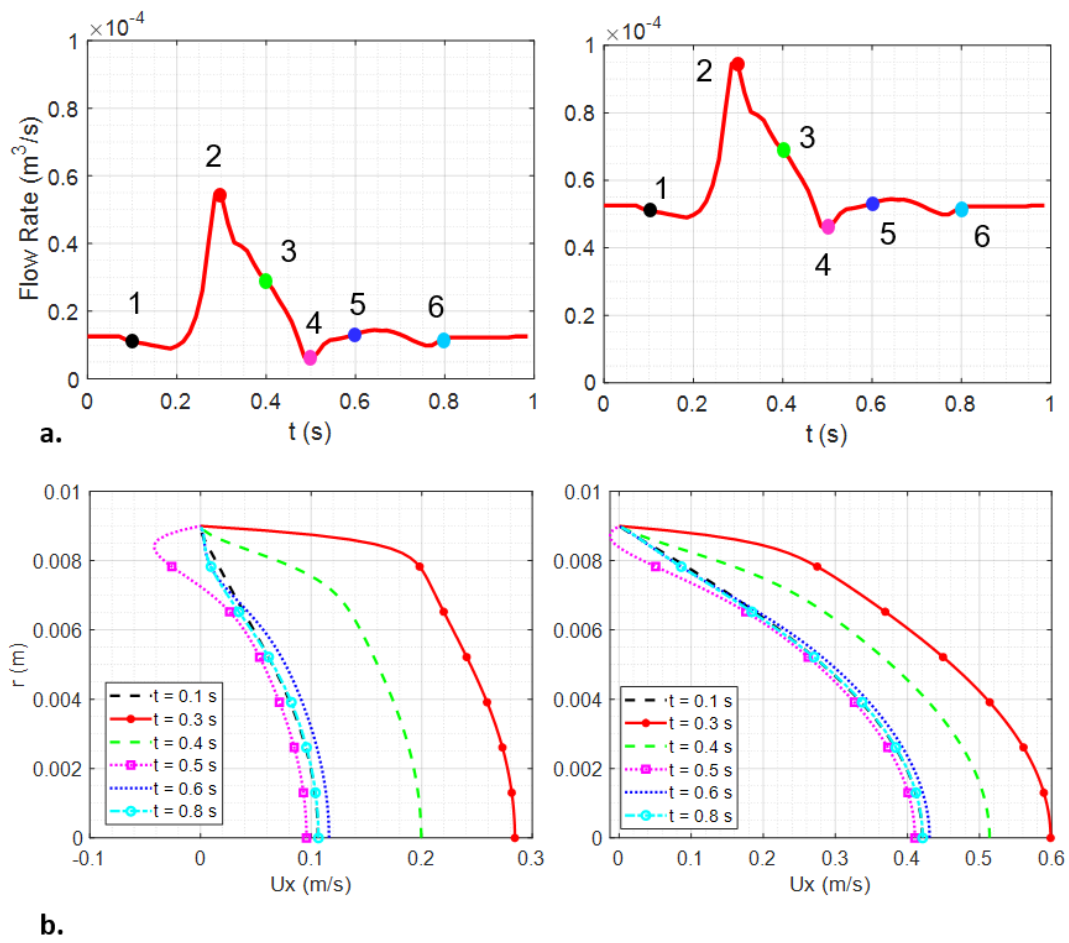


Figure 3.2. a. Physiological inlet flow rate waveforms for $Re_m = 340$ and 1160 , from left to right, respectively b. Womersley velocity profiles for those waveforms at selected time instants (Finol and Amon, 2001)

Table 3.2. Phases of cardiac cycle with period $T = 1$ sec.

Number	Phase	Time interval
1	Late Diastole	0 – 0.18
2	Early Systole	0.18 – 0.3
3	Mid Systole	0.3 – 0.4
4	Late Systole	0.4 – 0.5
5	Early Diastole	0.5 – 0.76
6	Mid Diastole	0.76 - 1

At the inlet, *Womersley*, *Parabolic* and *Plug* profiles are specified according to the waveform which is considered to be physiologic. *Plug* profile is actually the uniform velocity at the inlet, while *Parabolic* and *Womersley* velocity profiles are defined by Eqn. (1) and (2), respectively

$$u(r, t) = \frac{2Q(t)}{\pi R^2} \left(1 - \left(\frac{r}{R}\right)^2\right) \quad (3.1)$$

$$u(r, t) = \frac{2C_0}{\pi R^2} \left(1 - \left(\frac{r}{R}\right)^2\right) + \sum_{n=1}^N \frac{C_n}{\pi R^2 \left(1 - \frac{2J_1\left(i^{\frac{3}{2}}\alpha_n\right)}{i^{\frac{3}{2}}\alpha_n J_0\left(i^{\frac{3}{2}}\alpha_n\right)}\right)} \left[1 - \frac{J_0\left(\alpha_n \frac{r}{R} i^{3/2}\right)}{J_0\left(\alpha_n i^{3/2}\right)}\right] e^{i\omega_n t} \quad (3.2)$$

where α is Womersley number, ω is frequency, J_0 and J_1 are the Bessel function of the first kind of order zero and first, respectively (Womersley, 1955). Q is the

physiologic flow rate, which is presented in Figure 3.2. To obtain Womersley profile, it is necessary to write the flow rate, $Q(t)$, in the harmonic form as in Eqn. (3.3)

$$Q(t) = \sum_{n=0}^N C_n e^{in\omega t} \quad (3.3)$$

where N is the total number of harmonic coefficients. A Fourier series decomposition of the flow waveform should be performed to obtain Fourier coefficients, C_n . For that purpose, Fast Fourier Transform (FFT) method is applied to the available flow rate data, as presented in Figure 3.2a. C_0 and C_n 's are the Finite Fourier Transform (FFT) coefficients of that flow rate, while the term $n = 0$ corresponds to a steady pressure gradient. Therefore, in Eqn. (3.2), the first term on the right hand side of the equation is equal to steady Poiseuille equation (Womersley, 1955), while the second term is obtained from harmonic contribution. Detailed derivation of Womersley profile, Matlab code and its application to OpenFOAM is explained in Appendix A in detail.

The wall boundaries are taken as rigid and no-slip boundary condition is applied, elastic effects of walls are neglected. Excluding the compliance effect with utilizing the walls as rigid is quite common (Arzani et al., 2014; Finol and Amon, 2001). Moreover, walls are not moving during cardiac cycle, i.e.; the artery is taken as stationary. Reference pressure at the outlet is set to zero, which is a frequently utilized approach in literature for hemodynamic studies (Qiu et al., 2018; Reza and Arzani, 2019). Flow is considered to be laminar (Scotti et al., 2018) due to Reynolds number is not sufficient to reach turbulent conditions even at peak systolic phase, $Re_{\text{peak}} = 2000$. In general, blood has non-Newtonian characteristics where the viscosity decreases with increased shear rate. However, at shear rates higher than 100 s^{-1} , blood shows Newtonian characteristics, and for large arteries, such as the one used in this study, it can be assumed as Newtonian (Reza and Arzani, 2019) with a kinematic viscosity of $3.45 \times 10^{-6} \text{ m}^2/\text{s}$, and density of $1000 \text{ kg}/\text{m}^3$.

Numerical simulations are conducted by using OpenFOAM version 8 (openfoam.org). The governing equations are discretized using second order implicit discretization in time and second order central discretization in space. pimpleFoam solver is selected because of enabling automatic control of the time step to achieve a given maximum Courant number (C_{max}) for each case. To select an appropriate C_{max} that can provide accurate solutions, five different Courant numbers, which are $C = 0.25, 0.5, 1, 2,$ and 4 were tested, and higher Courant numbers are failed to provide stable solutions. For all Courant numbers, the same velocity profile was obtained, meaning that solutions until $C_{max} = 4$ give accurate results for the current study. However, C_{max} was taken as 1 to be on the safe side. 30 iterations are performed at each time step, and the solution is considered to be converged when residuals for axial velocity component and pressure are less than 10^{-4} . To ensure the convergence, calculations are repeated for six cardiac cycles.

To select a suitable mesh, a mesh independence study is performed using four structured meshes created, as shown in Fig. 3.3. Figure 3.4a shows axial velocity profiles at the mid-plane of the aneurysm and swirling strength, λ_{ci} contours obtained by using these meshes at the peak systole and early diastole. In Figure 3.4b, OSI and ECAP distributions obtained by those meshes are provided. As from those figures, the axial velocity profiles are identical and swirling strength contours are very similar for the Mesh 3 and 4. Albeit OSI and ECAP distributions are very sensitive to the mesh selection, Mesh 3 and 4 obtain very similar OSI and ECAP distribution. Therefore, Mesh 3 is evaluated to be suitable and used to perform the simulations in the present study.

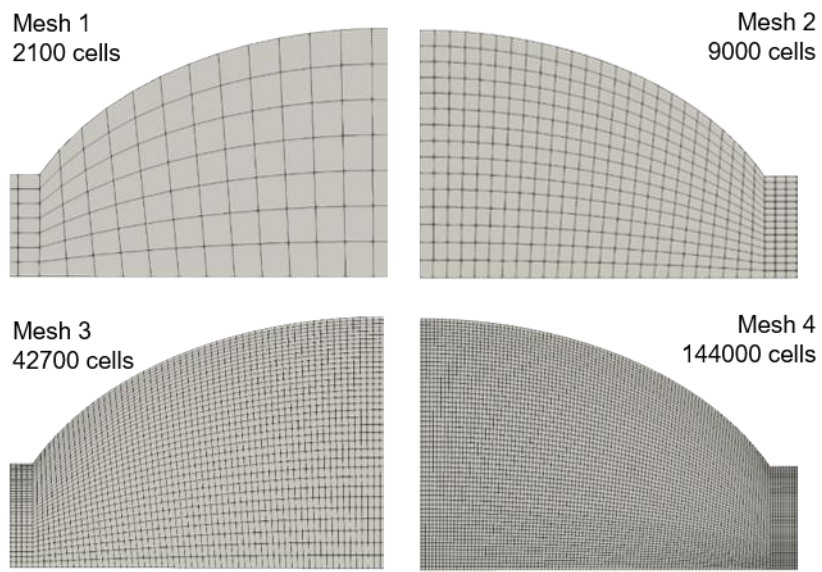


Figure 3.3. Four meshes generated for mesh independency check

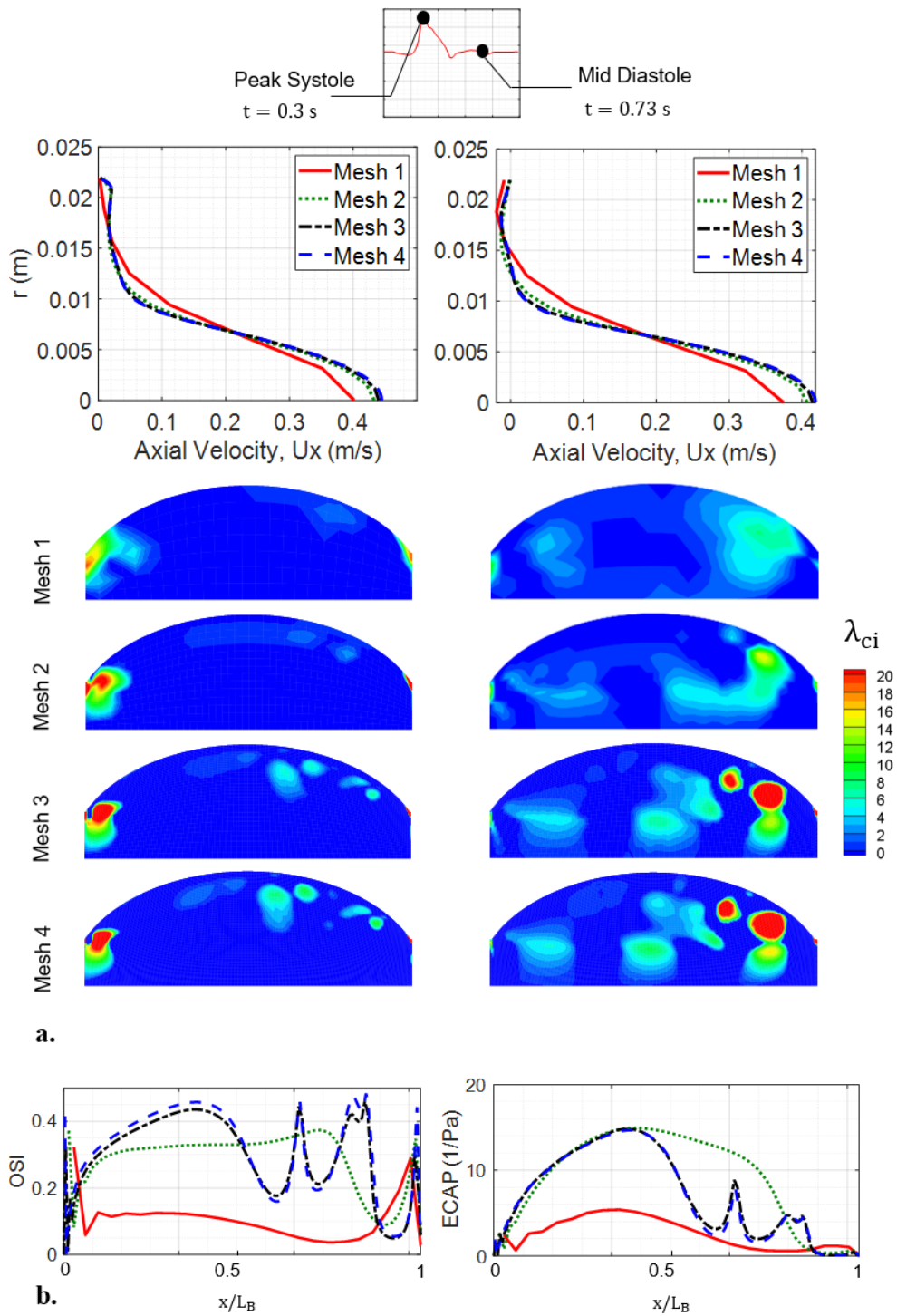


Figure 3.4. a. Axial velocity profiles obtained with four different meshes at $x/L_B = 0.5$, and swirling strength contours, b. OSI and ECAP distributions of four meshes for $Re_{mean} = 1160$

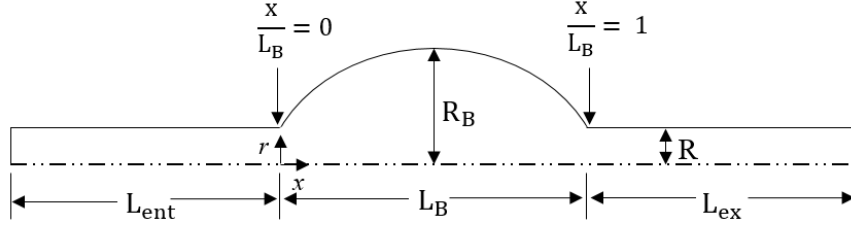
3.1.2 Effect of Infrarenal Flow Waveform Pattern on Rheology Model Selection and AAA Hemodynamics Study

The idealized abdominal aortic aneurysm (AAA) model used in this study is given in Fig. 3.5a. Geometry is two-dimensional, axisymmetric, and created based on those used in Stamatopoulos et. al's study (Stamatopoulos et al., 2010). Inlet and exit parts are straight and cylindrical, while the aneurysm bulge is elliptical with a major radius of 0.034 m. The lengths of the entrance part, bulge and exit part are $L_{ent} = 935$ mm, $L_B = 62$ mm and $L_{ex} = 206$ mm. The artery and bulge radii are, $R = 9$ mm and $R_B = 22$ mm. The vessel and bulge dimensions are consistent with realistic abdominal artery and aneurysm (Les et al., 2010; Brewster et al., 2003). Actually, the idealization of aneurysm bulge rather than utilizing patient-specific geometry may fail to simulate exact aneurysm hemodynamics. However, an idealized axisymmetric geometry is sufficient for a comparative parametric study to characterize the behavior of a vast number of rheology models at different inlet flow waveform patterns, which is actually independent of geometric details.

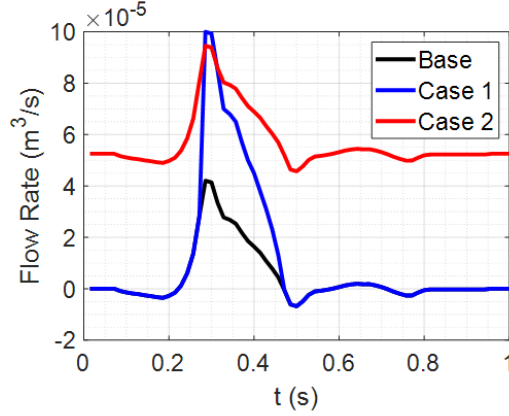
To investigate the effect of flow waveform on hemodynamics and rheology model selection, three different patterns named as Base, Case 1 and 2, shown in Figure 3.5b are considered. The Base waveform, suggested by Finol and Amon (2001), starts from zero diastolic flow rate and reaches 42 ml/sec peak systolic flow rate. For the Case 1, diastolic flow rate is kept the same with Base case but peak systolic flow rate is increased, while for Case 2 the amplitude of peak systole is the same with Base, with increased diastolic flow rate. Therefore, the effect of increasing peak systolic flow rate and diastolic flow rate is checked using Case 1 and 2, respectively. The period of all waveform patterns is the same and equal to $T = 1$ s, yielding a Womersley number of $\alpha = 0.5D\sqrt{\omega/\nu} = 12.14$, where D is the artery diameter, ω is the frequency and equals to $2\pi/T$, and $\nu = 3.45 \times 10^{-6}$ m²/s, ν is the kinematic viscosity of the Newtonian model. The mean Reynolds numbers for the waveforms are $Re_m = U_m D/\nu = 120, 250$ and 1160 , where $U_m = 0.02, 0.04$ and 0.22 m/s are the time averaged velocities over one period for Base Case 1 and 2, respectively.

Unsteady plug flow is specified at the inlet, and through a number of preliminary runs, the entrance length is selected as 50 times the vessel diameter, which is sufficiently long to have fully developed condition at the bulge inlet (Madhavan and Kemmerling, 2018). A constant reference pressure of 0 Pa is specified at the outlet, which is a frequently utilized approach in literature for hemodynamic studies (Reza and Arzani, 2019). Through the preliminary runs, it is made sure that the length of the exit part is long enough such that the disturbance created by the bulge dies out before the flow reaches the outlet, enabling the use of constant pressure outlet condition. Wall boundaries are taken as rigid with no-slip boundary condition applied. Excluding the compliance effect with utilizing the walls as rigid is quite common (Finol and Amon, 2001; Arzani and Shadden, 2015).

In this study, eight non-Newtonian models, which are Carreau, Carreau-Yasuda, Casson, Quemada, Power, Cross, Simplified and Modified Cross, with details given in Table 3.3, are used. For Power model, different constants are available in literature for the same hematocrit. In the current study, Power-1 (Shibeshi and Collins, 2005) and Power-2 (Cho and Kensey, 1991) are tested by using two frequently used constants. In Table 3.3, μ is the viscosity, μ_0 and μ_∞ are the asymptotic viscosity values at zero and infinite shear rates, λ is the relaxation time constant, K is the flow consistency index and n is the power law index (Bessonov et al., 2016; Shibeshi and Collins, 2005; Cho and Kensey, 1991). For Newtonian approach, the kinematic viscosity and density of the blood are taken as 3.45×10^{-6} m²/s, and density of the blood for all models is taken as 1000 kg/m³ (Bessonov et al., 2016).



a.



b.

Figure 3.5. a. 2D axisymmetric flow domain, b. Physiological inlet flow rate waveform patterns, Base (Finol and Amon, 2001), Case 1 and 2

To account for the elastic nature of blood, the stress tensor in linear momentum equation can be decomposed into viscous and elastic parts as $\tau = \tau_s + \tau_e$. The viscous part of Oldroyd-B model is Newtonian (Bodnár et al., 2011), $\tau_s = 2\mu_s(\nabla u + \nabla u^T)$.

The elastic part satisfies following constitutive equation

$$\tau_e + \lambda_1 \left(\frac{\partial \tau_e}{\partial t} + u \cdot \nabla \tau_e - \tau_e \cdot \nabla u - \nabla u^T \cdot \tau_e \right) = \mu_e (\nabla u + \nabla u^T) \quad (3.4)$$

where μ_e is the elastic viscosity coefficient, and λ_1 is the relaxation time (Leuprecht and Perktold, 2001). For blood, $\mu_e = 0.0004 \text{ Pa} \cdot \text{s}$ and $\lambda_1 = 0.06 \text{ s}$ (Leuprecht and Perktold, 2001).

Numerical simulations are conducted by using the open source software OpenFOAM (openfoam.org). Flow is considered to be laminar (Scotti et al., 2008) due to

Reynolds number is not sufficient to reach turbulent conditions even at peak systolic phase, $Re_{\text{peak}} = 2000$. The governing equations are discretized using second order implicit discretization in time and second order central discretization in space. Among the incompressible flow solvers available in OpenFOAM, shear-thinning and Newtonian model solutions are obtained by using the pimpleFoam solver. In OpenFOAM version 8, only Carreau, Casson, Cross and Power models are available and frequently used and validated in literature (Javidi and Hrymak, 2015; Juster et al., 2014; Maazioui et al., 2021; Zheng et al., 2019). The Carreau-Yasuda, Quemada, Modified and Simplified Cross models are added in the current study. For the Oldroyd-B model simulation, the viscoelasticFluidFoam solver, which is only available in foam-extend version of OpenFOAM, is utilized. Several validation studies of this implementation can be found in literature (Habla et al., 2014; Favero et al., 2010; Guranov et al., 2013).

Maximum number of iterations performed at each time step is taken as 10, and the solutions are considered to be converged when residuals for axial velocity component and pressure are less than 10^{-4} . Time step for all simulations is selected as 10^{-5} sec, and to ensure that the time periodic state is reached, calculations are repeated for 6 cardiac cycles for shear-thinning and Newtonian models. However, examining the monitor points, 12 cardiac cycles are used to reach the time periodic state for Oldroyd-B model. To select a suitable mesh, a mesh independence study is performed using four structured meshes given in Fig. 3.6. Figure 3.7a shows axial velocity profiles at the mid-plane of the aneurysm and swirling strength, λ_{ci} contours obtained by using these meshes at the peak systole and early diastole. In Figure 3.7b, OSI and ECAP distributions obtained are provided. The axial velocity profiles are identical and swirling strength contours are very similar for meshes 3 and 4. Albeit OSI and ECAP distributions are very sensitive to the mesh selection, Mesh 3 and 4 provided very similar OSI and ECAP distributions. Therefore, Mesh 3 is evaluated to be suitable and used to perform the simulations in the present study.

Table 3.3. Selected shear-thinning rheology models (Bessonov et al., 2016; Shibeshi and Collins, 2005; Cho and Kensey, 1991, Quemada, 1978) – continued in next page

Carreau	$\frac{\mu(\dot{\gamma}) - \mu_{\infty}}{\mu_0 - \mu_{\infty}} = (1 + (\lambda\dot{\gamma})^2)^{(n-1)/2}$	$\mu_0 = 0.056 \text{ Pa} \cdot \text{s}$ $\mu_{\infty} = 0.00345 \text{ Pa} \cdot \text{s}$ $\lambda = 3.313 \text{ s}$ $n = 0.3568$
Carreau- Yasuda	$\frac{\mu(\dot{\gamma}) - \mu_{\infty}}{\mu_0 - \mu_{\infty}} = (1 + (\lambda\dot{\gamma})^a)^{(n-1)/a}$	$\mu_0 = 0.056 \text{ Pa} \cdot \text{s}$ $\mu_{\infty} = 0.00345 \text{ Pa} \cdot \text{s}$ $\lambda = 1.902 \text{ s}$ $n = 0.22$ $a = 1.25$
Quemada	$\mu = \mu_f \left[1 - \frac{1}{2} \frac{K_0 + K_{\infty} \sqrt{ \dot{\gamma} }}{1 + \sqrt{ \dot{\gamma} }} \phi \right]$	$\mu_f = 0.0012 \text{ Pa} \cdot \text{s}$ $K_0 = 4.65$ $K_{\infty} = 1.84$ $\gamma_c = 2.23 \text{ s}^{-1}$ $\phi = 0.4$
Casson	$\sqrt{\tau} = \sqrt{k_0} + \sqrt{k_1 \dot{\gamma}}$	$k_0 = 0.05 \text{ dyne/cm}^2$ $k_1 = 0.04 \text{ dyne/cm}^2$

		$\mu_0 = 0.056 \text{ Pa} \cdot \text{s}$
Cross	$\frac{\mu(\dot{\gamma}) - \mu_\infty}{\mu_0 - \mu_\infty} = \frac{1}{1 + (m\dot{\gamma})^n}$	$\mu_\infty = 0.00345 \text{ Pa} \cdot \text{s}$ $m = 1.007 \text{ s}$ $n = 1.028$
Simplified Cross	$\frac{\mu(\dot{\gamma}) - \mu_\infty}{\mu_0 - \mu_\infty} = \frac{1}{1 + m\dot{\gamma}}$	$\mu_0 = 0.103 \text{ Pa} \cdot \text{s}$ $\mu_\infty = 0.005 \text{ Pa} \cdot \text{s}$ $m = 8 \text{ s}$
Modified Cross	$\frac{\mu(\dot{\gamma}) - \mu_\infty}{\mu_0 - \mu_\infty} = \frac{1}{(1 + (m\dot{\gamma})^n)^a}$	$\mu_0 = 0.056 \text{ Pa} \cdot \text{s}$ $\mu_\infty = 0.00345 \text{ Pa} \cdot \text{s}$ $m = 3.736 \text{ s}$ $n = 2.406$ $a = 0.254$
Power	$\mu(\dot{\gamma}) = K\dot{\gamma}^{n-1}$	$K = 0.017 \text{ Pa} \cdot \text{s}^n$ $n = 0.708$ (Shibeshi and Collins, 2005) <i>or</i> $K = 0.035 \text{ Pa} \cdot \text{s}^n$ $n = 0.6$ (Cho and Kensey, 1991)

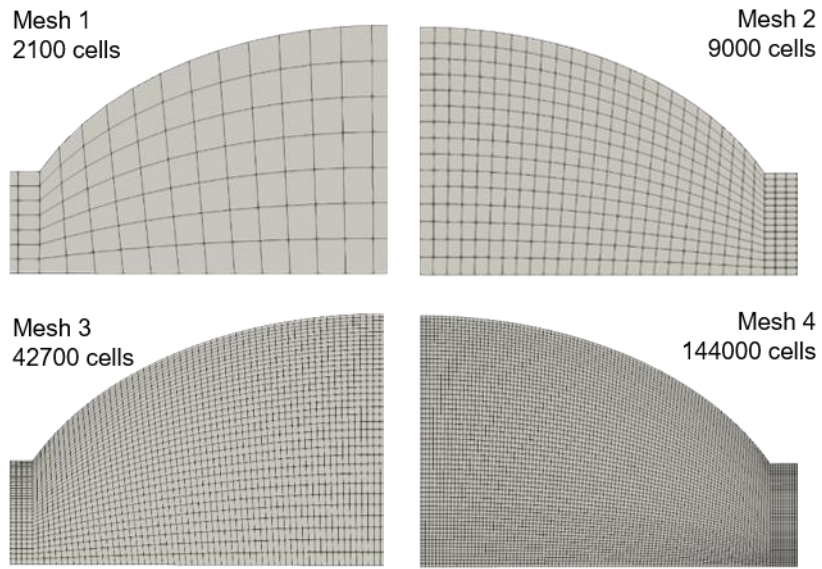


Figure 3.6. Four meshes used for the mesh independence check

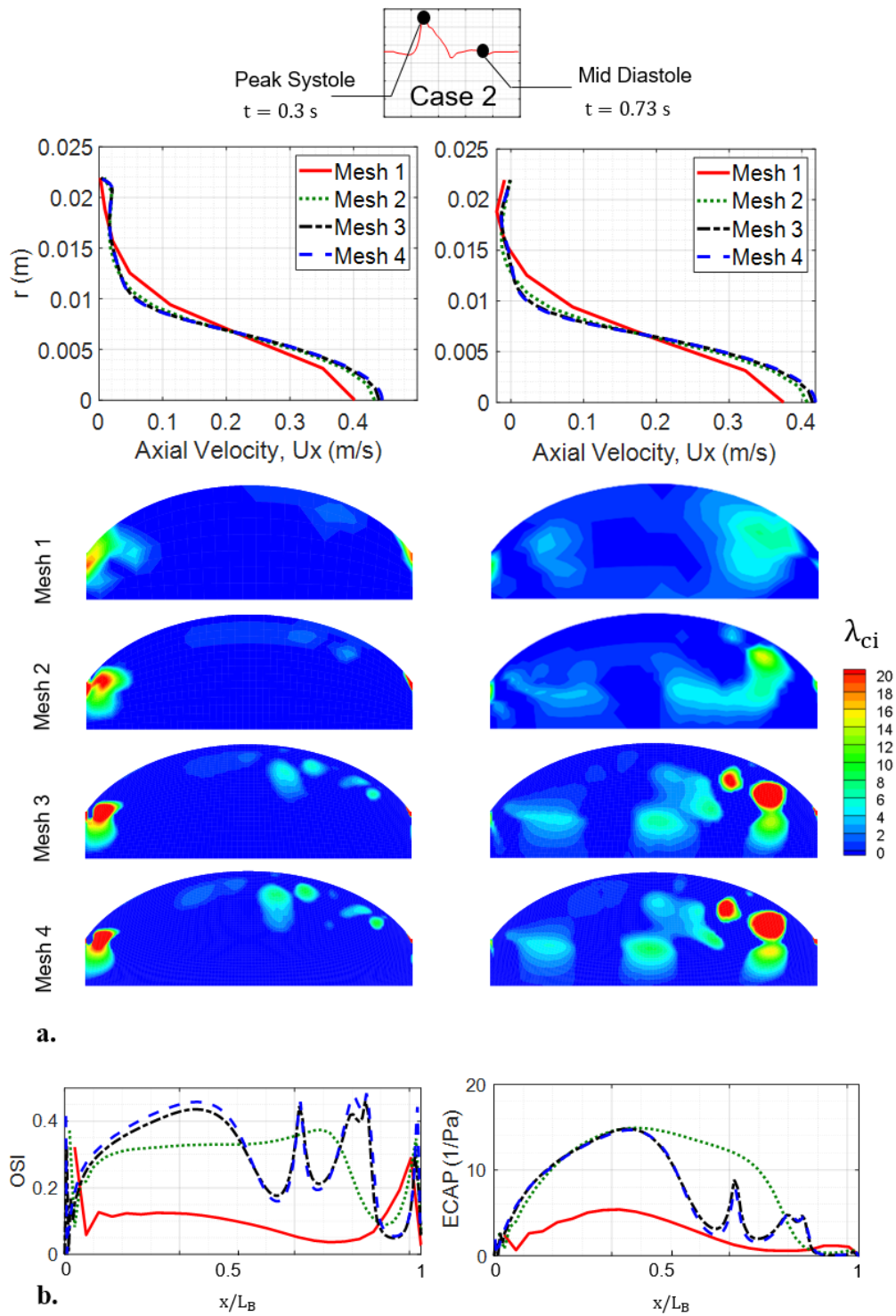
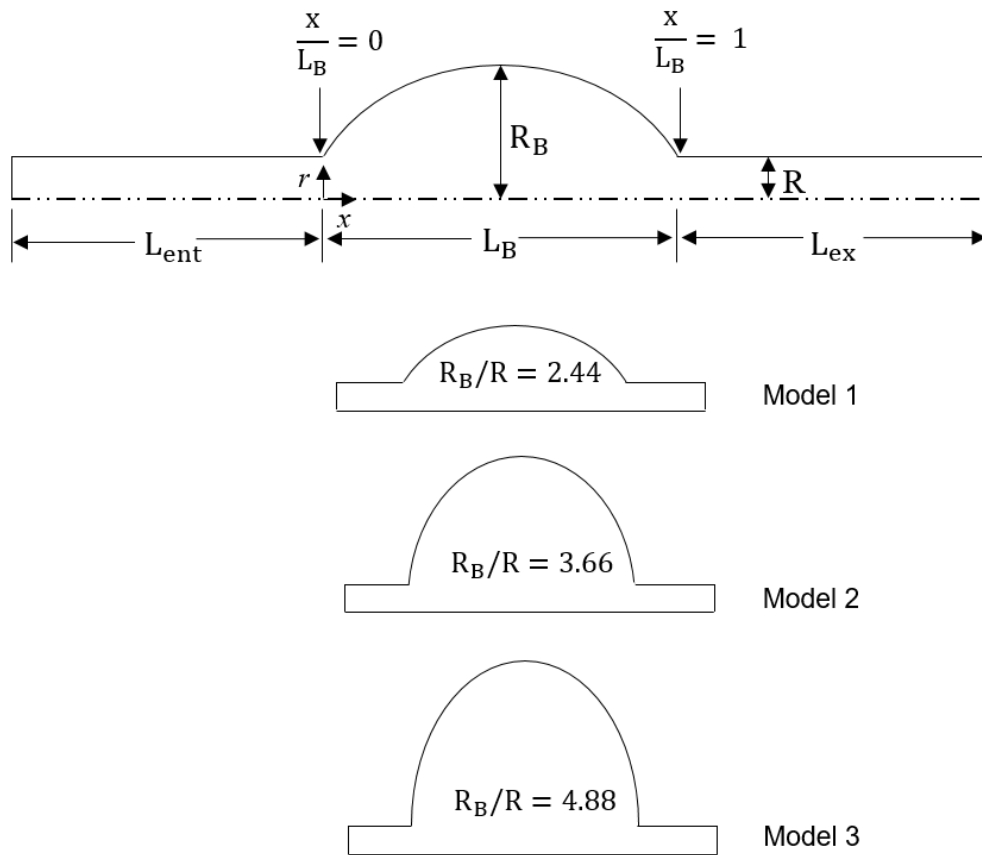


Figure 3.7. a. Axial velocity profiles obtained with four different meshes at $x/L_B = 0.5$, and swirling strength contours, b. OSI and ECAP distributions of four meshes for Case 2

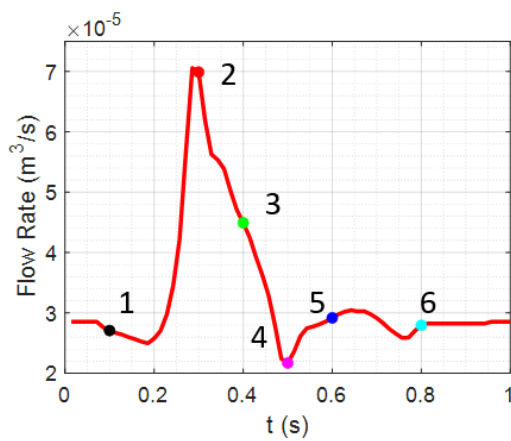
3.1.3 Correlation between vortex identification methods and wall shear stress parameters study

The idealized abdominal aortic aneurysm (AAA) models used in this study are given in Fig. 3.8a. Geometries are two-dimensional, axisymmetric, and created based on those used in Stamatopoulos et. al's study (2010). Inlet and exit parts are straight and cylindrical, while the aneurysm bulge is elliptical with a major radius of 0.034 m. The lengths of the entrance part, $L_{ent} = 935$ mm, the bulge, $L_B = 62$ mm, and the exit part, $L_{ex} = 206$ mm, as well as the artery radius, $R = 9$ mm, are the same for all models, while the bulge radius, R_B , varies. As shown in Fig. 3.8a, three different bulge radius to aorta radius ratios, $R_B/R = 2.44, 3.66$ and 4.88 , which are referred as Model 1, 2 and 3, respectively, are considered. The vessel and bulge dimensions are consistent with realistic abdominal arteries and aneurysms (Les et al., 2010; Brewster et al., 2003).

Unsteady plug flow is specified at the inlet, and through a number of preliminary runs, the entrance length is selected as 50 times the vessel diameter, which is sufficiently long to have fully developed condition at the bulge inlet (Madhavan and Kemmerling, 2018). A constant reference pressure of 0 Pa is specified at the outlet, which is a frequently utilized approach in literature for hemodynamic studies (Qiu et al., 2018; Reza and Arzani, 2019). Through the preliminary runs, it is made sure that the length of the exit part is long enough such that the disturbance created by the bulge dies out before the flow reaches the outlet, enabling the use of constant pressure outlet condition. Wall boundaries are taken as rigid with no-slip boundary condition applied. Excluding the compliance effect with utilizing the walls as rigid is quite common (Arzani et al.; Les et al., 2010; Kelsey et al., 2016; Biasetti et al., 2011; Biasetti et al., 2012; Finol and Amon, 2001).



a.



b.

Figure 3.8. a. 2D axisymmetric flow domains for aneurysm models with three different bulge radii, b. Physiological inlet flow rate waveform (Finol and Amon, 2001)

The physiological inlet waveform (Finol and Amon, 2001) used in the simulations is given in Fig.3.8b. It has a period of $T = 1$ s, yielding a Womersley number of $\alpha = 0.5D\sqrt{\omega/\nu} = 12.14$, where D is the artery diameter, ω is the frequency and equals to $2\pi/T$, and ν is the kinematic viscosity. The mean Reynolds number is $Re_m = U_m D/\nu = 670$, where $U_m = 0.13$ m/s is the time averaged velocity over one period. The cardiac cycle is divided into six phases, which are early/mid/late systole and diastole, as shown in Table 3.2. Representative time instances for each phase are numbered from 1 to 6 in Fig. 3.8b, and the results corresponding to them will be given in the Results section.

In general, blood has non-Newtonian characteristics where the viscosity decreases with increased shear rate. However, at shear rates higher than 100 s^{-1} , blood shows Newtonian characteristics, and for large arteries, such as the one used in this study, it can be assumed as Newtonian with a kinematic viscosity of $3.45 \times 10^{-6} \text{ m}^2/\text{s}$, and density of 1000 kg/m^3 .

Numerical simulations are conducted by using the open source software OpenFOAM (openfoam.org). Flow is considered to be laminar (Scotti et al., 2008) due to the peak Reynolds number, $Re_{\text{peak}} = 1500$, not exceeding the threshold value (2000–2300) for transition to turbulence in pipe flow. The governing equations are discretized using second order implicit discretization in time and second order central discretization in space. Among the incompressible flow solvers available in OpenFOAM, pimpleFoam is preferred because it enables automatic control of the time step size based on a user selected maximum Courant number (C_{max}). To select the necessary C_{max} that provides accurate solutions, four different values, 0.25, 0.5, 1, 2, and 4, are tested, with higher values failing to provide stable solutions. All tested C_{max} values resulted in practically identical solutions and C_{max} is set to 1 in the actual simulations. Maximum number of iterations performed at each time step is taken as 30, and the solutions are considered to be converged when residuals for axial velocity component and pressure are less than 10^{-4} . To ensure that the time periodic state is reached, calculations are repeated for six cardiac cycles. To select a

suitable mesh, a mesh independence study is performed using four structured meshes created for Model 1, as shown in Fig. 3.9. Figure 3.10 shows axial velocity profiles at the mid-plane of the aneurysm and swirling strength, λ_{ci} contours obtained by using these meshes at the peak systole and early diastole. As seen, the axial velocity profiles are identical and swirling strength contours are very similar for the 3rd and the 4th meshes, and therefore Mesh 3 is evaluated to be suitable and used to perform the simulations in the present study.

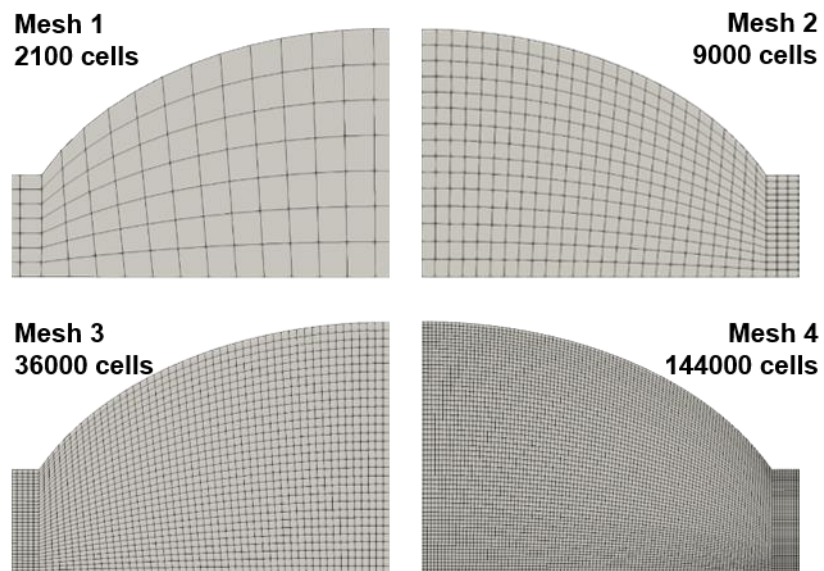


Figure 3.9. Four meshes used for the mesh independence check

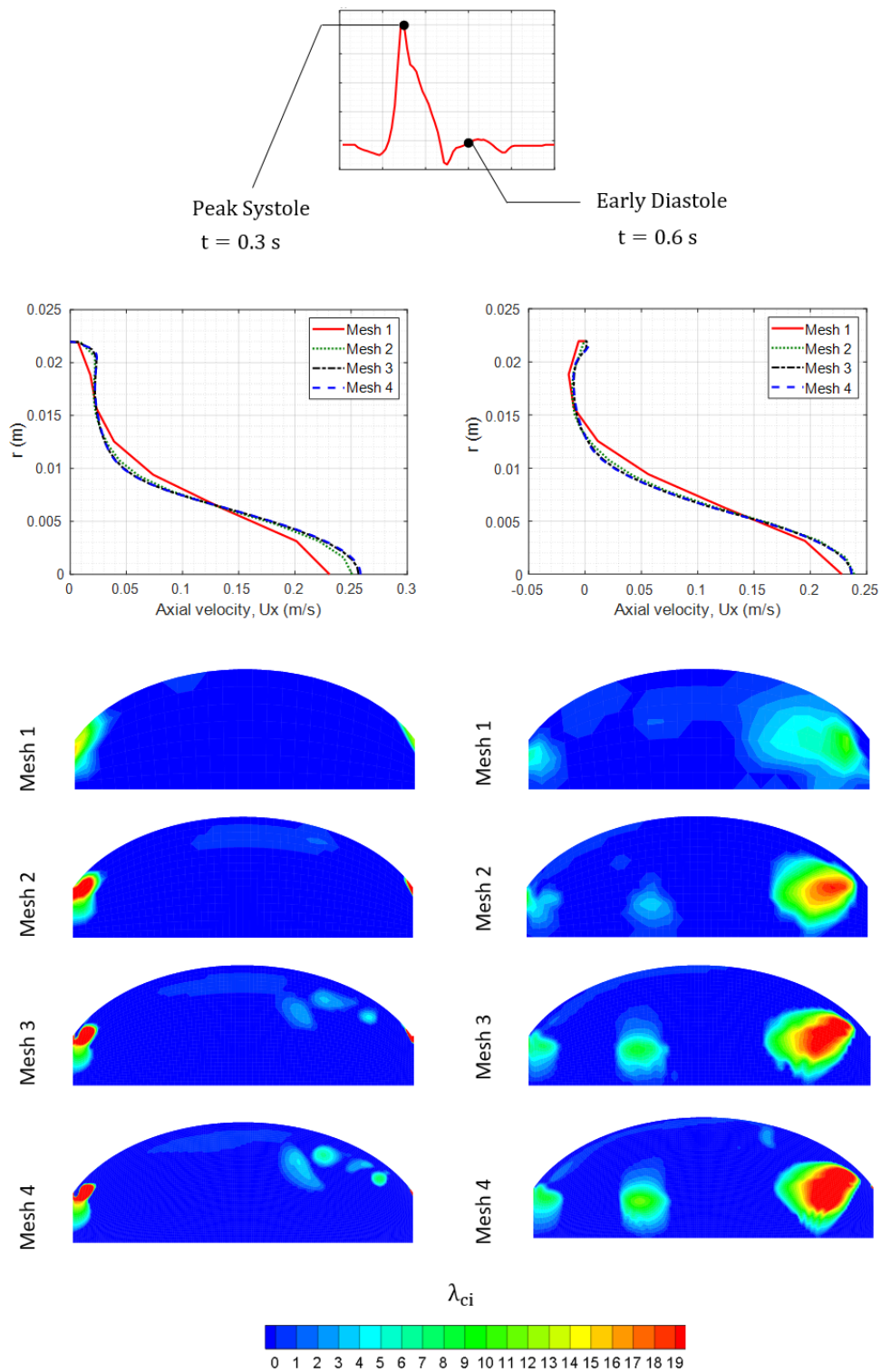


Figure 3.10. Axial velocity profiles obtained with four different meshes $x/L_B = 0.5$, and swirling strength contours

3.2 WSS Parameters and Vortex Identification Techniques

In literature, researchers utilize several physical phenomena to predict aneurysm development, thrombosis formation and rupture. Generally, wall shear stress (WSS) distribution and different WSS descriptors are used for this purpose. TAWSS descriptor evaluates the total shear stress exerted on the wall throughout a cardiac cycle and OSI highlights zones where WSS shows directional changes over the cardiac cycle (Pinto and Campos, 2016). Mathematical definitions of these descriptors are given below.

$$TAWSS = \frac{1}{T} \int_0^T |\tau_w| dt \quad (3.5)$$

$$OSI = 0.5 \left(1 - \frac{\left| \frac{1}{T} \int_0^T \tau_w dt \right|}{\frac{1}{T} \int_0^T |\tau_w| dt} \right) \quad (3.6)$$

$$ECAP = \frac{OSI}{TAWSS} \quad (3.7)$$

$$RRT = \frac{1}{(1 - 2 \cdot OSI) \cdot TAWSS} \quad (3.8)$$

where T and τ_w are the cardiac cycle period and the wall shear stress, respectively.

In literature, different vortex identification methods are used to quantify vortex dominant flows such as vortex rings. The most well-known methods include Q-criterion, Δ -criterion, λ_2 -criterion and λ_{ci} -criterion (Epps, 2017), which are briefly discussed here. Δ -criterion and λ_{ci} -criterion are called as velocity gradient based vortex identification criteria, which use discriminant of characteristic equation and imaginary part of the complex eigenvalue, respectively, while λ_2 -criterion utilizes local pressure minimum to define a vortex. On the other hand, Q-criterion compares the rotation rate with the strain rate (Epps, 2017). For 2D axisymmetric flows, Q-criterion, λ_{ci} -criterion and λ_2 -criterion can be written in the following form (Chen et al., 2015)

$$Q = -\frac{\partial u_r}{\partial x} \frac{\partial u_x}{\partial r} - \frac{1}{2} \left(\frac{\partial u_r}{\partial r} \right)^2 - \frac{1}{2} \left(\frac{\partial u_x}{\partial x} \right)^2 > 0 \quad (3.9)$$

$$\lambda_{ci} = \frac{1}{2} \sqrt{-4 \frac{\partial u_r}{\partial x} \frac{\partial u_x}{\partial r} - \left(\frac{\partial u_x}{\partial x} - \frac{\partial u_r}{\partial r} \right)^2} > 0 \quad (3.10)$$

$$\lambda_2 = \frac{\partial u_r}{\partial x} \frac{\partial u_x}{\partial r} + \frac{1}{2} \left[\left(\frac{\partial u_x}{\partial x} \right)^2 + \left(\frac{\partial u_r}{\partial r} \right)^2 \right. \\ \left. + \left| \frac{\partial u_x}{\partial x} + \frac{\partial u_r}{\partial r} \right| \sqrt{\left(\frac{\partial u_x}{\partial x} - \frac{\partial u_r}{\partial r} \right)^2 + \left(\frac{\partial u_r}{\partial x} + \frac{\partial u_x}{\partial r} \right)^2} \right] < 0 \quad (3.11)$$

Vortex structures are studied extensively in fluid mechanics because in many cases they provide important insight about the flow field. Inside the aneurysm sac, there is a vortex ring that evolves throughout the cardiac cycle. Temporal evolution of vortex structure through cardiac cycle for Model 1, 2 and 3 are presented in Appendix B. Detailed derivation of those vortex identification methods is available in Appendix C.

3.3 Validation of Numerical Model and 2D/3D Model Comparison

Stamatopoulos et al. (2010) have performed an experimental and numerical study in axisymmetric bulges similar to the ones used in the current study with a steady inlet flow. In Fig. 3.11a, axial velocity profiles obtained by Stamatopoulos et al. (2010) are compared with those obtained in the current study with a steady inlet flow. The match in the profiles is considered to be satisfactory. Ohtaroglu (2020) performed experiments with physiological, unsteady inlets using Stamatopoulos et al.'s (2010) geometry. Figure 3.11c compares the streamlines obtained in those experiments with the current simulation results at four different time instants of the physiological

cycle. Progression of focus points in streamlines which are the indication of vortex core movement shows good agreement. Considering both the spatial and the temporal evolution during the cycle, the model predictions are considered to be satisfactory. In addition, simulations are performed to ensure the validity of 2D axisymmetric simplification by comparing results with those of 3D simulations. This simplification aims to decrease the computation time and is justified by performing a sample 3D simulation to see whether there are any 3D effects altering the overall flow structure inside the aneurysm bulge. Considering the velocity profiles plotted at the mid plane of the bulge as demonstrated in Fig. 3.11b, 2D axisymmetric and 3D results turn out to be almost identical.

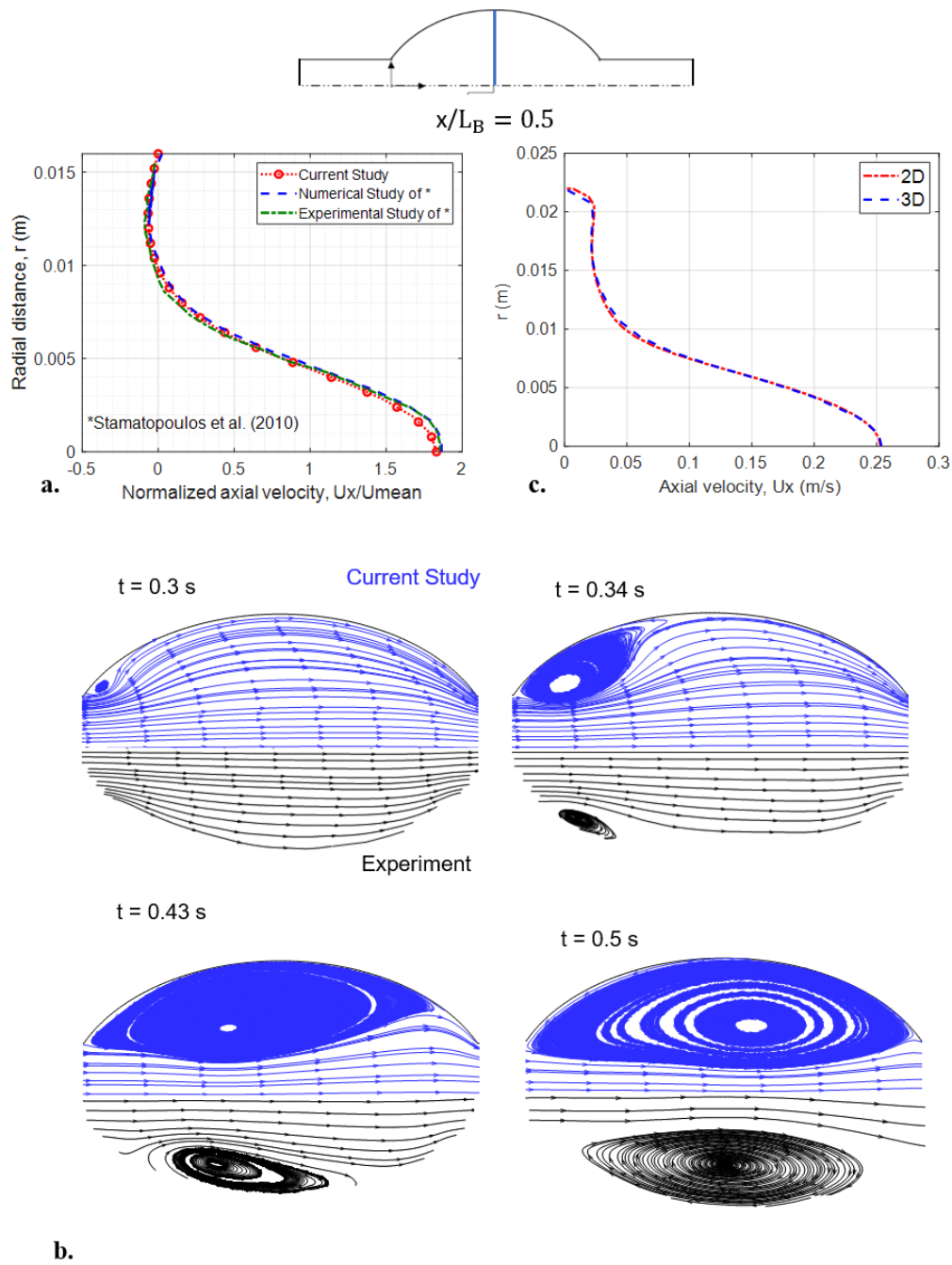


Figure 3.11. a. Comparison of the normalized axial velocity profile with results of Stamatopoulos et al. (2010) for a steady inlet velocity, b. Comparison of the streamline patterns of different time instants with results of Ohtaroglu (2020), c. Comparison of the axial velocity profiles of 2D axisymmetric and 3D geometries at $x/L_B = 0.5$ at $t = 0.3$ sec

CHAPTER 4

EFFECT OF INLET VELOCITY PROFILE AND ENTRANCE LENGTH ON ABDOMINAL AORTIC ANEURYSM HEMODYNAMICS

Simulating the exact hemodynamics throughout abdominal aortic aneurysms (AAA) depends on the assumptions done during the numerical solution. Transient effects of physiological flow are well described by *Womersley* profile, though its application can be difficult due to the Bessel functions and imaginary numbers that it contains. Conversely, in literature, studies utilizing *Plug* or *Parabolic* profiles as inlet boundary condition generally require large entrance lengths to obtain *Womersley* profile characteristics. In the current chapter, the differences arising between those idealized boundary conditions, *Womersley*, *Parabolic* and *Plug*, with different entrance lengths, $L_{ent} = D, 3D$ and $11D$, are examined by comparing the results with a Base condition, which is a solution obtained with ensured fully-developed flow before entering the aneurysm sac at two mean Reynolds numbers, $Re_m = 340$ and 1160 .

4.1 Results

In Figure 4.1, time-averaged axial velocity profiles obtained with *Womersley*, *Parabolic* and *Plug* inlet velocity profiles at different entrance lengths for mean Reynolds number, $Re_m = 340$, are presented and compared with the Base condition. The profiles are plotted at proximal, mid, distal and exit sections of the models, where $x/L_B = 0.25, 0.5, 0.75$ and 1 . At each section, results obtained with different inlet conditions at different entrance lengths, $L_{ent} = D, 3D$, and $11D$, are plotted. For each sections and entrance lengths, the time-averaged axial velocity profiles for

Womersley is the same with the Base case. For *Parabolic* and *Plug*, the general pattern of time-averaged axial velocity profiles are also very close to *Womersley* and Base condition for $L_{ent} = 11D$. However, for $L_{ent} = D$ and $3D$, the shape of time-averaged velocity profiles and maximum velocity values that they obtained are very different than the Base condition. In addition, the backflow region, which is an important characteristics of the aneurysm hemodynamics, is obtained inside the bulge by the *Womersley* and the Base case for all L_{ent} values. Especially for $L_{ent} = D$, *Plug* and *Parabolic* fail to have an accurate backflow region at those sections.

Figure 4.2 shows the time-averaged axial velocity profiles for $Re_m = 1160$ in the same orientation with the Figure 4.1. For this waveform, similar with the previous case, time-averaged axial velocity profiles for *Womersley* are nearly identical with the Base condition for all entrance lengths. Different from the results for $Re_m = 340$, *Parabolic* also obtain nearly the same velocity profile with *Womersley* and the Base condition for each sections and entrance lengths, even for $L_{ent} = D$, for $Re_m = 1160$. On the other hand, *Plug* fails to obtain a similar maximum velocity and the backflow region with the Base case for both $L_{ent} = D$ and $3D$. For $L_{ent} = 11D$, although the maximum velocity value is different, it can capture backflow region. In addition, time-averaged axial velocity profiles for *Womersley* and *Parabolic* demonstrate a parabolic pattern, while *Plug* has a velocity profile with a flat central part, implying that even $L_{ent} = 11D$ is not sufficient for *Plug* profile to achieve fully developed condition for $Re_m = 1160$. For $Re_m = 340$, general pattern obtained by *Plug* is very similar with the *Womersley* and Base condition, while for $Re_m = 1160$, velocity profiles of *Parabolic* are nearly the same with them, even with $L_{ent} = D$.

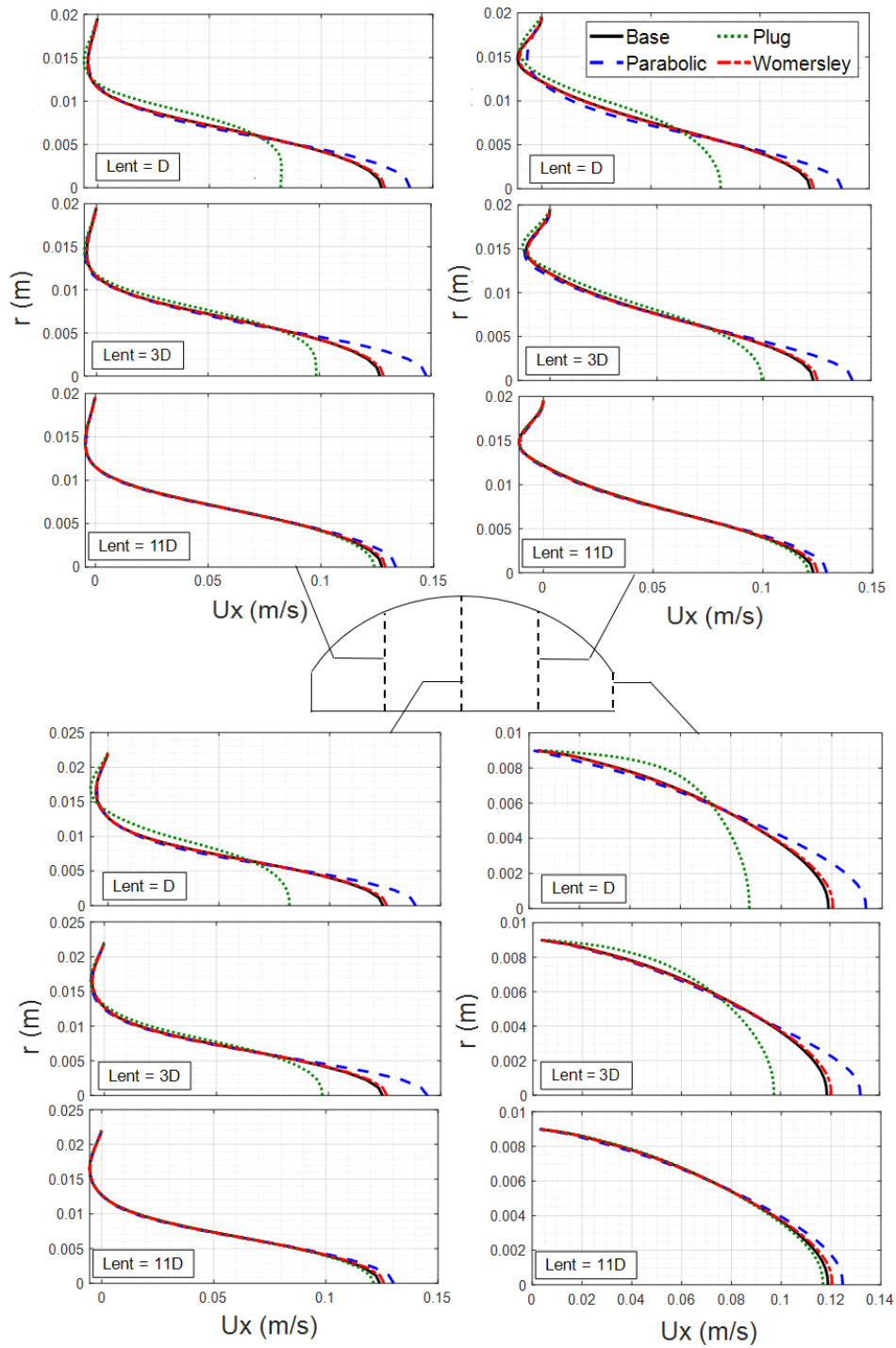


Figure 4.1. Comparison of time-averaged axial velocity profiles obtained by different inlet velocity profiles and entrance lengths for $Re_m = 340$

In Figure 4.3 and 4.4, oscillatory shear index (OSI) and endothelial cell activation potential (ECAP) distributions obtained with *Womersley*, *Parabolic* and *Plug* inlet velocity profiles at different entrance lengths throughout the aneurysm sac are plotted and compared with the Base case. For $Re_m = 340$ and $L_{ent} = 11D$, OSI and ECAP distributions for all inlet velocity profiles are the same with Base condition. For $L_{ent} = D$ and $3D$, *Womersley* gives the same OSI and ECAP distributions with Base condition. Although the maximum velocity values obtained by *Parabolic* at each section inside the aneurysm are very different for $L_{ent} = 3D$, OSI and ECAP distributions of *Parabolic* are very similar with Base condition because their backflow regions are similar, which affects the WSS parameters considerably. Similarly, for $L_{ent} = D$, in which backflow region of *Parabolic* and *Plug* are completely different than Base condition, WSS parameters are also very different. For $Re_m = 1160$, *Parabolic* and *Womersley* obtain nearly the same OSI and ECAP distributions with the Base case for $L_{ent} = 3D$ and $11D$. Although their results are very similar with each other for $L_{ent} = D$, a deviation from Base condition is observed. *Plug* fails to provide an accurate OSI and ECAP distribution for $Re_m = 1160$, even with a longer entrance length, $L_{ent} = 11D$.

In Figure 4.5, for $Re_m = 1160$, instantaneous wall shear stress distributions and contours of swirl strength, λ_{ci} , are presented for late systole and early diastole phases, $t = 0.49$ and 0.73 sec, through aneurysm bulge. Top part of the figure shows the results for $L_{ent} = 3D$, while the mid part is for $L_{ent} = 11D$. For the top and mid parts, contours of swirl strength for *Womersley*, *Parabolic* and *Plug* inlet velocity profiles are located, under the instantaneous WSS distributions, from top to bottom, respectively. Contours of λ_{ci} and streamline patterns of Base condition are located at the bottom part of the figure to compare the results obtained with idealized inlet velocity profiles. From the contours of λ_{ci} for the Base case, at the late systole, $t = 0.49$ sec, the primary vortex structure is translated to distal end, and a new vortex is originated from the primary vortex structure, which might be labeled as second primary vortex structure.

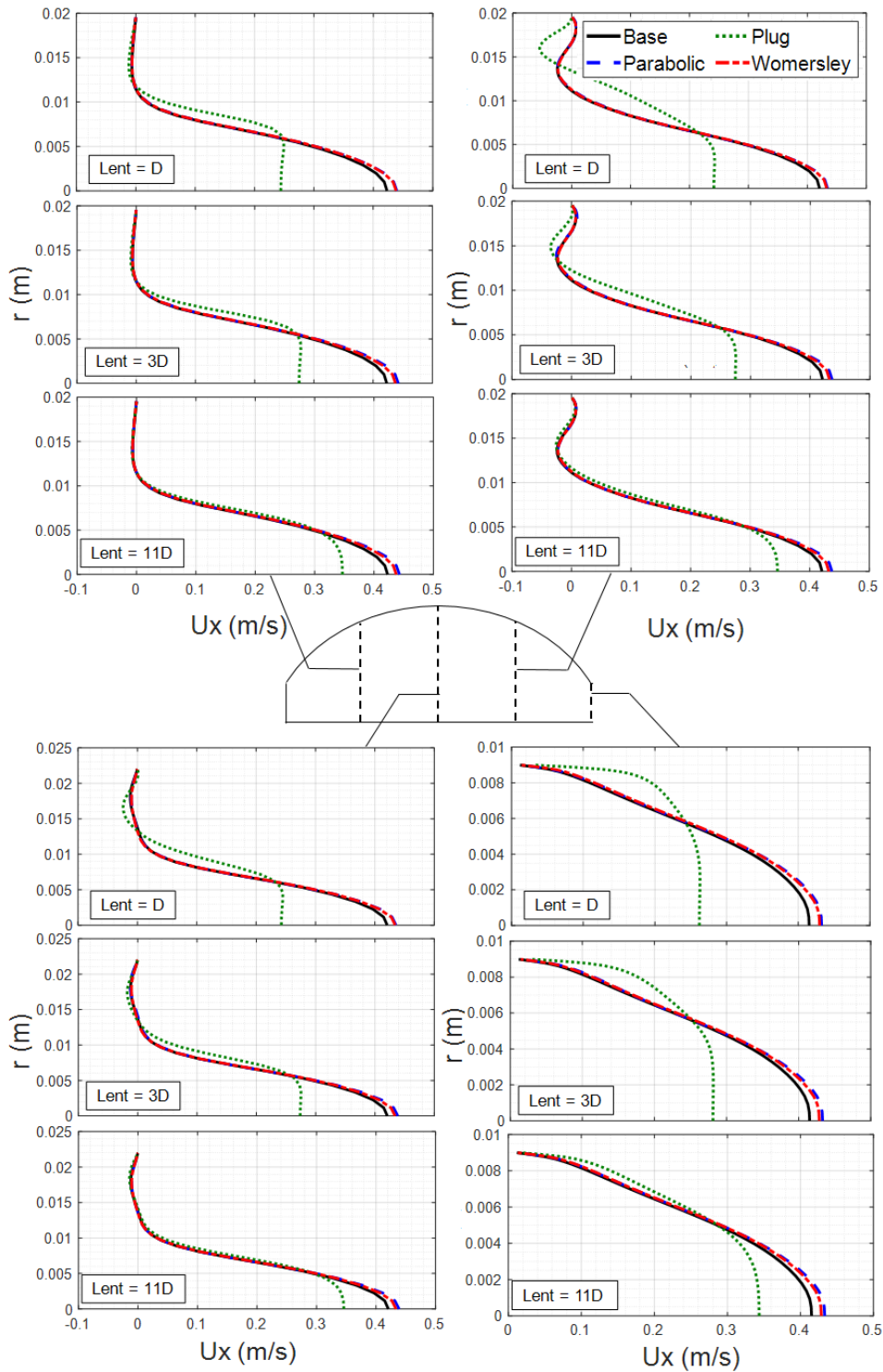


Figure 4.2. Comparison of time-averaged axial velocity profiles obtained by different inlet velocity profiles and entrance lengths for $Re_m = 1160$

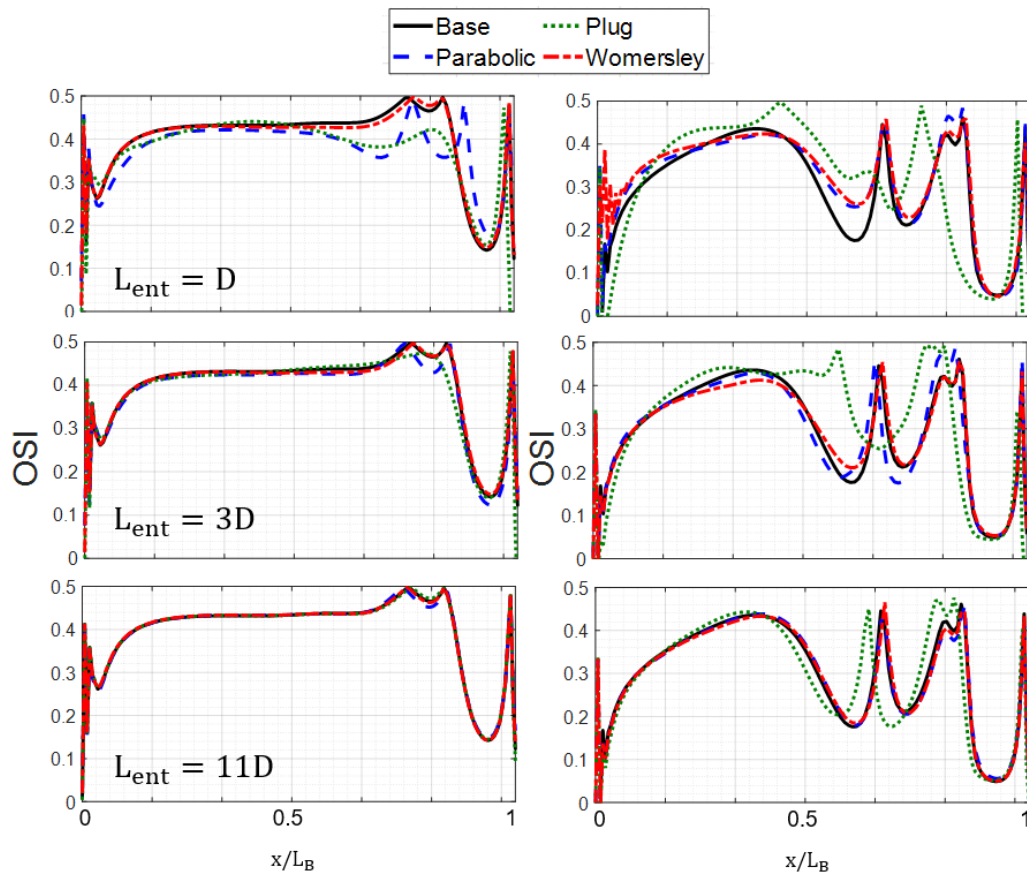


Figure 4.3. Comparison of OSI distributions obtained by different inlet velocity profiles and entrance lengths for $Re_m = 340$ and 1160 , from left to right, respectively

The primary and second primary vortex structures are enclosed by a closed streamline pattern, but they have different vortex cores. At the early diastole, $t = 0.73$ sec, the primary vortex structure still stays the distal end of the bulge, but its intensity decreases due to viscous diffusion. An additional secondary vortex is generated and located between those two vortex cores, which is very near to the wall and with a smaller swirl strength magnitude than the primary vortex.

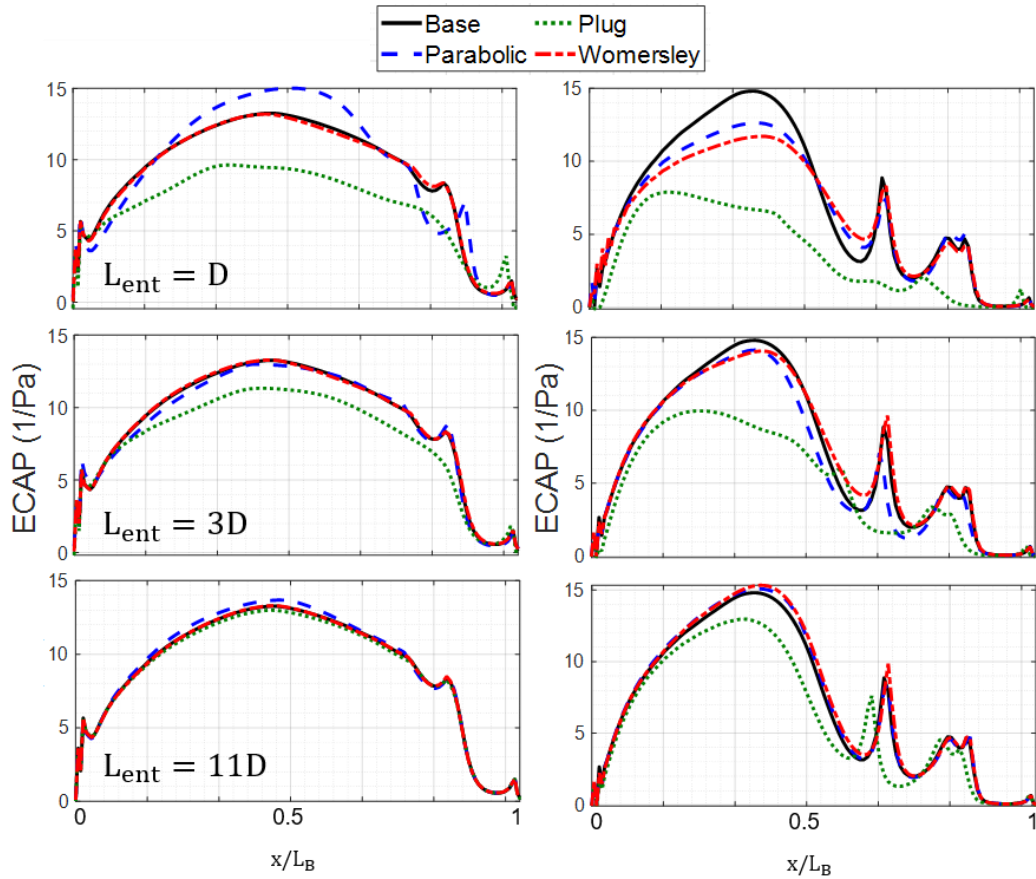


Figure 4.4. Comparison of ECAP distributions obtained by different inlet velocity profiles and entrance lengths for $Re_m = 340$ and 1160 , from left to right, respectively

At each time instant, the contours of swirl strength and instantaneous WSS distributions obtained by *Womersley* and *Parabolic* inlet velocity profiles with $L_{ent} = 11D$ are identical with the Base condition. The vortical structures obtained by *Plug* are also similar in terms of location of cores of primary vortex structure and general swirl strength pattern, but the intensity of the contours is significantly different especially in late systolic and early diastolic phases, for $t = 0.49$ and 0.73 sec. Also, WSS distributions obtained by *Plug* case are different than the others at the specified time instants, which is in accordance with swirl strength patterns. For $L_{ent} = 3D$, *Womersley* obtains nearly the same λ_{ci} patterns and WSS distributions with the Base case. Although WSS patterns of *Parabolic* are also the same with them,

there is a negligible discrepancy of intensity of swirl strength contours for $t = 0.49$ and 0.73 sec. On the other hand, *Plug* obtains completely different results with $L_{ent} = 3D$, which is convenient with the differences observed in time-averaged axial velocity profiles and OSI and ECAP distributions for that inlet condition.

WSS distributions at different time instants have a correlation with vortex structure movement and swirl strength magnitude, which is also observed by Biasetti et al. (2011). As can be seen in Figure 4.5, there is a WSS peak around the primary vortex structure which is near to the wall at each time instants. With increasing the intensity and magnitude of λ_{ci} of the near-wall vortex structure, the magnitude of WSS peak also increases. This phenomenon can also be observed in the WSS distribution and λ_{ci} contour of *Plug* at $t = 0.49$ sec with $L_{ent} = 3D$. For that time instant, primary vortex structure with a large $|\lambda_{ci}|$ of the *Plug* case is not located in proximity of the wall at the distal area, and its WSS distribution shows a very small peak at that region. Moreover, at $t = 0.73$ sec, primary vortex structure of *Plug* is not dissipated as much as Base condition, and it shows a high swirl strength intensity and WSS magnitude in the distal area, for $L_{ent} = 3D$. Despite the correlation between the primary vortex structure and WSS magnitude, second primary vortex structure has no effect on WSS distribution due to large distance between the vortex and aneurysm wall. However, at $t = 0.73$ sec, the secondary vortex structure is observed. It has an effect on WSS distribution since it is located in close proximity to the wall. Because the swirling strength magnitude is smaller for the secondary vortex structure, its effect on WSS distribution is also small.

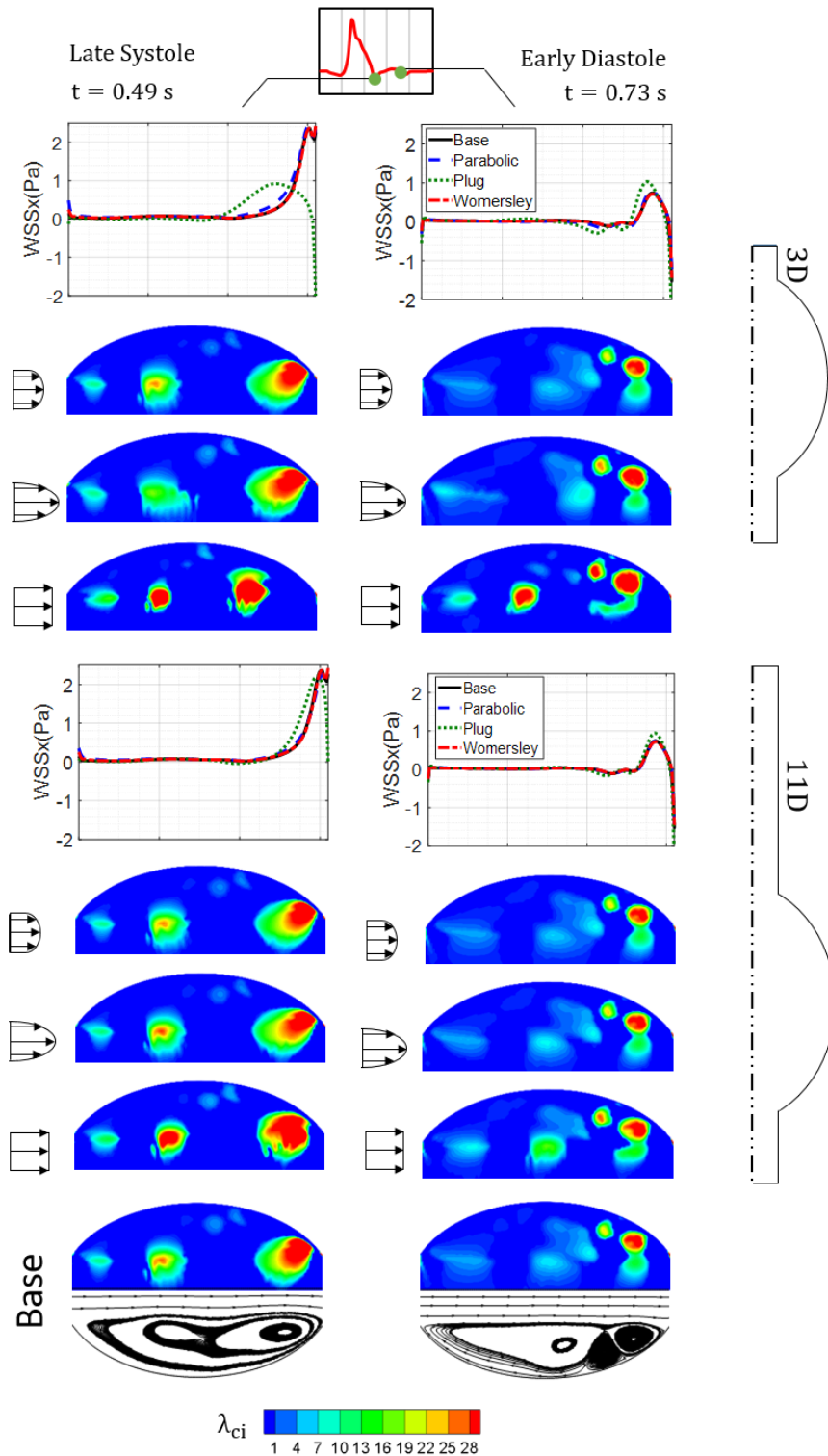


Figure 4.5. Comparison of instantaneous WSS distributions, contours of swirling strength and streamline patterns for $Re_m = 1160$

4.2 Discussion

In the current study, the effect of inlet velocity profiles, which are *Womersley*, *Parabolic* and *Plug*, on predicting the hemodynamics by using different entrance lengths is discussed at two different Re_m using the same physiologic flow waveform pattern. Results are compared with the Base condition, which has a very long entrance length with a uniform flow at the inlet to ensure the flow entering the aneurysm sac is fully developed. According to the comparisons of time-averaged axial velocity profiles at different sections inside the sac, OSI and ECAP distributions, instantaneous WSS distributions and swirl strength contours, *Womersley* and *Parabolic* profiles give the same results with Base condition, even with a very small entrance length, $L_{ent} = 3D$. However, for $Re_m = 1160$, even *Womersley* profile could not achieve the same OSI and ECAP distributions with the Base case with $L_{ent} = D$. With increasing Reynolds number, entrance length requirement of *Womersley* profile becomes nearly the same with *Parabolic* profile. Therefore, especially for high mean Reynolds numbers, utilization of *Womersley* profile might not be necessary. Therefore, rather than applying complex *Womersley* formulation, utilization of *Parabolic* profile for high mean Reynolds numbers with an entrance length at least $L_{ent} = 3D$ might be appropriate. On the other hand, *Plug* profile cannot obtain similar results with Base condition even $L_{ent} = 11D$ for high mean Reynolds number, $Re_m = 1160$, but for $Re_m = 340$, using an entrance length $L_{ent} = 11D$ with *Plug* profile can yield the same results with Base condition.

CHAPTER 5

EFFECT OF INFRARENAL FLOW WAVEFORM PATTERN ON RHEOLOGY MODEL SELECTION AND ABDOMINAL AORTIC ANEURYSM HEMODYNAMICS

Although blood behaves as a Newtonian fluid for high shear rates ($\dot{\gamma} > 100 \text{ s}^{-1}$), stagnant and low velocity recirculation regions with very small shear rates present inside the aneurysm sac due to the separation of bulk flow at diastolic phase. Also, infrarenal flow waveform pattern, especially peak systolic and diastolic flow rates, demonstrates significant differences from patient to patient, which might affect the $\dot{\gamma}$ distribution through the aneurysm sac. To investigate the effect of infrarenal flow waveform on rheology model selection, three waveform patterns, Base, Case 1 and 2, having different peak systolic and diastolic flow rate values are tested. Wall shear stress (WSS) parameters such as time-averaged wall shear stress (TAWSS), oscillatory shear index (OSI), endothelial cell activation potential (ECAP), relative residence time (RRT) and swirling strength (λ_{ci}) contours are obtained by viscous shear thinning models such as Carreau, Carreau-Yasuda, Cross, Casson, Power, Quemada, Modified and Simplified Cross, and viscoelastic Oldroyd-B are compared with Newtonian model.

5.1 Results

Temporal evolution of vortex structures for all Base, Case 1 and 2 waveform patterns, obtained by using Carreau model, are presented in Figures 5.1, 5.2 and 5.3, respectively. For all waveforms, a primary vortex is generated due to acceleration of bulk flow during early systole, and it separates from the inlet of the bulge at $t = 0.3$

sec, which is the peak systole, and transported to downstream by means of advection. Indeed, the acceleration and advection of bulk flow are the primary phenomena that differ with the characteristics of the flow waveform. For the Base waveform, acceleration is small compared to Case 1, resulting only a weaker primary vortex with small $|\lambda_{ci}|$. Also, advective effects are not dominant due to low bulk flow rate. Therefore, primary vortex dissipates before it reaches the central part of the bulge due to diffusive effects. The largest acceleration is obtained by the Case 1, and during early systole, larger acceleration generates stronger vortex with large $|\lambda_{ci}|$ compared to Base and Case 2. This primary vortex maintains itself as a strong identity, with a very small dissipation, until the end of the cardiac cycle. Because the mean flow rate of Case 1 is larger than Base, throughout the cardiac cycle, the primary vortex is transported to downstream by means of advection and it reaches the distal region at $t = 1$ sec. On the other hand, advection is more dominant for Case 2 due to its larger mean flow rate. Therefore, transportation of vortex to distal region is completed until the end of the systolic phase, $t = 0.5$ sec. Throughout the diastolic phase, vortex is placed at the distal zone and it is dissipated by means of viscous effects until the end of the cycle, while primary vortex for Case 1 case maintains its identity. On the other hand, viscous diffusion is more dominant in Base waveform pattern because low acceleration generates a weak primary vortex with a low $|\lambda_{ci}|$, and advective effects are not sufficient to transport it even until the central area due to small mean flow rate.

Figure 5.4 shows contours of time-averaged swirling strength, $\overline{\lambda_{ci}}$, and streamlines together with variations of WSS parameters for three waveform patterns, Base, Case 1 and 2. According to $\overline{\lambda_{ci}}$ contours and streamlines, only primary vortex pattern, located at the proximal region of the bulge, is generated for the Base flow waveform. For the Case 1 and 2, second primary and secondary vortices are also generated. For the Case 1 and 2, primary vortex is located at the distal region with a larger magnitude of $\overline{\lambda_{ci}}$ compared to the Base case. For Case 1, second primary and secondary vortices are located at the proximal and central regions, respectively.

However, for Case 2, they are both located at the distal zone, with vortices present at the proximal part, which is exact opposite of the Base case.

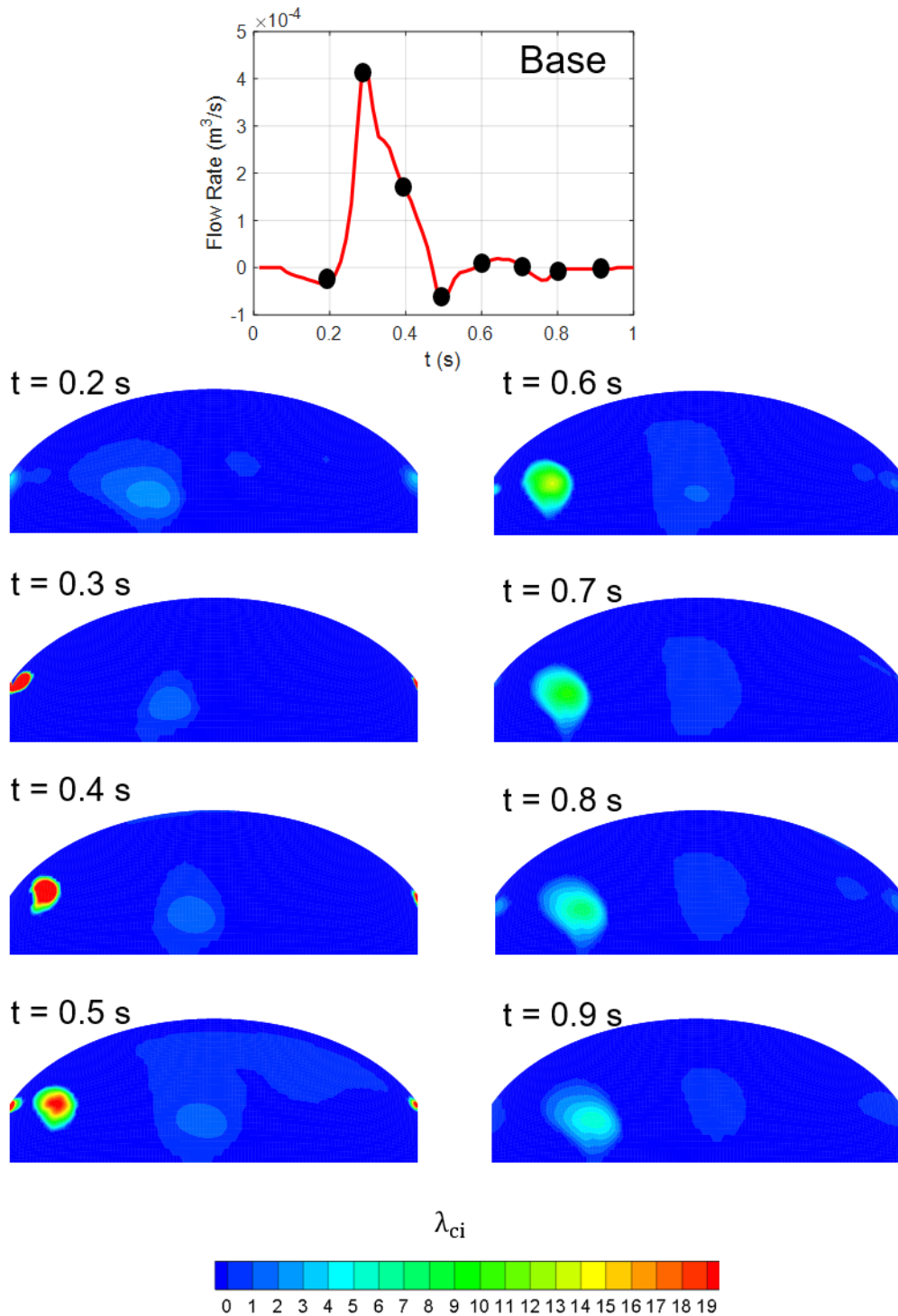


Figure 5.1. Comparison of swirl strength contours for Base

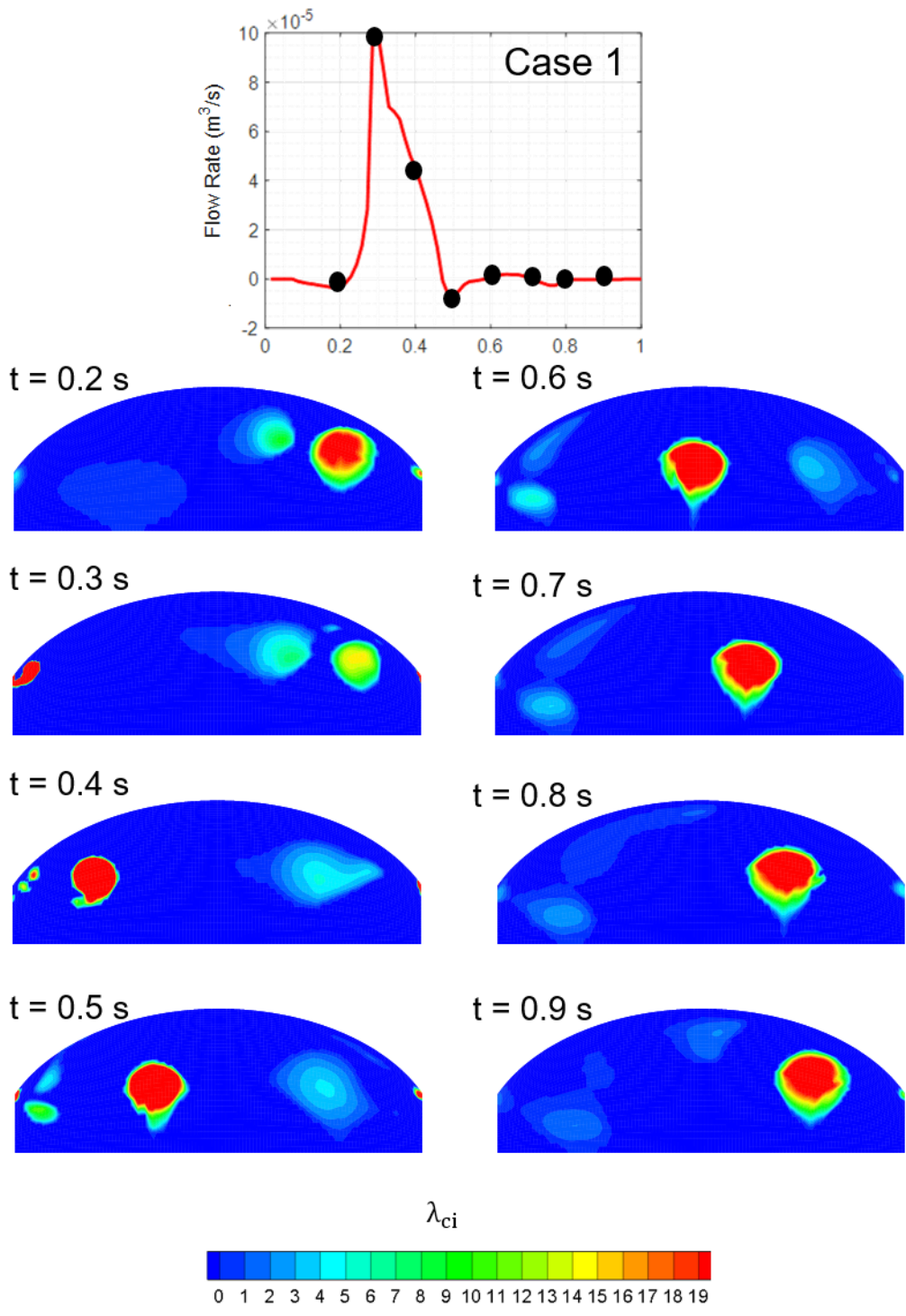


Figure 5.2. Comparison of swirl strength contours for Case 1

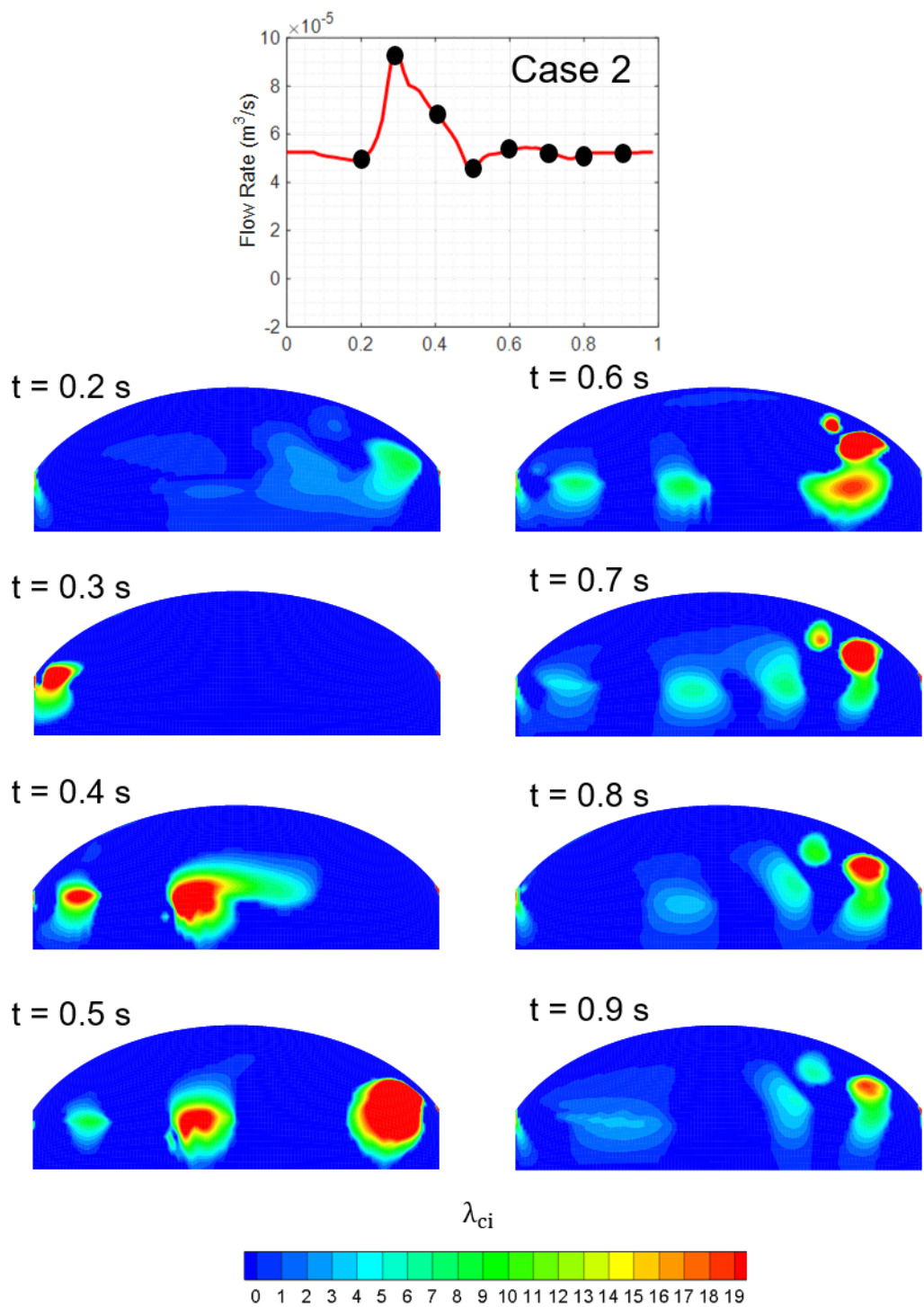


Figure 5.3. Comparison of swirl strength contours for Case 2

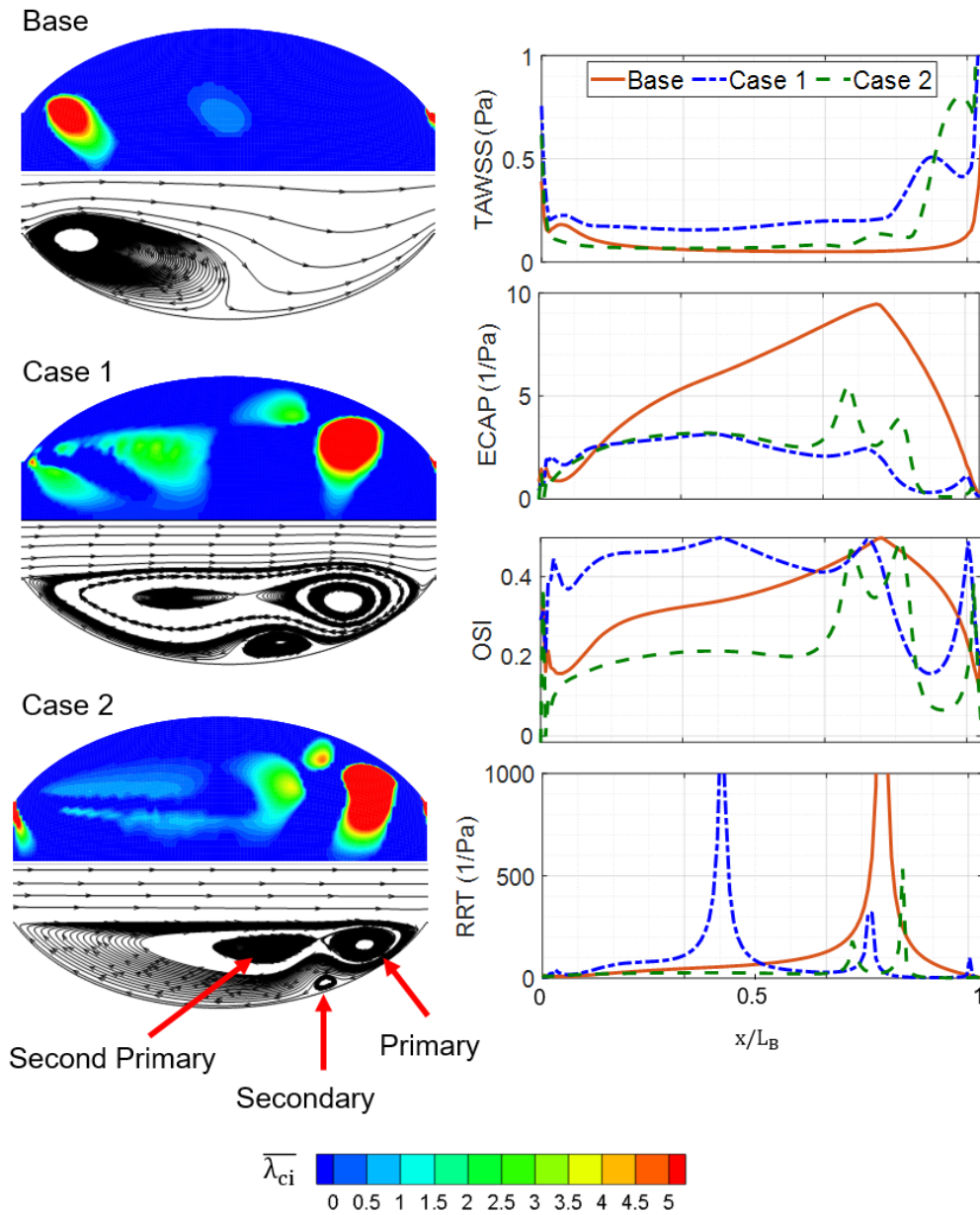


Figure 5.4. Comparison of time-averaged swirl strength contours, streamline patterns and the variation of WSS measures on the aneurysm wall, for the waveform patterns, Base, Case 1 and 2

Behavior of vortex structures significantly affects the WSS parameters, as can be observed from Fig. 5.4. TAWSS is very high around the vortices, especially near-wall large $|\overline{\lambda_{ci}}|$ zones, where OSI, ECAP and RRT are low. The magnitude of ECAP and RRT reaches zero at the regions where the primary vortex is located, having high

$|\overline{\lambda_{ci}}|$ for all waveforms. However, ECAP and RRT especially increases at the highly stagnant regions. $ECAP_{max}$ and RRT_{max} for Base are 3 times larger than that of Case 1 with low stagnancy.

To investigate the effect of flow waveform on the behavior of rheology models, instantaneous WSS distributions, swirling strength and shear rate contours are plotted in Fig. 5.5. Mid diastolic phase ($t = 0.73$ sec) is selected because in literature, it is reported that the most significant deviations between Newtonian and shear thinning models are observed at diastolic phase due to low flow rate. From the contours of shear rate, $\dot{\gamma}$, it is obvious that for most of the regions inside the bulge, $|\dot{\gamma}|$ is small for Case 1, while $|\dot{\gamma}| > 50 \text{ s}^{-1}$ around the primary vortex. Newtonian model overestimates the WSS peak, $\dot{\gamma}$ distribution and vortex patterns, compared to shear thinning models. WSS distributions, patterns of λ_{ci} contours and their locations are very similar for Casson and Quemada models, which is well-in-line with the findings of Skiadopoulos et al. (2017). Carreau and Power models predict very similar λ_{ci} patterns and WSS distributions, which is compatible with findings of Shibeshi and Collins (2005). Although they are not demonstrated, in preliminary studies, the Carreau-Yasuda, Cross, Modified and Simplified Cross models are also tested. Results obtained by Carreau-Yasuda, Cross and Modified Cross are the same with Carreau and Power-1, while Simplified Cross obtain very similar hemodynamic parameters with Casson and Quemada for each flow waveform patterns. For the Case 2, $|\dot{\gamma}| > 50 \text{ s}^{-1}$ is obtained near the distal region and at the centerline of the aneurysm, while it is near to zero at the near-wall proximal and central regions. At the regions with high shear rate, contours of λ_{ci} and WSS distribution obtained by shear-thinning models are converged to Newtonian case. Therefore, even $|\dot{\gamma}| \approx 50 \text{ s}^{-1}$ might be sufficient to utilize Newtonian assumption.

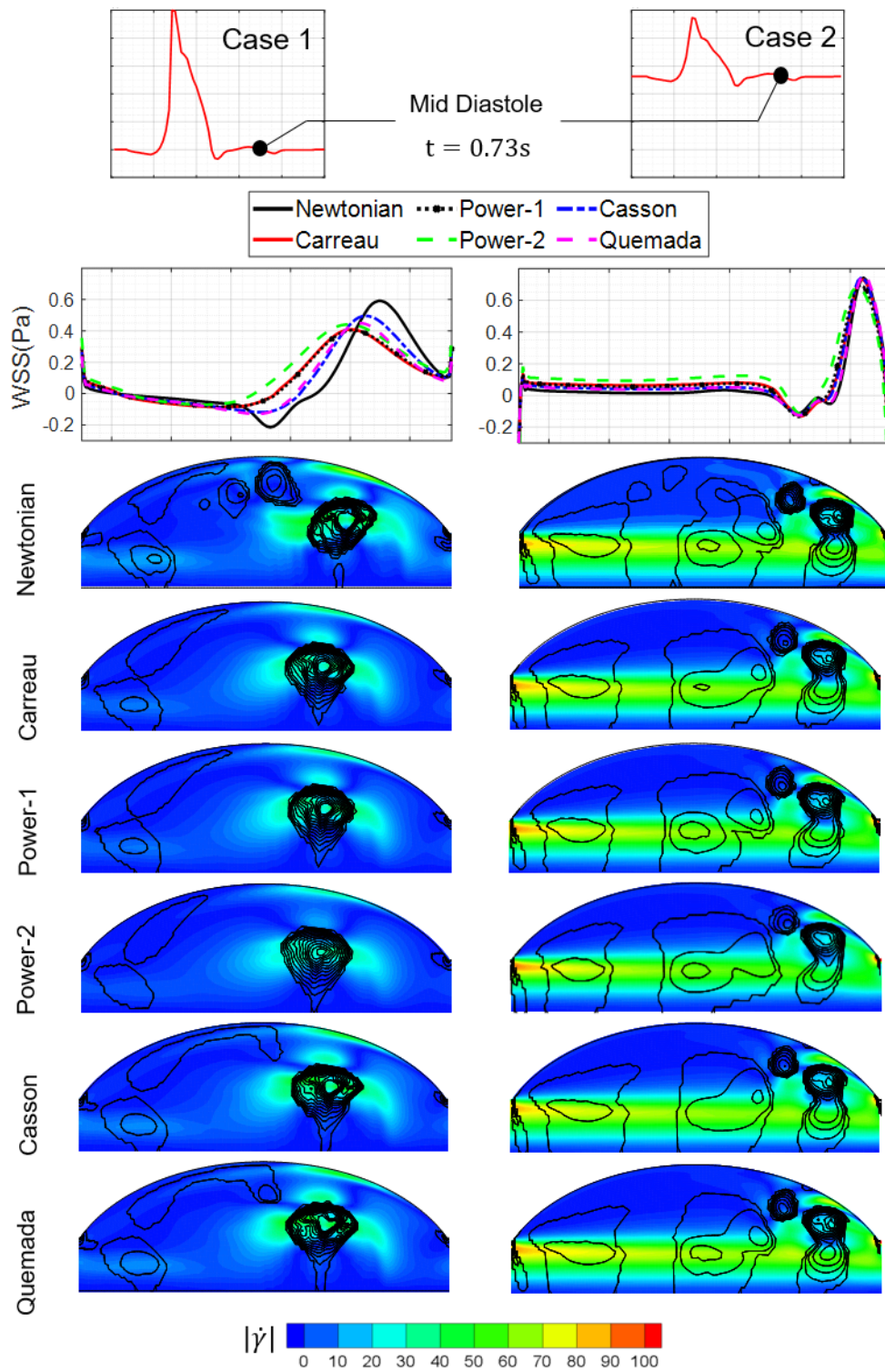


Figure 5.5. Comparison of WSS distributions, swirl strength and shear rate contours of Newtonian and selected shear-thinning rheology models for the Case 1 and 2

Figure 5.6 shows contours of time-averaged swirling strength, $\overline{\lambda_{ci}}$, and streamlines together with contours of time-averaged shear rate, $\overline{\dot{\gamma}}$. For the Base case, $|\overline{\dot{\gamma}}|$ is smaller than 10 s^{-1} throughout the bulge. Newtonian model overestimates the vortex structures. For Base model with low shear rates, none of the shear-thinning models predict the second primary vortex. Non-Newtonian behavior in low shear zones minimizes the extend of recirculation, as reported by Soulis et al. (2008). For the Case 1 and 2, $|\overline{\dot{\gamma}}|$ throughout the bulge is larger and all rheology models can predict primary, second primary and secondary vortices, despite the Power-2 model. For Case 2, $|\overline{\dot{\gamma}}|$ for distal region and in proximity to the centerline or artery is larger than 70 s^{-1} , and the predictions of all shear-thinning models are more similar to the Newtonian. On the other hand, for Case 1, $|\overline{\dot{\gamma}}| > 70 \text{ s}^{-1}$ region is smaller than Case 2, and Newtonian model significantly overestimates each vortex structure, it obtains even a tertiary vortex. Predictions of Quemada and Casson models resemble the Newtonian, but vortex predictions of Carreau and Power models are more conservative.

However, estimation of WSS parameters with different rheology models demonstrate an unexpected pattern. In Figure 5.7, OSI and ECAP distributions obtained by different rheology models for the waveforms Base, Case 1 and 2 are presented. Even high flow rates like the Case 1 and 2, Newtonian model presents overestimated OSI and ECAP distributions. OSI and ECAP distributions obtained by Casson and Quemada are nearly the same with each other, and closer to Newtonian pattern at each flow waveform. On the other hand, OSI and ECAP estimations of Carreau and Power-1 model are very similar, while Power-2 model is significantly conservative and fails to obtain OSI and ECAP patterns especially around secondary vortex.

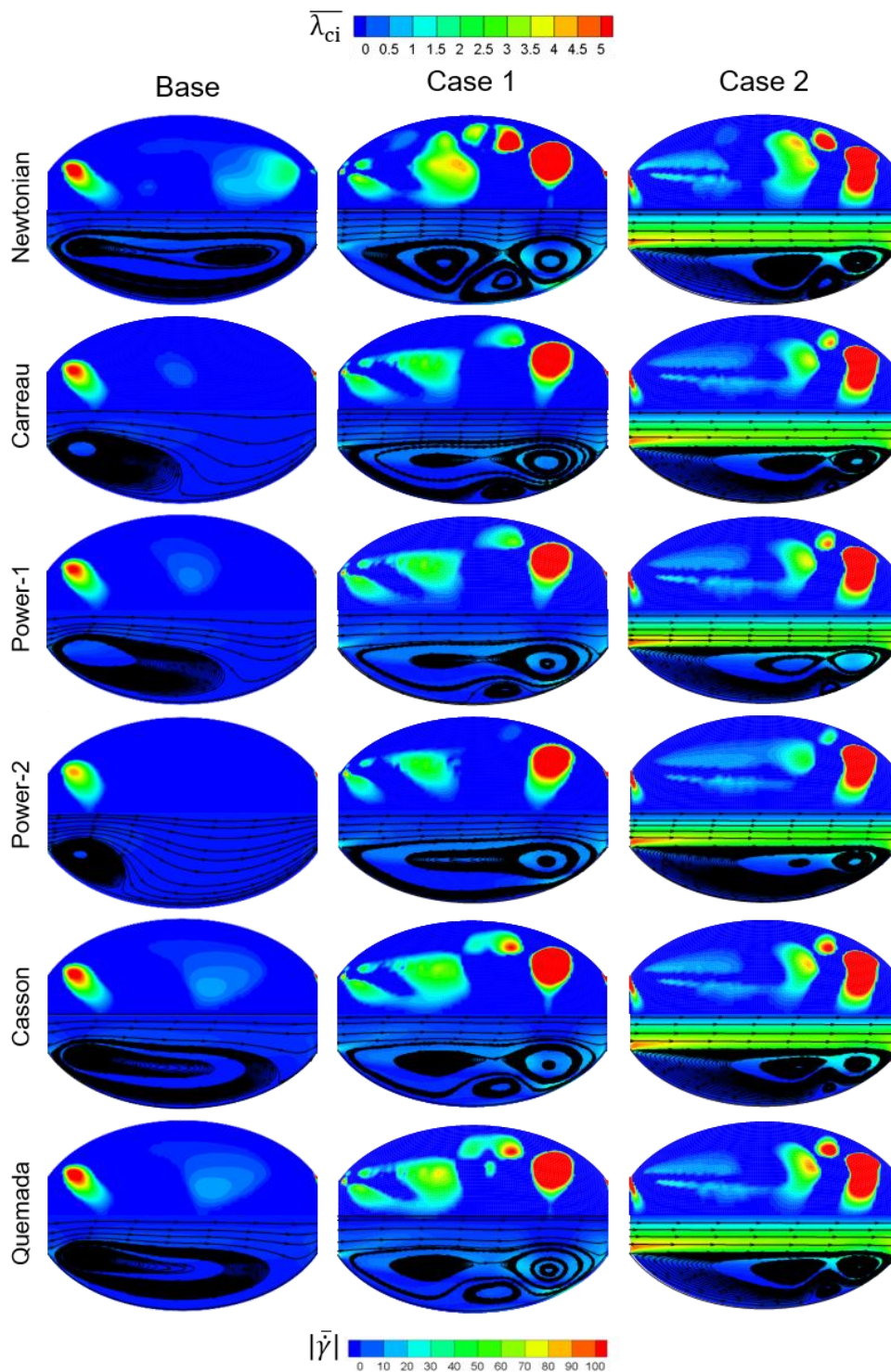


Figure 5.6. Comparison of time-averaged streamline patterns, swirl strength and shear rate contours of selected rheology models for the waveform patterns, Base, Case 1 and 2

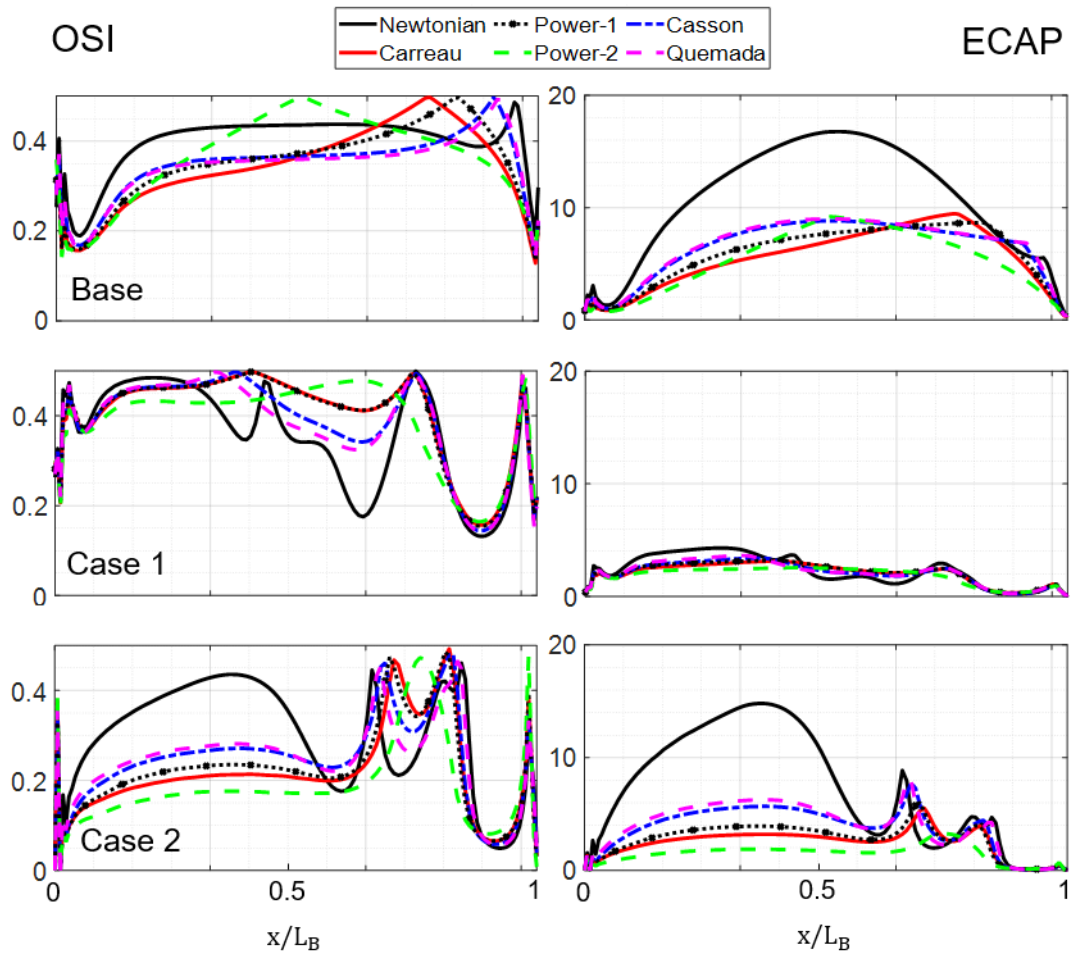


Figure 5.7. Comparison of OSI and ECAP distribution on the aneurysm wall of selected rheology models the waveform patterns, Base, Case 1 and 2

In Figure 5.8a, swirling strength contours and streamline patterns for the Base waveform are presented for Newtonian, Viscoelastic, Quemada and Carreau models at mid-diastolic phase, $t = 0.73$ sec. Diastolic phase of Base model is selected because Oldroyd-B model could not provide a stable solution for high Reynolds numbers (Elhanafy et al., 2019; Leuprecht and Perktold, 2001). Also, elastic nature of blood is dominant at low shear rates (2011). Viscous part of the viscoelastic Oldroyd-B model is Newtonian, not shear-thinning. Therefore, the only reason for the difference between Newtonian and Viscoelastic results is the elastic effects. Viscoelastic model predicts a smaller primary vortex, which is closer to the inlet region of aneurysm bulge, compared to others. Due to conservative nature of Carreau model, it only

obtains primary vortex. Second primary vortex is observed from the streamlines and contours of λ_{ci} of Newtonian, Viscoelastic and Quemada models, but at different locations. Second primary vortex obtained by Newtonian model is located near to distal region, while it is located at the central zone for Viscoelastic and Quemada models. In Figure 5.8b, time-averaged swirl strength contours, $\overline{\lambda_{ci}}$, and streamline patterns of those rheology models for Base waveform is presented. Despite the mid-diastolic phase, location of time-averaged vortex cores and $\overline{\lambda_{ci}}$ distribution obtained by Newtonian and Viscoelastic models are more similar. However, the $\overline{\lambda_{ci}}$ contours and time-averaged streamlines of viscous shear thinning models are significantly different from Newtonian and Viscoelastic models, and they can only predict the primary vortex structure.

5.2 Discussion

In the current study, the behaviors of Newtonian, viscous shear-thinning and viscoelastic rheology models at different inlet flow waveforms are investigated. For this purpose, three inlet waveform patterns, with different peak systolic and diastolic flow rates are utilized. First of all, the variations of vortex structure and WSS parameters at those inlet flow conditions are observed by using Carreau model. From vorticity transport equation (Smith, 2018), it is known that acceleration of bulk flow is the main source of vortex generation for such 2D physiological flows, while vortex transport is accomplished by advection of vortex by means of bulk flow and viscous diffusion. The primary vortex generated by Case 1, the waveform pattern having largest acceleration, conserves its strong identity with small diffusion.

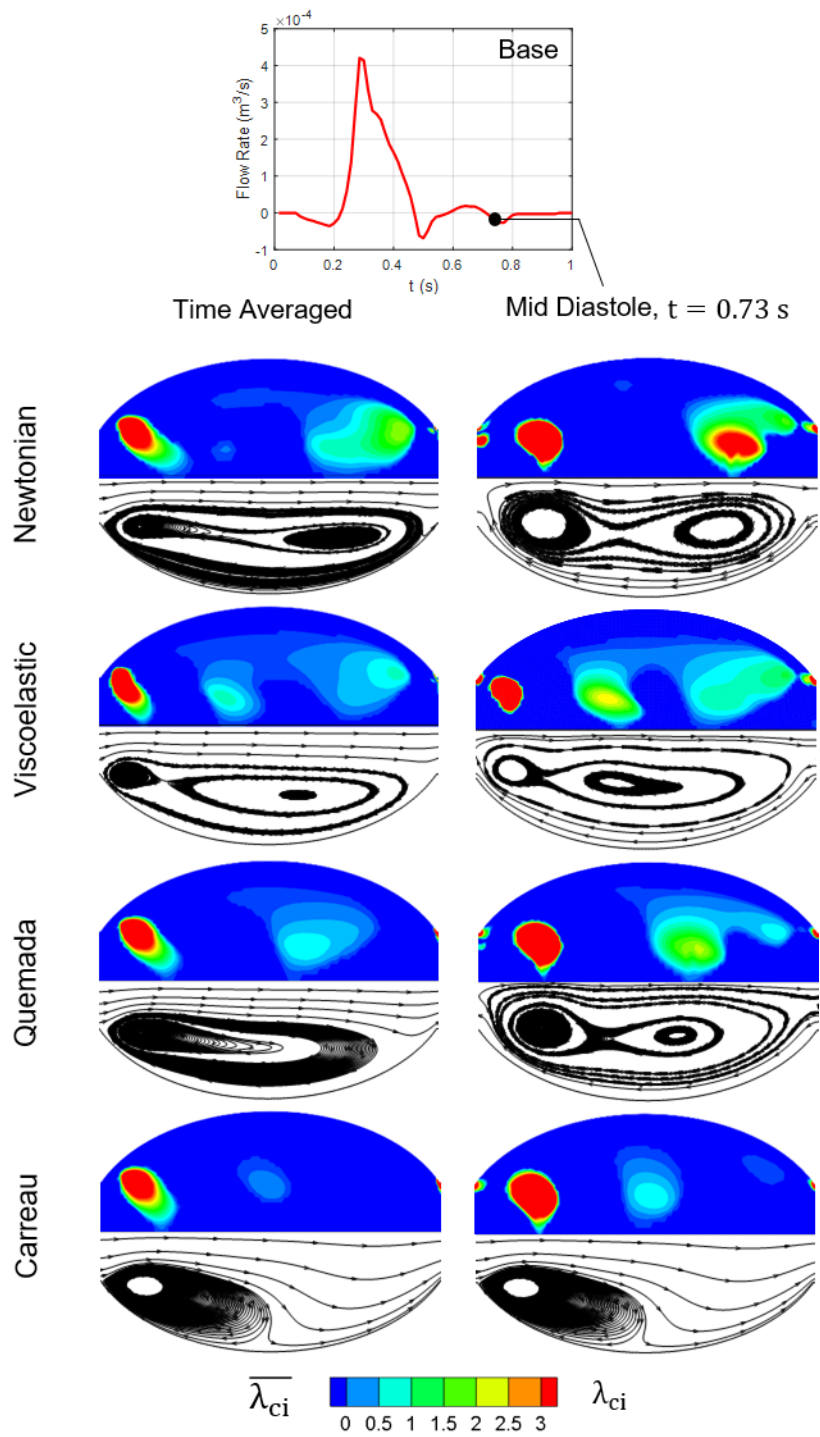


Figure 5.8. Comparison of a. swirl strength contours and streamline patterns b. time-averaged swirl strength contours and streamline patterns of different rheology models for Base

For Case 1, transportation of that vortex to distal site continues until the end of the cardiac cycle, $t = 1$ sec. Due to its significant advection capacity, the vortex pattern generated by Case 2 is transported to distal site until the end of systolic phase, $t = 0.5$ sec, and it reserves that position throughout the diastolic phase. This behavior affects the WSS parameters significantly. OSI magnitudes for Case 1 are larger than other patterns through the bulge, which might be related with vortex transportation. The vortex is transported throughout the cycle without settling a specified zone for a long time and thus generates an oscillatory flow pattern, leading to high OSI. Hence, not only strength of the vortex, but also its transportation mechanism affects the distribution of WSS parameters, ILT formation and growth process. However, the stretching and tilting effects are should be checked in further studies by using 3D geometries.

From the results obtained with different rheology models at three waveform patterns, it is observed that inside the aneurysm bulge, in addition to shear rate distribution, the vortex transport phenomenon is also a determinant in rheology model selection. In literature, it is reported that, Newtonian model assumption is applicable for large flow rates (Soulis et al., 2008). From the results presented in Figure 5.4, for diastolic phase with a low flow rate, Newtonian model overestimates WSS distribution and vortex patterns, followed by Quemada and Casson, while Carreau and Power models are more conservative. For regions with $|\bar{\gamma}| > 50 \text{ s}^{-1}$, on the other hand, Newtonian and shear-thinning model predictions demonstrate a similar pattern. Also, $\bar{\lambda}_{ci}$ contours and streamlines agree this hypothesis. For the Base and Case 1, having low shear rates inside the bulge, Newtonian overestimates time-averaged vortex patterns, even shear thinning models have variations between each other. However, for Case 2 having high shear rate zones inside the bulge, swirling strength contours obtained by shear-thinning models are very similar, and closer to the $\bar{\lambda}_{ci}$ contours of Newtonian case. Although instantaneous WSS distributions, λ_{ci} and $\bar{\lambda}_{ci}$ contours agree that Newtonian model is applicable especially for high mean flow rates, there is a significant difference in OSI and ECAP distributions of Newtonian and shear-thinning models for the Case 2. On the other hand, despite its smaller mean flow rate

and shear rate distribution, the difference of OSI and ECAP distributions for Newtonian and shear thinning models for Case 1 is comparably small. The reason might be related with vortex transport mechanism. In Appendix D, temporal evolution of shear rate distribution inside the bulge for three waveform models are presented. Together with the vortex structure, larger $|\dot{\gamma}|$ region is also transported through the bulge. Although Case 1 could not obtain large $|\dot{\gamma}|$ through the aneurysm, transport of vortex pattern is slow, eliminating the long stagnation at specified sections inside the sac. However, for Case 2, transport of vortex pattern is accomplished in a very short time, leading a highly stagnant flow structure at proximal and central regions. In those highly stagnant regions, there is 40% difference between Newtonian and Carreau models, together with a 20% difference between Quemada and Carreau models. Arzani et al. (2018) stated that for the stagnant regions, non-Newtonian models should be used. According to Arzani et al. (2018), Carreau-Yasuda model overestimates the non-Newtonian effects, and the results of this study are compatible with this conclusion. Predictions of Carreau, Carreau-Yasuda, Cross and Modified Cross models are very similar not converging to Newtonian model, even with increasing shear rate. On the other hand, Casson, Quemada and Simplified Cross are nearly identical with each other and closer to Newtonian model for lower shear rates, while they diverge from Newtonian with increasing shear rate at systolic phase. However, at diastolic phase, Power model presents non-Newtonian behavior for low shear rates, while it converges to Newtonian at peak systole with increasing shear rate.

Morbiducci et al. (2011) stated that for the carotid artery, Newtonian model predictions for OSI and ECAP are sufficient, while bulk flow metrics such as velocity distribution are nearly the same with shear thinning models. Also, they reported that, outflow boundary condition selection is more important than rheology model selection. In the current study, it is demonstrated that any difference in inlet waveform characteristics significantly changes hemodynamics. However, for AAA, shear-thinning rheology model selection is as much effective as inlet waveform characteristics, especially in OSI and ECAP estimations, even for high mean flow

rates. Even selection of constants for shear-thinning models significantly affects the hemodynamics. In literature, for Power model, Shibeshi and Collins (2005) and Cho and Kensey (1991) and have proposed two different constants. Power-2 model seems to underestimate the vortex patterns and WSS parameters. Therefore, in order to simulate exact patient-specific hemodynamics for AAA, it might be necessary to utilize shear-thinning models with exact patient-specific constants (Saqr et al., 2020), even for large mean flow rates.

In addition to viscous shear thinning models, viscoelastic rheology model also present variations from Newtonian especially in terms of locations of vortex patterns. On the other hand, the difference between time-averaged swirling strength and streamline patterns obtained by Viscoelastic and Newtonian model is small, compared to viscous models, even low $|\dot{\gamma}|$. Bodnar et al. (2011) reported that, effect of elasticity of blood on hemodynamics through stenosis might be negligible, compared to shear-thinning viscous effects. The same conclusion might be applicable for AAA hemodynamics, especially at high mean flow rates.

CHAPTER 6

A CORRELATION BETWEEN WALL SHEAR STRESS PARAMETERS AND VORTEX IDENTIFICATION METHODS

Wall shear stress (WSS) parameters such as time-averaged wall shear stress (TAWSS), oscillatory shear index (OSI), endothelial cell activation potential (ECAP) and relative residence time (RRT) are generally utilized to predict regions of intraluminal thrombus (ILT) formation inside abdominal aortic aneurysms, while the effect of vortex structure on ILT formation is not clear. Moreover, obtaining WSS parameters is a challenging issue in experimental studies due to limitations arising in proximity to the wall, while acquiring vortex structures with vortex identification techniques such as swirling strength (λ_{ci}), Q -criterion, and λ_2 -criterion, is a very common approach. In the current study, the correlation between vortex identification techniques and WSS parameters is investigated. Numerical simulations are conducted for a physiological flow pattern at a mean Reynolds number of 670. Three aneurysm models with bulge radius to aorta radius ratios of 2.44, 3.66 and 4.88 are used to generate different vortex patterns.

6.1 Results

Figure 6.1 shows temporal evolution of instantaneous WSS, contours of swirl strength, λ_{ci} , and streamline patterns obtained for Model 1 at different time instants. Considering the patterns at $t = 0.3$ sec, a primary vortex structure starts to separate from the aneurysm wall at the proximal region of the bulge, with a large swirl strength magnitude near to the wall, resulting in a sudden WSS peak. Throughout the remaining parts of the bulge, an attached flow structure is observed. At $t = 0.4$

sec, the primary vortex separates from the proximal end, and a weak WSS bump is present around the primary vortex. At $t = 0.5$ sec, which is the end of the systolic phase, the primary vortex core reaches the mid-plane of the bulge, and it is dissipated into the whole bulge. Magnitude of swirl strength is non-zero throughout the sac, together with a non-zero WSS.

At the early diastolic phase, $t = 0.6$ sec, the primary vortex reaches the distal region, by maintaining its strength. The vortex core, which has the highest swirl strength magnitude, is very close to the wall, creating a WSS peak of magnitude 1 Pa, while the remaining parts of the bulge having nearly zero WSS. At $t = 0.7$ sec, streamline pattern indicates another vortical structure formation at the proximal region, rotating in the same direction with the main vortex. It has a distinct core and can be considered as the second primary vortex. In addition, a third structure, which rotates opposite to the primary vortex and might be named as secondary vortex, appears near the wall. Second primary vortex structure is not close to the wall, and it is not affecting the WSS distribution. But there is a weak negative WSS peak around the secondary vortex structure.

Although the area covered by the primary vortex decreases due to the generation of other vortex structures, the WSS magnitude is still near 1 Pa. Since a large $|\lambda_{ci}|$ contour encloses a significant portion of the near-wall area at the proximal region, the $|WSS|$ maintains a large value. Similar streamline patterns and vortex structures are observed at $t = 0.2, 0.8$ and 0.9 sec, but the magnitude of swirl strength for each vortex structure are less at the mid and late diastolic phases due to viscous dissipation. Moreover, size of the near-wall large $|\lambda_{ci}|$ areas for those time instants are clearly smaller than the size of the corresponding areas at $t = 0.6$ and 0.7 sec. In accordance with swirl strength magnitudes, patterns, and near-wall areas enclosed by large $|\lambda_{ci}|$ contours, there is a decrease in the WSS peaks, too.

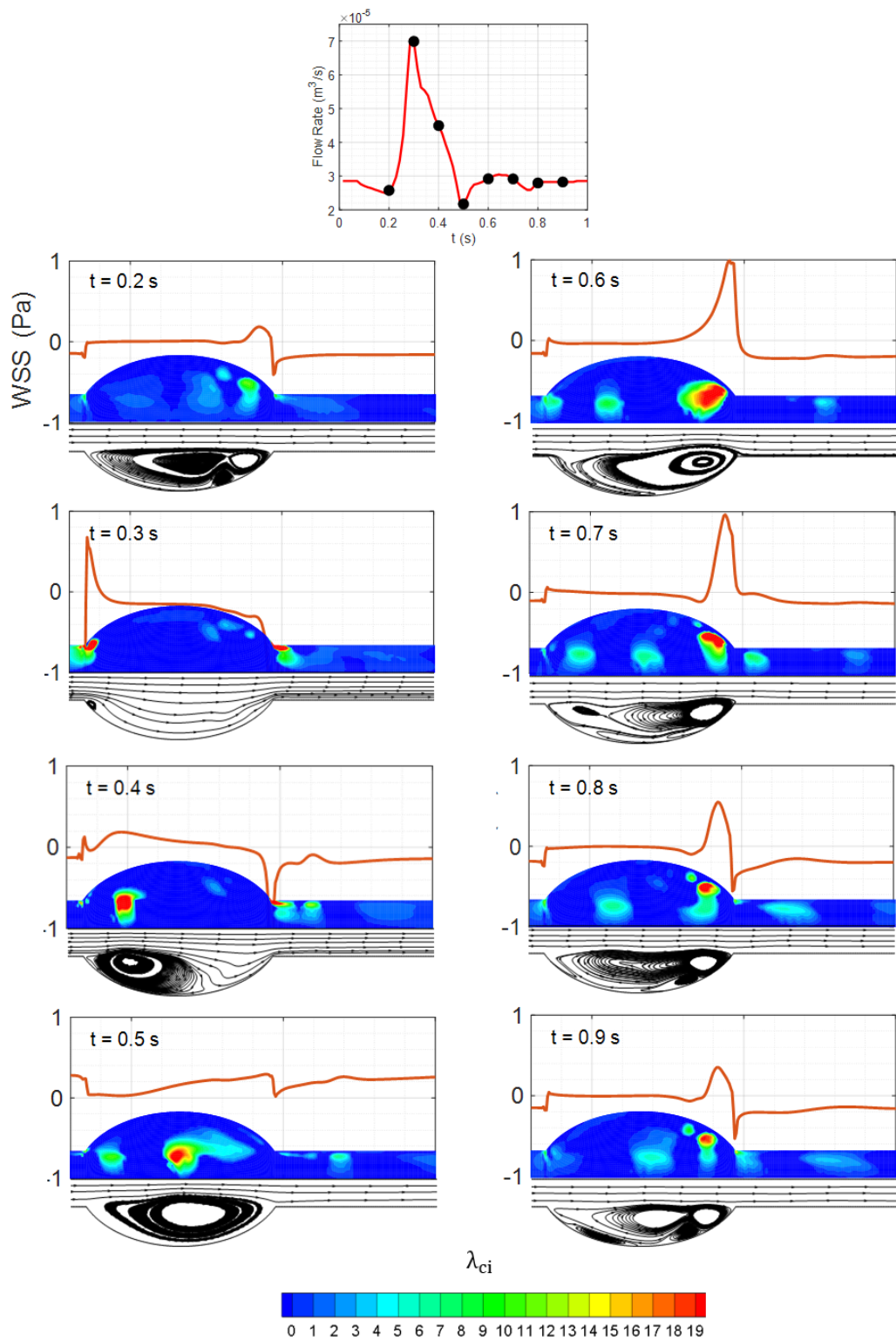


Figure 6.1. Temporal evolution of instantaneous WSS, contours of swirl strength, λ_{ci} , and streamline patterns for the Model 1

Figure 6.2 shows contours of vortex identification measures and variations of WSS parameters for Model 1. Contours of vortex identification measures and streamline pattern are plotted by using time-averaged velocity components throughout a cycle. All three vortex identification measures give nearly similar results, as expected from a 2D simulation (Chen et al., 2015). According to the contours of vortex identification measures and streamline patterns, for the proximal and central regions of the bulge ($0 < x/L_B < 0.65$), magnitude of $\overline{\lambda_{ci}}$ is comparably small, while it is significantly large at the distal section of the bulge ($0.65 < x/L_B < 1$). The primary vortex core appears at the distal end of the bulge with a significantly large magnitude. A second primary vortex with smaller magnitude appears closer to the central-plane, but away from the wall, and a secondary vortex structure with larger magnitude than the second primary vortex is placed just above the primary vortex core in close proximity to the wall. TAWSS value through the proximal and central parts of the bulge is very small, nearly equal to 0.05 Pa, and reaches 0.1 Pa between $x/L_B = 0.65 - 0.8$ where the secondary vortex structure is apparent. But its magnitude increases around the primary vortex structure, reaching 0.4 Pa between $x/L_B = 0.8 - 1$. Unlike TAWSS, OSI is high for the proximal and central regions of the bulge, where the magnitude of $\overline{\lambda_{ci}}$ is small. In addition, at the reattachment and separation points of the secondary vortex structure, which can be seen from the streamlines, there are OSI peaks reaching nearly 0.5, which is the overall maximum value. However, OSI value decreases at the high-intensity $\overline{\lambda_{ci}}$ regions near the wall, where primary and secondary vortex structures are located. For very large $\overline{\lambda_{ci}}$ magnitudes observed for the primary vortex structure, OSI magnitude becomes smaller than 0.1. Interestingly, at the reattachment point of the primary vortex structure, located at the exit of the bulge, OSI increases again but it is smaller than the OSI peaks generated by the secondary vortex.

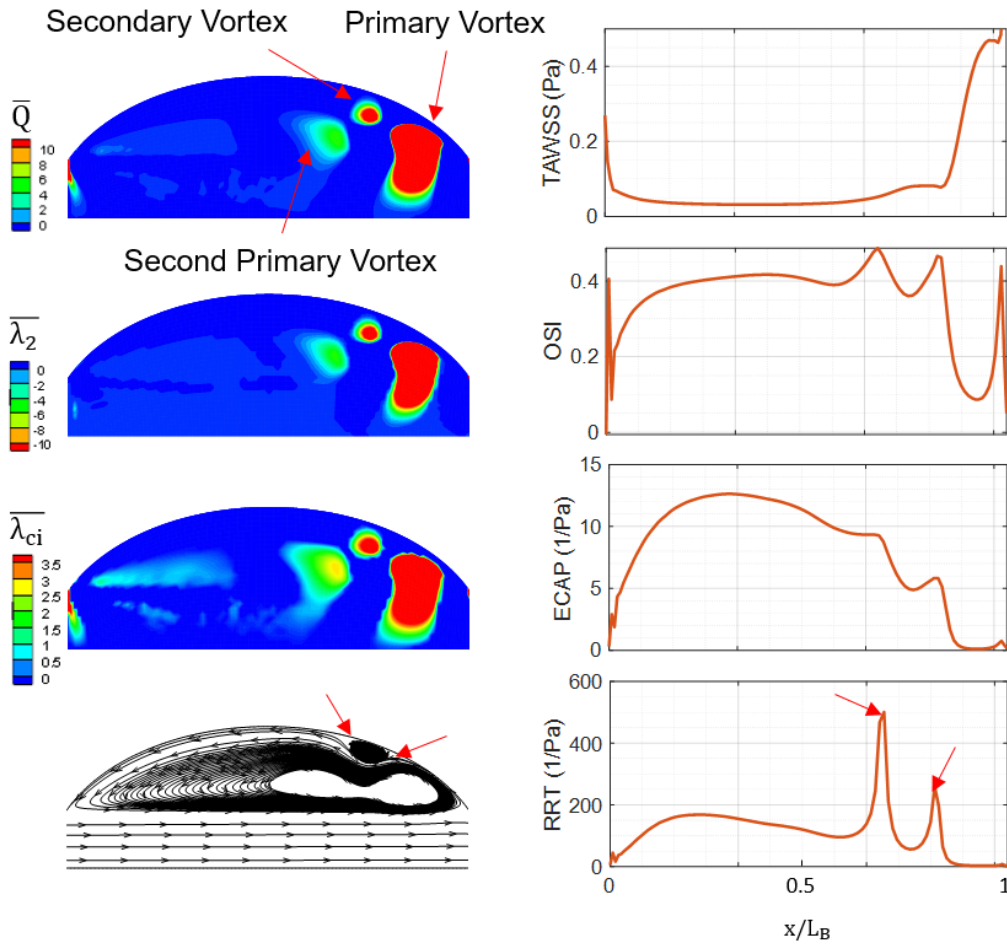


Figure 6.2. Contours of \bar{Q} -criterion, $\bar{\lambda}_2$ -criterion, swirl strength, $\bar{\lambda}_{ci}$, streamline pattern, and TAWSS, ECAP, OSI and RRT variations on the aneurysm wall for Model 1

Similar with OSI, ECAP and RRT magnitudes are also high for the proximal and central regions of the bulge. ECAP decreases continuously after $x/L_B = 0.65$, and it reaches to zero for the distal region where the primary vortex structure with high $|\bar{\lambda}_{ci}|$ is located. However, like OSI, RRT distribution shows peaks after $x/L_B = 0.65$, at the reattachment and separation regions of the secondary vortex structure. However, RRT is more sensitive to the vortex reattachment and separation. Similar to ECAP, RRT is also zero around the primary vortex structure with high $|\bar{\lambda}_{ci}|$, and no RRT peak is apparent at its reattachment point. This might be related to the

magnitude of $\overline{\lambda_{cl}}$. At the reattachment and separation points of vortex structures with a high $|\overline{\lambda_{cl}}|$, OSI and RRT peaks might be smaller than the peaks occurring at the reattachment and separation points of vortices with small $|\overline{\lambda_{cl}}|$.

To see the effect of aneurysm size on the vortex structures and their corresponding influence on wall shear stress, two additional models with larger bulge diameters, i.e. $R_B/R = 3.66$ and 4.88 , are studied. Figure 6.3 shows the temporal evolution of the instantaneous WSS distributions, contours of swirl strength, and streamline patterns of Models 2 and 3. For both models, at $t = 0.5$ sec, which is the end of the systolic phase, the primary vortex covers the whole aneurysm bulge, and the vortex core has passed the mid-plane. For Model 2 and 3, due to increased diameter, the distance between high swirl region and wall is larger. This results in almost zero WSS distribution through the bulge with only non-zero WSS peak at the distal area, where near-wall swirl strength contours appear. At $t = 0.6$ sec, the primary vortex structure reaches the distal site and a secondary vortex structure is generated for Model 2, but not for Model 3. However, at the same instant, for Model 3, the primary vortex structure is divided into two, and a second primary vortex core is generated, with swirl strength magnitude smaller than that of the primary vortex. Compared to Model 1, the primary vortex cores are much closer to the wall and their swirl strength magnitudes are larger over a greater spatial extent. Therefore, a sharp WSS peak reaching 2.5 Pa is seen for both models. At $t = 0.7$ sec, secondary vortex structure is also generated for Model 3, located at the mid-plane, in close proximity to the wall. Secondary vortices of both models are not witnessed in the swirl strength contours due to their small magnitudes (<1). In addition, for both models, a tertiary vortex structure, which has very small spatial extent but high strength swirl magnitude, is generated over the primary vortex. Its footprint on WSS distribution is a small peak due to its closeness to the wall.

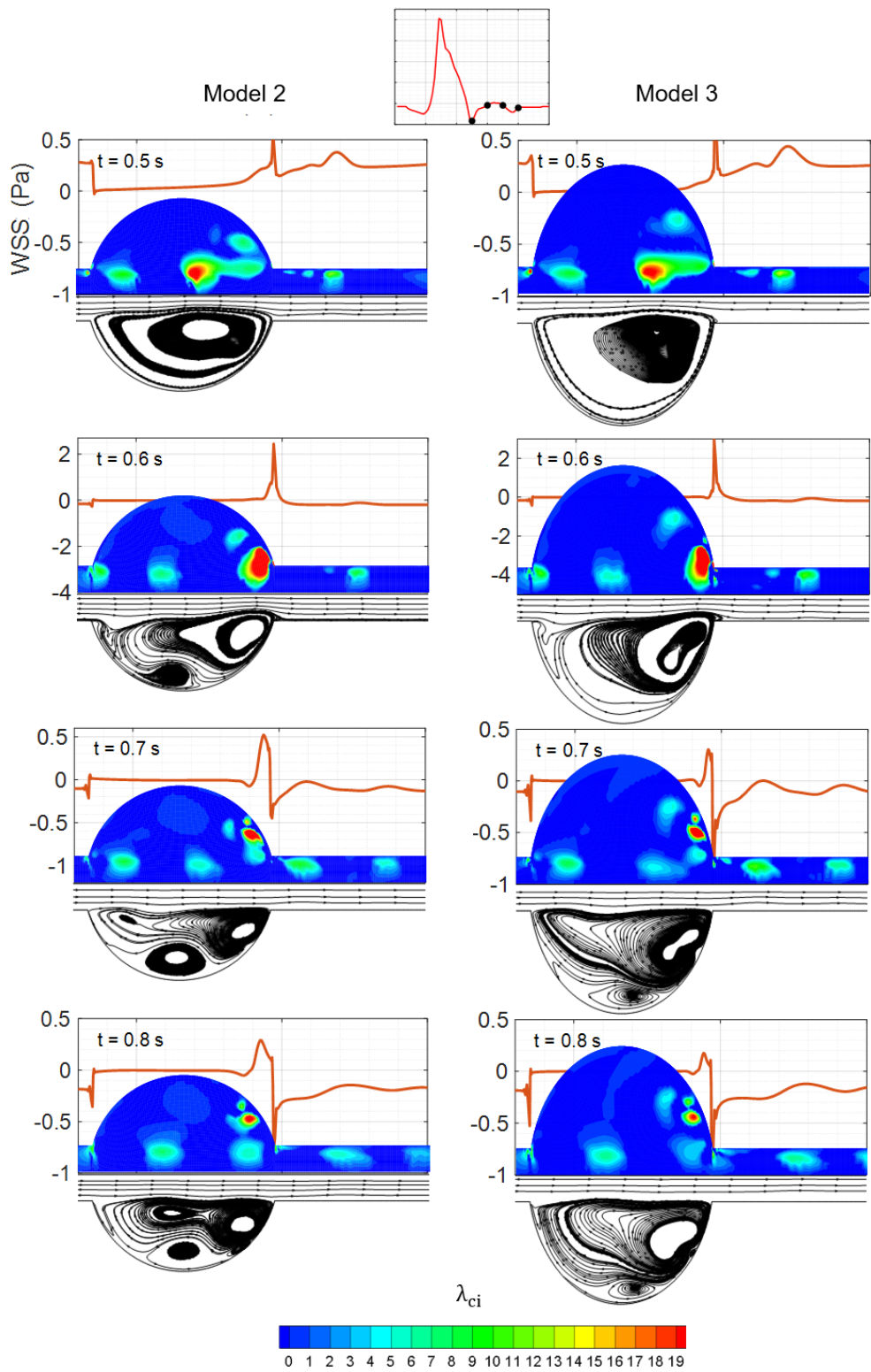


Figure 6.3. Temporal evolution of instantaneous WSS, contours of swirl strength and streamline patterns obtained for Models 2 and 3

To investigate the correlation between WSS parameters and vortex identification techniques further, a detailed comparison of them for all three models is given in Figure 6.4. According to contours of $\overline{\lambda_{cl}}$ and streamline patterns, for the proximal and central regions of the bulge ($0 < x/L_B < 0.65$), magnitude of $\overline{\lambda_{cl}}$ is comparably small. The primary vortex core is located at the distal end of the bulge with a large magnitude for all models. With increasing diameter of the bulge, the primary vortex structure gets larger. However, the magnitude of $\overline{\lambda_{cl}}$ decreases due to dissipation of the vortex pattern into a larger area. A second primary vortex with smaller magnitude is located near the central region of the bulge, but its focal point disappears and the intensity of $\overline{\lambda_{cl}}$ contours significantly decreases with increasing bulge diameter. A secondary vortex with larger $\overline{\lambda_{cl}}$ magnitude than the second primary vortex forms just above the primary vortex core, very close to the artery wall. The core of the secondary vortex moves toward the central region of the bulge for the models with increasing bulge diameter, and it disappears from the $\overline{\lambda_{cl}}$ contour plot for Model 3. In addition, with increasing diameter, magnitude of $\overline{\lambda_{cl}}$ at the focal points of streamlines of vortices decreases.

TAWSS values through the proximal and central parts of the bulge are smaller than 0.025 Pa for Model 2 and 3, which is nearly 0.05 Pa for the Model 1. Between $x/L_B = 0.8 - 1$, it reaches 0.4 Pa for Model 1, but TAWSS values for larger models can reach that value only at $x/L_B = 1$. Unlike TAWSS, OSI is high at low $\overline{\lambda_{cl}}$ regions. Around the primary vortices, because $|\overline{\lambda_{cl}}| > 4$, OSI value is significantly small for all models. Although Model 1 has intense swirling strength contours compared to others at the distal region, its OSI_{min} is slightly larger because high swirl area for Model 2 and 3 covers wider region in proximity of the wall. Also for Model 3, intensity of $\overline{\lambda_{cl}}$ contours are lower because the primary vortex structure is dissipated, which leads to higher OSI than the other two models at that zone. At the reattachment and separation points of the secondary vortex of all models, OSI reaches its maximum value, while it decreases through the secondary vortex, between its separation and reattachment. ECAP distribution is significantly affected

from the bulge diameter. Maximum ECAP of Model 3 is ten times higher than that of Model 1. For Model 2 and 3, high ECAP region is located around the large scale swirling structure with $|\overline{\lambda_{ci}}| < 1$. The magnitude of ECAP reaches zero at the distal region where the primary vortex is located, and the magnitude of $\overline{\lambda_{ci}}$ is high for all models. From RRT distributions, it is clear that RRT is highly sensitive to vortex reattachment and separation, and for Model 2 and 3 its magnitude is significantly high at the reattachment point of large-scale swirling structure with low swirl strength. RRT_{max} of Model 3 is not visible because the vertical axis of RRT distribution is constrained to observe RRT distribution of Model 2. The peak values are strongly affected from diameter because increasing diameter also increases the stagnant flow features inside the sac, and generates large-scale swirling structures with significantly small swirl strength, which is correlated with high OSI, ECAP and RRT. Especially for Model 3, $|\overline{\lambda_{ci}}|$ is significantly small around the secondary vortex reattachment point, where a strong RRT peak is observed. RRT_{max} value obtained by Model 3 is 30 times higher than that of Model 1, for which $|\overline{\lambda_{ci}}|$ of the secondary vortex is significantly higher than other models.

6.2 Discussion

To determine the relation between instantaneous WSS distributions and the swirl strength, hemodynamics inside three aneurysm models with different bulge radius to aorta radius ratios is examined. Around a near-wall vortex structure with high swirl strength magnitude, there is a WSS peak with a magnitude that is positively correlated with the magnitude of the swirl strength. The largest WSS peak is observed at early diastole for all models. The primary vortex structure is dissipated into second primary, secondary and tertiary vortex structures and due to the dissipation, its λ_{ci} magnitude decreases, together with its WSS magnitude. Moreover, with increasing bulge diameter, their spatial extends get larger and those vortical structures are being dissipated with reductions in their swirl strength magnitudes. As a result, with increasing aneurysm bulge diameter, several large-

scale swirling structures with very small swirl strength magnitudes are generated. Although it is known that near-wall vortex structures are correlated with high WSS magnitudes at those locations (Biasetti et al., 2011; Biasetti et al., 2012; Bauer et al., 2020), each and every near-wall recirculation observed in streamline patterns might not affect WSS distribution. The size of the secondary vortex is significantly larger than that of the tertiary vortex in terms of streamline patterns, and both appear close to the wall, but only the tertiary vortex with higher swirl strength magnitude has an impact on the WSS distribution. Thus, the near-wall, high-magnitude swirl strength can be correlated with high magnitude WSS peaks, but there is no correlation between the size of a near-wall recirculation and WSS distribution.

In literature, aneurysm hemodynamics is generally quantified by WSS parameters and there are different approaches about the relation between ILT formation and WSS parameters. General argument is that ILT formation and rupture may occur at the low TAWSS, high OSI, ECAP and RRT regions, which are possibly located in a recirculation region (Biasetti et al., 2011; Biasetti et al., 2012; Kelsey et al., 2016; Qiu et al., 2018). On the other hand, Arzani et al. (2014) stated that ILT is observed at regions with low OSI and high TAWSS, where a persistent recirculation region contributes to low OSI. Indeed, the actual effect of recirculation region on ILT formation and its relation with WSS parameters is not clear. Although several studies also reported a qualitative relation between recirculation zones and ILT formation, to the author's best knowledge, the correlation between vortex structure on thrombus formation is not reported quantitatively. For that purpose, in the current study, the correlation between WSS parameters, such as TAWSS, OSI, ECAP and RRT, that are frequently used to determine ILT deposition and rupture regions, and vortex identification methods are studied. The correlation between vortex identification methods and WSS parameters might be a useful tool especially for experimental studies, in which obtaining WSS parameters is a challenge due to experimental constraints.

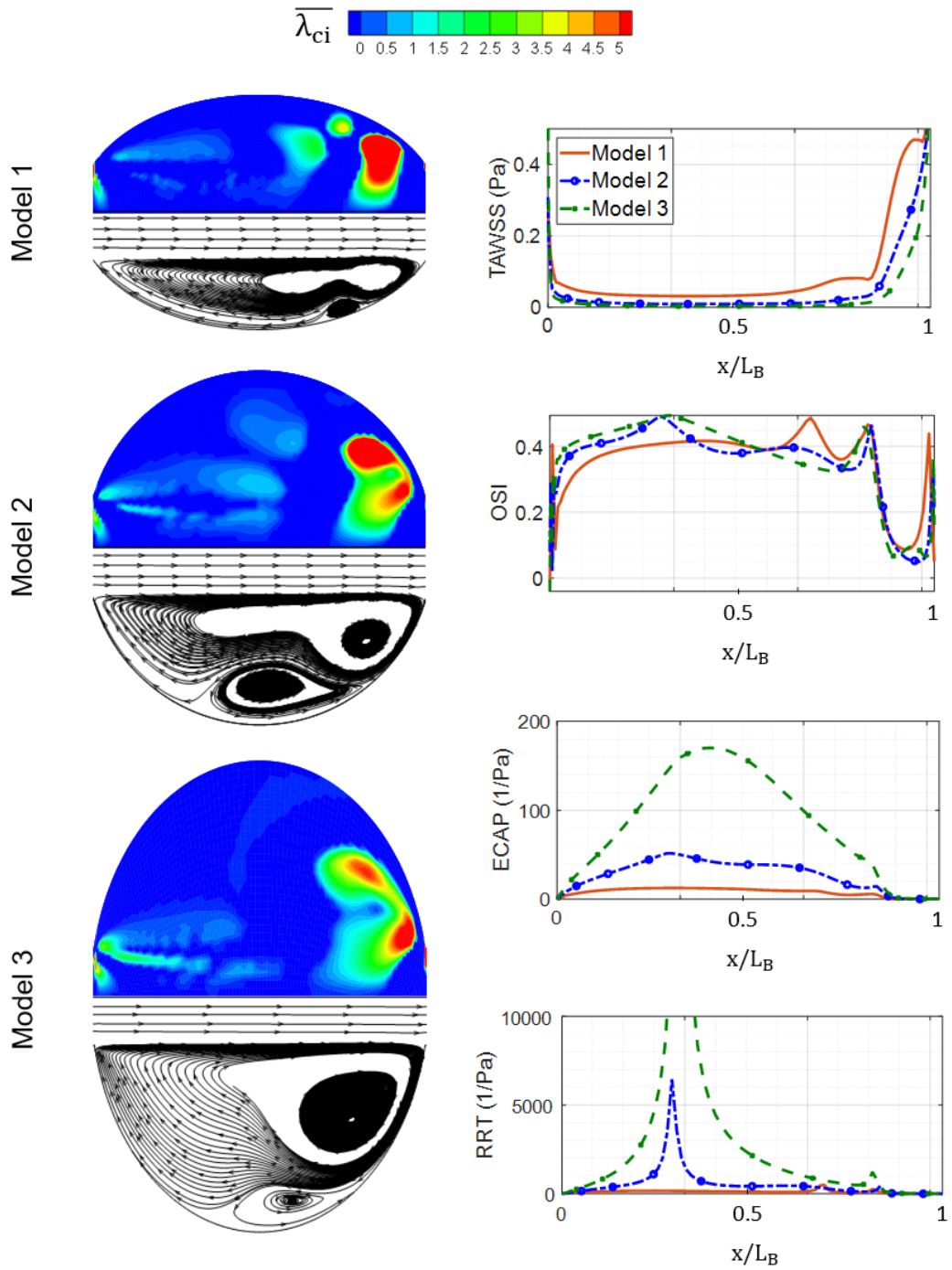


Figure 6.4. Comparison of swirl strength contours, streamline patterns and the variation of WSS measures on the aneurysm wall

Although vortex identification methods such as \bar{Q} -criterion, $\bar{\lambda}_2$ -criterion and $\bar{\lambda}_{ci}$ -criterion obtain nearly the same vortex structures through the bulge, $\bar{\lambda}_{ci}$ can reveal patterns even with a very small magnitude. Biasetti et al. have compared the WSS distribution and vortex patterns which are calculated using λ_2 -criterion (Biasetti et al., 2011; Biasetti et al., 2012), and they also reported that there is a correlation between vortex patterns and WSS distribution. However, λ_2 -criterion discards the weakest vortices (Chen et al., 2015), while λ_{ci} -criterion extract the most number of vortices and can identify even weaker ones. The current study demonstrated that, near-wall vortex patterns even with small λ_{ci} magnitudes can affect the WSS distribution. Therefore, λ_{ci} -criterion might be preferable in WSS comparisons. Although there are different types of recirculation regions throughout the aneurysm bulge, each structure is correlated with different condition. For instance, low TAWSS and high ECAP, OSI and RRT regions are correlated with the secondary vortex structure, with low magnitude of $\bar{\lambda}_{ci}$. On the other hand, in regions with high TAWSS and low OSI, ECAP and RRT, the primary vortex is located, with a high magnitude of $\bar{\lambda}_{ci}$. Large OSI and RRT peaks are observed at the reattachment and separation points of vortices with small $|\bar{\lambda}_{ci}|$. Therefore, to correlate a WSS parameter with a recirculation region, magnitude of $\bar{\lambda}_{ci}$ and the distance between the wall and recirculation should be considered. In Figure 6.4, comparing $\bar{\lambda}_{ci}$ and streamline patterns shows that increasing the aneurysm diameter also increases the scale of the vortices, but decreases the magnitude of $\bar{\lambda}_{ci}$ for each vortex structure. Therefore, it might be concluded that, with increasing bulge diameter, vortices turn into large-scale swirling structures with a stable focus. Indeed, generation of large-scale swirling structures around a focal point might be interpreted as the footprints of vortex dissipation and they possibly have smaller $\bar{\lambda}_{ci}$ magnitudes, leading low TAWSS and high ECAP, OSI and RRT regions. As a result, it might be concluded that vortex identification techniques might also be utilized to predict possible ILT and rupture regions. However, this hypothesis needs to be tested using patient specific geometries of which ILT and rupture regions are known.

CHAPTER 7

CONCLUSION

Intraluminal thrombus (ILT) is observed 80% of abdominal aortic aneurysms (AAA) and might affect rupture characteristics. Disturbed hemodynamics through AAA might affect ILT formation, that are generally quantified by wall shear stress (WSS) parameters such as time-averaged wall shear stress (TAWSS), oscillatory shear index (OSI), endothelial cell activation potential (ECAP) and relative residence time (RRT) in literature. However, modeling parameters such as boundary conditions and fluid properties significantly affect quantification of those hemodynamic parameters. Substantial attention should be drawn during selection of those parameters.

Transient nature of physiological flow is demonstrated by *Womersley* profile. However, in literature, *Parabolic* and *Plug* profiles are also used together with a long entrance length. To observe the differences in WSS parameters and swirling strength contours arising due to inlet velocity profile selection, three different velocity profiles which are *Womersley*, *Parabolic* and *Plug* are utilized for two different mean Reynolds numbers, $Re_m = 340$ and 1160 , and results are compared with a fully-developed Base case. To observe the entrance length requirements of those velocity profiles, three models with differing entrance lengths are used.

In addition to inlet velocity BC, selection of fluid properties is also effective in accuracy of hemodynamic assessment. In the current study, WSS parameters such as TAWSS, OSI, ECAP and RRT together with swirling strength (λ_{ci}) contours are obtained by viscous shear thinning models such as Carreau, Carreau-Yasuda, Cross, Casson, Power, Quemada, Modified and Simplified Cross, and viscoelastic Oldroyd-B are compared with Newtonian model at three inlet flow waveform patterns, which are Base, Case 1 and 2.

In a meta literature analysis study, Saqr et al. (2020) have reported that WSS parameters solely are not enough to bridge hemodynamics and aneurysm pathology. Therefore, to interpret the effect of vortex pattern on ILT formation and also to observe the correlation between WSS parameters and vortex identification methods, such as swirling strength (λ_{ci}), Q -criterion, and λ_2 -criterion, numerical simulations are conducted for a physiological flow pattern at a mean Reynolds number of 670. Three aneurysm models with bulge radius to aorta radius ratios of 2.44, 3.66 and 4.88 are used to generate different vortex patterns. According to those studies, following conclusions might be drawn:

- Instead of *Womersley* profile, for $R_m = 1160$, *Parabolic* profile might be used with an entrance length at least $L_{ent} = 3D$. On the other hand, *Plug* profile cannot obtain similar results with Base condition even $L_{ent} = 11D$ for $R_m = 1160$.
- For $R_m = 340$, *Plug* profile might be utilized rather than *Womersley* profile, with an entrance length $L_{ent} = 11D$. Therefore, it might not be necessary to define the complex *Womersley* profile in physiological flows, especially the cases with high mean Reynolds numbers.
- From the results obtained with different rheology models at three waveform patterns, it is observed that inside the aneurysm bulge, in addition to shear rate distribution, the vortex transport phenomenon is also a determinant in rheology model selection.
- For diastolic phase with a low flow rate, Newtonian model overestimates WSS distribution and vortex patterns, followed by Quemada and Casson, while Carreau and Power models are more conservative. For regions with $|\bar{\dot{\gamma}}| > 50 \text{ s}^{-1}$, on the other hand, Newtonian and shear-thinning model predictions demonstrate a similar pattern.

- In highly stagnant regions, there is 40% difference between Newtonian and Carreau models, together with a 20% difference between Quemada and Carreau models for WSS parameters.
- At diastolic phase, Power model presents non-Newtonian behavior for low shear rates, while it converges to Newtonian at peak systole with increasing shear rate.
- For AAA, shear-thinning rheology model selection is as much effective as inlet waveform characteristics, especially in OSI and ECAP estimations, even for high mean flow rates. Even selection of constants for shear-thinning models significantly affects the hemodynamics.
- Bodnar et al. (2011) reported that, effect of elasticity of blood on hemodynamics through stenosis might be negligible, compared to shear-thinning viscous effects. The same conclusion might be applicable for AAA hemodynamics, especially at high mean flow rates.
- Around a near-wall vortex structure with a high swirl strength magnitude, a large WSS peak is observed.
- Although vortex identification methods such as \bar{Q} -criterion, $\bar{\lambda}_2$ -criterion and swirl strength, $\bar{\lambda}_{ci}$, give nearly the same vortex patterns, $\bar{\lambda}_{ci}$ can reveal the vortex patterns even with a very small magnitude.
- Comparing $\bar{\lambda}_{ci}$ and streamline patterns for Model 1, 2 and 3 shows that increasing the aneurysm diameter also increases the scale of vortex patterns, but decreases the magnitude of $\bar{\lambda}_{ci}$ for each vortex structure.

- With increasing bulge diameter, the vortex structures turning into large-scale, inward-swirling structures with a stable focus.
- Vortex structures having high magnitudes of $\overline{\lambda_{CI}}$ are located at high TAWSS and low OSI, ECAP and RRT regions. Therefore, vortex identification techniques might also be utilized to predict possible ILT and rupture regions. However, this hypothesis is required to be analyzed using patient specific geometries of which ILT and rupture regions are known.

Moreover, following work might be performed in future for better understanding the conclusions:

- To replicate realistic conditions, a physiological pressure waveform might be supplied as the outlet boundary condition.
- To understand the effect of outlet profile on vortex structure, zero pressure outlet condition and physiological pattern might be compared.
- To further investigate the effect of inlet velocity profile, profiles having different inlet directions can be supplied at the inlet. This might be especially important for AAA geometries having a neck angle.
- The effect of wall elasticity and movement on vortex structure can also be observed. For that purpose, an FSI study might be implemented and correlation between WSS parameters and vortex patterns, together with ILT formation can be further checked under those conditions.

- To understand the ILT formation and growth mechanism of AAAs, patient-specific geometries having ILT region can be used to observe the behavior of vortex pattern on ILT zones.

REFERENCES

- Armour, C.H., Guo, B., Pirola, S., Saitta, S., Liu, Y., Dong, Z. and Xu, X. Y. 2021. The influence of inlet velocity profile on predicted flow in type B aortic dissection. *Biomech. Model. Mechanobiol.*, vol. 20, no. 2, pp. 481–490, doi: 10.1007/s10237-020-01395-4.
- Arzani, A., and Shadden, S.C. 2015. Characterizations and Correlations of Wall Shear Stress in Aneurysmal Flow. *Journal of Biomechanical Engineering* 138(1), 014503-014503-014510. doi: 10.1115/1.4032056.
- Arzani, A., Suh, G.-Y., Dalman, R.L., and Shadden, S.C. 2014. A longitudinal comparison of hemodynamics and intraluminal thrombus deposition in abdominal aortic aneurysms. *American Journal of Physiology-Heart and Circulatory Physiology* 307(12), H1786-H1795. doi: 10.1152/ajpheart.00461.2014.
- Arzani, A. 2018. Accounting for residence-time in blood rheology models: do we really need non-Newtonian blood flow modelling in large arteries?. *J. R. Soc. Interface*, 15: 20180486. <http://dx.doi.org/10.1098/rsif.2018.0486>
- Bauer, A., Bopp, M., Jakirlic, S., Tropea, C., Krafft, A. J., Shokina, N., Hennig, J. 2020. Analysis of the wall shear stress in a generic aneurysm under pulsating and transitional flow conditions. *Exp. Fluids*, vol. 61, no. 2, pp. 1–16, doi: 10.1007/s00348-020-2901-4.
- Berger, S.A., and Jou, L.D. 2000. Flows in Stenotic Vessels. *Annual Review of Fluid Mechanics* 32(1), 347-382. doi: 10.1146/annurev.fluid.32.1.347.
- Bessonov, N., Simakov, A. S. S., Vassilevskii, Y., and Volpert, V. (2016). *Methods of Blood Flow Modelling*. vol. 11, no. 1, pp. 1–25, doi: 10.1051/mmnp/201611101.

- Biasseti, J., Hussain, F., and Gasser, T.C. 2011. Blood flow and coherent vortices in the normal and aneurysmatic aortas: a fluid dynamical approach to intraluminal thrombus formation. *Journal of The Royal Society Interface*.
- Biasseti, J., Spazzini, P. G., Swedenborg, J. and Christian Gasser, T. 2012. An integrated fluid-chemical model toward modeling the formation of intraluminal thrombus in abdominal aortic aneurysms. *Front. Physiol.*, vol. 3 JUL, no. July, pp. 1–16, doi: 10.3389/fphys.2012.00266.
- Bilgi, C. and Atalik, K. 2019. Numerical investigation of the effects of blood rheology and wall elasticity in abdominal aortic aneurysm under pulsatile flow conditions. *Biorheology*, vol. 56, no. 1, pp. 51–71, doi: 10.3233/BIR-180202.
- Bilgi, C. and Atalik, K. 2020. Effects of blood viscoelasticity on pulsatile hemodynamics in arterial aneurysms. *J. Nonnewton. Fluid Mech.*, vol. 279, no. July 2019, doi: 10.1016/j.jnnfm.2020.104263.
- Bit, A., Alblawi, A., Chattopadhyay, H., Quais, Q. A., Benim, A. C., Rahimi-Gorji, M., and Do, H. T. 2020. Three dimensional numerical analysis of hemodynamic of stenosed artery considering realistic outlet boundary conditions. *Comput. Methods Programs Biomed.*, vol. 185, p. 105163, doi: 10.1016/j.cmpb.2019.105163.
- Bodnár, T., Sequeira, A., and Prosi, M. (2011). On the shear-thinning and viscoelastic effects of blood flow under various flow rates. *Appl. Math. Comput.*, vol. 217, no. 11, pp. 5055–5067, doi: 10.1016/j.amc.2010.07.054.
- Boyd, A. J., Kuhn, D. C. S., Lozowy, R. J. and Kulbisky, G. P. 2016. Low wall shear stress predominates at sites of abdominal aortic aneurysm rupture. *J. Vasc. Surg.*, vol. 63, no. 6, pp. 1613–1619, doi: 10.1016/j.jvs.2015.01.040.
- Brewster, D.C., Cronenwett, J.L., Hallett, J.W., Johnston, K. W., Krupski, W. C. and Matsumura, J. S. 2003. Guidelines for the treatment of abdominal aortic aneurysms: Report of a subcommittee of the Joint Council of the American

- Association for Vascular Surgery and Society for Vascular Surgery. *J. Vasc. Surg.*, vol. 37, no. 5, pp. 1106–1117, doi: 10.1067/mva.2003.363.
- Canchi, T., Saxena, A., Ng, E.Y.K., Pwee, E.C.H., and Narayanan, S. 2018. Application of Fluid–Structure Interaction Methods to Estimate the Mechanics of Rupture in Asian Abdominal Aortic Aneurysms. *BioNanoScience* 8(4), 1035-1044. doi: 10.1007/s12668-018-0554-z.
- Campbell, I.C., Ries, J., Dhawan, S.S., Quyyumi, A. A., Taylor, W. R. and Oshinski, J. N. 2012. Effect of inlet velocity profiles on patient-specific computational fluid dynamics simulations of the carotid bifurcation. *J. Biomech. Eng.*, vol. 134, no. 5, pp. 1–8, doi: 10.1115/1.4006681.
- Chandra, S., Raut, S.S., Jana, A., Biederman, R.W., Doyle, M., Muluk, S.C., et al. 2013. Fluid-Structure Interaction Modeling of Abdominal Aortic Aneurysms: The Impact of Patient-Specific Inflow Conditions and Fluid/Solid Coupling. *Journal of Biomechanical Engineering* 135(8), 081001-081001-081014. doi: 10.1115/1.4024275.
- Chen, C.-Y., Antón, R., Hung, M.-y., Menon, P., Finol, E.A., and Pekkan, K. 2014. Effects of Intraluminal Thrombus on Patient-Specific Abdominal Aortic Aneurysm Hemodynamics via Stereoscopic Particle Image Velocity and Computational Fluid Dynamics Modeling. *Journal of Biomechanical Engineering* 136(3), 031001-031001-031009. doi: 10.1115/1.4026160.
- Chen, C.Y., Hung, M.Y., Finol, E.A., and Pekkan, K. 2015. Experimental and computational investigation of the patient-specific abdominal aortic aneurysm pressure field AU - Antón, R. *Computer Methods in Biomechanics and Biomedical Engineering* 18(9), 981-992. doi: 10.1080/10255842.2013.865024.
- Chen, Q., Zhong, Q., Qi, M. and Wang, X. 2015. Comparison of vortex identification criteria for planar velocity fields in wall turbulence. *Phys. Fluids*, vol. 27, no. 8, doi: 10.1063/1.4927647.

- Chen, X., Zhuang, J., and Wu, Y. 2020. The effect of Womersley number and particle radius on the accumulation of lipoproteins in the human aorta. *Comput. Methods Biomech. Biomed. Engin.*, vol. 23, no. 10, pp. 571–584, doi: 10.1080/10255842.2020.1752681.
- Cho, Y. I. and Kensey, K. R. 1991. Effects of the non-Newtonian viscosity of blood on flows in a diseased arterial vessel. Part 1: Steady flows. *Biorheology*, vol. 28, no. 3–4, pp. 241–262, doi: 10.3233/BIR-1991-283-415.
- Darling, R.C., Messina, C.R., Brewster, D.C., and Ottinger, L.W. 1977. Autopsy study of unoperated abdominal aortic aneurysms. The case for early resection. *Circulation* 56(3 Suppl), III161-164.
- Deplano, V., Guivier-Curien, C., and Bertrand, E. 2016. 3D analysis of vortical structures in an abdominal aortic aneurysm by stereoscopic PIV. *Experiments in Fluids* 57(11), 167. doi: 10.1007/s00348-016-2263-0.
- Deplano, V., Knapp, Y., Bertrand, E., and Gaillard, E. 2007. Flow behaviour in an asymmetric compliant experimental model for abdominal aortic aneurysm. *Journal of Biomechanics* 40(11), 2406-2413. doi: <https://doi.org/10.1016/j.jbiomech.2006.11.017>.
- Di Martino, E.S., and Vorp, D.A. 2003. Effect of Variation in Intraluminal Thrombus Constitutive Properties on Abdominal Aortic Aneurysm Wall Stress. *Annals of Biomedical Engineering* 31(7), 804-809. doi: 10.1114/1.1581880.
- Doyle, B.J., McGloughlin, T.M., Miller, K., Powell, J.T., and Norman, P.E. 2014. Regions of High Wall Stress Can Predict the Future Location of Rupture of Abdominal Aortic Aneurysm. *CardioVascular and Interventional Radiology* 37(3), 815-818. doi: 10.1007/s00270-014-0864-7.
- Drewe, C.J., Parker, L.P., Kelsey, L.J., Norman, P.E., Powell, J.T., and Doyle, B.J. 2017. Haemodynamics and stresses in abdominal aortic aneurysms: A fluid-structure interaction study into the effect of proximal neck and iliac

- bifurcation angle. *Journal of Biomechanics* 60, 150-156. doi: <https://doi.org/10.1016/j.jbiomech.2017.06.029>.
- Durst, F., Ray, S., Ünsal, B., and Bayoumi, O.A. 2005. The Development Lengths of Laminar Pipe and Channel Flows. *Journal of Fluids Engineering* 127(6), 1154-1160. doi: 10.1115/1.2063088.
- Elhanafy, A., Guaily, A. and Elsaid, A. 2019. Numerical simulation of Oldroyd-B fluid with application to hemodynamics. *Adv. Mech. Eng.*, vol. 11, no. 5, pp. 1–7, doi: 10.1177/1687814019852844.
- Epps, B.P. 2017. Review of vortex identification methods. *AIAA SciTech Forum - 55th AIAA Aerosp. Sci. Meet.*, no. January, pp. 1–22, doi: 10.2514/6.2017-0989.
- Egelhoff, C.J., Budwig, R.S., Elger, D.F., Khraishi, T.A., and Johansen, K.H. 1999. Model studies of the flow in abdominal aortic aneurysms during resting and exercise conditions. *Journal of Biomechanics* 32(12), 1319-1329. doi: [https://doi.org/10.1016/S0021-9290\(99\)00134-7](https://doi.org/10.1016/S0021-9290(99)00134-7).
- Faraji, A., Sahebi, M. and SalavatiDezfouli, S. 2022. Numerical investigation of different viscosity models on pulsatile blood flow of thoracic aortic aneurysm (TAA) in a patient-specific model. *Comput. Methods Biomech. Biomed. Engin.*, vol. 0, no. 0, pp. 1–13, doi: 10.1080/10255842.2022.2102423.
- Favero, J. L., Secchi, A. R., Cardozo, N. S. M. and Jasak, H. 2010. Viscoelastic flow analysis using the software OpenFOAM and differential constitutive equations. *J. Nonnewton. Fluid Mech.*, vol. 165, no. 23–24, pp. 1625–1636, doi: 10.1016/j.jnnfm.2010.08.010.
- Field, D.A. 1988. Laplacian smoothing and Delaunay triangulations. *Communications in Applied Numerical Methods* 4(6), 709-712. doi: 10.1002/cnm.1630040603.

- Finol, E.A. and Amon, C. H. 2001. Blood flow in abdominal aortic aneurysms: Pulsatile flow hemodynamics. *J. Biomech. Eng.*, vol. 123, no. 5, pp. 474–484, doi: 10.1115/1.1395573.
- Fillinger, M.F., Marra, S.P., Raghavan, M.L., and Kennedy, F.E. 2003. Prediction of rupture risk in abdominal aortic aneurysm during observation: Wall stress versus diameter. *Journal of Vascular Surgery* 37(4), 724-732. doi: <https://doi.org/10.1067/mva.2003.213>.
- Fillinger, M.F., Raghavan, M.L., Marra, S.P., Cronenwett, J.L., and Kennedy, F.E. 2002. In vivo analysis of mechanical wall stress and abdominal aortic aneurysm rupture risk. *Journal of Vascular Surgery* 36(3), 589-597. doi: <https://doi.org/10.1067/mva.2002.125478>.
- Fisher, C. and Rossmann, J. S. 2009. Effect of non-Newtonian behavior on hemodynamics of cerebral aneurysms. *J. Biomech. Eng.*, vol. 131, no. 9, pp. 1–9, doi: 10.1115/1.3148470.
- Fonken, J.H., Maas, E.J., Nievergeld, A.H., van Sambeek, M.R., van de Vosse, F.N., Lopata, R.G. Ultrasound-Based Fluid–Structure Interaction Modeling of Abdominal Aortic Aneurysms Incorporating Pre-stress. *Front. Physiol.* 2021, 12, 717593, <https://doi.org/10.3389/fphys.2021.717593>.
- Formaggia, L., Lamponi, D., and Quarteroni, A. 2003. One-dimensional models for blood flow in arteries. *Journal of Engineering Mathematics* 47(3), 251-276. doi: 10.1023/B:ENGL.0000007980.01347.29.
- Guranov, I., Čočić, A. and Lečić, M. 2013. Numerical Studies of Viscoelastic Flow Using the Software OpenFOAM. *Pamm*, vol. 13, no. 1, pp. 591–592, doi: 10.1002/pamm.201310276.
- Habla, F., Tan, M. W., Haßlberger, J. and Hinrichsen, O. 2014. Numerical simulation of the viscoelastic flow in a three-dimensional lid-driven cavity using the log-conformation reformulation in OpenFOAM®. *J. Nonnewton. Fluid Mech.*, vol. 212, pp. 47–62, doi: 10.1016/j.jnnfm.2014.08.005.

- Hoi, Y., Wasserman, B. A., Lakatta, E. G. and Steinman, D. A. 2010. Effect of common carotid artery inlet length on normal carotid bifurcation hemodynamics. *J. Biomech. Eng.*, vol. 132, no. 12, pp. 1–14, doi: 10.1115/1.4002800.
- Hua, J., and Mower, W.R. 2001. Simple geometric characteristics fail to reliably predict abdominal aortic aneurysm wall stresses. *Journal of Vascular Surgery* 34(2), 308-315. doi: <https://doi.org/10.1067/mva.2001.114815>.
- Impiombato, A. N., La Civita, G., Orlandi, F., Franceschini Zinani, F. S., Oliveira Rocha, L. A. and Biserni, C. 2021. A Simple Transient Poiseuille-Based Approach to Mimic the Womersley Function and to Model Pulsatile Blood Flow. *Dynamics*, vol. 1, no. 1, pp. 9–17, doi: 10.3390/dynamics1010002.
- Javidi, M. and Hrymak, A. N. 2015. Numerical simulation of the dip-coating process with wall effects on the coating film thickness. *J. Coatings Technol. Res.*, vol. 12, no. 5, pp. 843–853, doi: 10.1007/s11998-015-9699-7.
- Jeong, J. and Hussain, F. 1995. On the identification of a vortex. *J. Fluid Mech.*, vol. 285, pp. 69–94, doi: 10.1017/S0022112095000462.
- Joly, F., Soulez, G., Lessard, S., Kauffmann, C., Vignon-Clementel, I. A Cohort Longitudinal study identifies morphology and hemodynamics predictors of abdominal aortic aneurysm growth. *Ann Biomed Eng* 2020;48:606-23, <https://doi.org/10.1016/j.combiomed.2017.10.033>.
- Juster, H. R., Distlbacher, T. and Steinbichler, G. 2014. Viscosity analysis of a polymer-based drug delivery system using open-source CFD methods and high-pressure capillary rheometry. *Int. Polym. Process.*, vol. 29, no. 5, pp. 570–578, doi: 10.3139/217.2892.
- Karimi, S., Dabagh, M., Vasava, P., Dadvar, M., Dabir, B. and Jalali, P. 2014. Effect of rheological models on the hemodynamics within human aorta: CFD study on CT image-based geometry. *J. Nonnewton. Fluid Mech.*, vol. 207, pp. 42–52, doi: 10.1016/j.jnnfm.2014.03.007.

- Kelsey, L.J., Powell, J.T., Norman, P.E., Miller, K., and Doyle, B.J. 2016. A comparison of hemodynamic metrics and intraluminal thrombus burden in a common iliac artery aneurysm. *International Journal for Numerical Methods in Biomedical Engineering* 33(5), e2821. doi: 10.1002/cnm.2821.
- Khanafer, K.M., Bull, J.L., Upchurch, G.R., and Berguer, R. 2007. Turbulence Significantly Increases Pressure and Fluid Shear Stress in an Aortic Aneurysm Model under Resting and Exercise Flow Conditions. *Annals of Vascular Surgery* 21(1), 67-74. doi: <https://doi.org/10.1016/j.avsg.2006.10.009>.
- Khanafer, K.M., Gadhoke, P., Berguer, R., and Bull, J.L. 2006. Modeling pulsatile flow in aortic aneurysms: effect of non-Newtonian properties of blood. *Biorheology* 43(5), 661-679.
- Kontopodis, N., Metaxa, E., Papaharilaou, Y., Tavlas, E., Tsetis, D., and Ioannou, C. 2014. Advancements in identifying biomechanical determinants for abdominal aortic aneurysm rupture. *Vascular* 23(1), 65-77. doi: 10.1177/1708538114532084.
- Ku, D.N., Glagov, S., Moore, J.E., and Zarins, C.K. 1989. Flow patterns in the abdominal aorta under simulated postprandial and exercise conditions: An experimental study. *Journal of Vascular Surgery* 9(2), 309-316. doi: [https://doi.org/10.1016/0741-5214\(89\)90051-7](https://doi.org/10.1016/0741-5214(89)90051-7).
- Lakatta, E.G. 2002. Age-associated Cardiovascular Changes in Health: Impact on Cardiovascular Disease in Older Persons. *Heart Failure Reviews* 7(1), 29-49. doi: 10.1023/A:1013797722156.
- Lee, S.W. and Steinman, D.A. 2007. On the relative importance of rheology for image-based CFD models of the carotid bifurcation. *J. Biomech. Eng.*, vol. 129, no. 2, pp. 273–278, doi: 10.1115/1.2540836.
- Les, A.S., Shadden, S.C., Figueroa, C.A., Park, J.M., Tedesco, M.M., Herfkens, R.J., et al. 2010. Quantification of Hemodynamics in Abdominal Aortic

Aneurysms During Rest and Exercise Using Magnetic Resonance Imaging and Computational Fluid Dynamics. *Annals of Biomedical Engineering* 38(4), 1288-1313. doi: 10.1007/s10439-010-9949-x.

Leuprecht, A., and Perktold, K. 2001. Computer simulation of non-newtonian effects on blood flow in large arteries. *Comput. Methods Biomech. Biomed. Engin.*, vol. 4, no. 2, pp. 149–163, doi: 10.1080/10255840008908002.

Li, Z. and Kleinstreuer, C. 2005. Blood flow and structure interactions in a stented abdominal aortic aneurysm model. *Med. Eng. Phys.*, vol. 27, no. 5, pp. 369–382, doi: 10.1016/j.medengphy.2004.12.003.

Li, Z., and Kleinstreuer, C. 2007. A comparison between different asymmetric abdominal aortic aneurysm morphologies employing computational fluid–structure interaction analysis. *European Journal of Mechanics - B/Fluids* 26(5), 615-631. doi: <https://doi.org/10.1016/j.euromechflu.2007.03.003>.

Lodi Rizzini, M., Gallo, D., De Nisco, G., D’ascenzo, F., Chiastra, C., Bocchino, P. P., Piroli, F., De Ferrari, G. and Morbiducci, U. 2020. Does the inflow velocity profile influence physiologically relevant flow patterns in computational hemodynamic models of left anterior descending coronary artery?. *Med. Eng. Phys.*, vol. 82, pp. 58–69, doi: 10.1016/j.medengphy.2020.07.001.

Longo, C., and Upchurch, G.R. 2005. Abdominal Aortic Aneurysm Screening: Recommendations and Controversies. *Vascular and Endovascular Surgery* 39(3), 213-219. doi: 10.1177/153857440503900301.

Maazioui, S., Kissami, I., Benkhaldoun, F., Maazouz, A. and Ouazar, D. 2021. Concentrated Phosphate Slurry Flow Simulations Using OpenFoam. *Proc. Int. Conf. Ind. Eng. Oper. Manag.*, pp. 1843–1852.

Madhavan, S. and Kemmerling, E.M.C. 2018. The effect of inlet and outlet boundary conditions in image-based CFD modeling of aortic flow. *Biomed. Eng. Online*, vol. 17, no. 1, pp. 1–20, doi: 10.1186/s12938-018-0497-1.

- McGloughlin Timothy, M., and Doyle Barry, J. 2010. New Approaches to Abdominal Aortic Aneurysm Rupture Risk Assessment. *Arteriosclerosis, Thrombosis, and Vascular Biology* 30(9), 1687-1694. doi: 10.1161/ATVBAHA.110.204529.
- Mendieta, J. B., Fontanarosa, D., Wand, J., Paritala, P. K., McGahan, T., Lloyd, T. and Li, Z. 2020. The importance of blood rheology in patient-specific computational fluid dynamics simulation of stenotic carotid arteries. *Biomech. Model. Mechanobiol.*, vol. 19, no. 5, pp. 1477–1490, doi: 10.1007/s10237-019-01282-7.
- Meyer, C.A., Bertrand, E., Boiron, O., and Deplano, V. 2011. Stereoscopically Observed Deformations of a Compliant Abdominal Aortic Aneurysm Model. *Journal of Biomechanical Engineering* 133(11), 111004-111004-111008. doi: 10.1115/1.4005416.
- Mohamied, Y., Rowland, E.M., Bailey, E.L., Sherwin, S.J., Schwartz, M.A., and Weinberg, P.D. 2015. Change of Direction in the Biomechanics of Atherosclerosis. *Annals of Biomedical Engineering* 43(1), 16-25. doi: 10.1007/s10439-014-1095-4.
- Moore, J.J.E., and Ku, D.N. 1994. Pulsatile Velocity Measurements in a Model of the Human Abdominal Aorta Under Simulated Exercise and Postprandial Conditions. *Journal of Biomechanical Engineering* 116(1), 107-111. doi: 10.1115/1.2895692.
- Morbiducci, U. , Gallo, D., Massai, D., Ponzini, R., Deriu, M.A., Antiga, L., Redaelli, A. and Montevvecchi, F.M. 2011. On the importance of blood rheology for bulk flow in hemodynamic models of the carotid bifurcation. *J. Biomech.*, vol. 44, no. 13, pp. 2427–2438, doi: 10.1016/j.jbiomech.2011.06.028.
- Morris, L., Delassus, P., Grace, P., Wallis, F., Walsh, M. and McGloughlin, T. 2006. Effects of flat, parabolic and realistic steady flow inlet profiles on idealised

and realistic stent graft fits through Abdominal Aortic Aneurysms (AAA). *Med. Eng. Phys.*, vol. 28, no. 1 SPEC. ISS., pp. 19–26, doi: 10.1016/j.medengphy.2005.04.012.

Mower, W.R., Quiñones, W.J., and Gambhir, S.S. 1997. Effect of intraluminal thrombus on abdominal aortic aneurysm wall stress. *Journal of Vascular Surgery* 26(4), 602-608. doi: [https://doi.org/10.1016/S0741-5214\(97\)70058-2](https://doi.org/10.1016/S0741-5214(97)70058-2).

Najjari, M.R., and Plesniak, M.W. 2016. Evolution of vortical structures in a curved artery model with non-Newtonian blood-analog fluid under pulsatile inflow conditions. *Experiments in Fluids* 57(6), 100. doi: 10.1007/s00348-016-2188-7.

Ohtaroglu, O. 2020. Experimental investigation of physiological flow in abdominal aortic aneurysm. METU.

“OpenFOAM 8,” OpenFOAM, 01-Sep-2020. [Online]. Available: <https://openfoam.org/version/8/>. [Accessed: 07-Jun-2022].

Owen, B., Lowe, C., Ashton, N., Mandal, P., Rogers, S., Wein, W., et al. 2016. Computational hemodynamics of abdominal aortic aneurysms: Three-dimensional ultrasound versus computed tomography. *Proceedings of the Institution of Mechanical Engineers, Part H: Journal of Engineering in Medicine* 230(3), 201-210. doi: 10.1177/0954411915626742.

Peattie, R.A., Asbury, C.L., Bluth, E.I., and Riehle, T.J. 1996. Steady flow in models of abdominal aortic aneurysms. Part II: Wall stresses and their implication for in vivo thrombosis and rupture. *Journal of Ultrasound in Medicine* 15(10), 689-696. doi: 10.7863/jum.1996.15.10.689.

Qiu, Y., Yuan, D., Wen, J., Fan, Y., and Zheng, T. 2018. Numerical identification of the rupture locations in patient-specific abdominal aortic aneurysms using hemodynamic parameters. *Computer Methods in Biomechanics and Biomedical Engineering* 21(1), 1-12. doi: 10.1080/10255842.2017.1410796.

- Pinto, S. I. S. and Campos, J. B. L. M. 2016. Numerical study of wall shear stress-based descriptors in the human left coronary artery. *Comput. Methods Biomech. Biomed. Engin.*, vol. 19, no. 13, pp. 1443–1455, doi: 10.1080/10255842.2016.1149575.
- Raghavan, M., Kratzberg, J., and da Silva, E.S.o. 2004. "Heterogeneous, Variable Wall-Thickness Modeling of a Ruptured Abdominal Aortic Aneurysm", in: *ASME International Mechanical Engineering Congress and Exposition*), 271-272.
- Raghavan, M.L., Vorp, D.A., Federle, M.P., Makaroun, M.S., and Webster, M.W. 2000. Wall stress distribution on three-dimensionally reconstructed models of human abdominal aortic aneurysm. *Journal of Vascular Surgery* 31(4), 760-769. doi: <https://doi.org/10.1067/mva.2000.103971>.
- Razavi, A., Shirani, E. and Sadeghi, M. R. 2011. Numerical simulation of blood pulsatile flow in a stenosed carotid artery using different rheological models. *J. Biomech.*, vol. 44, no. 11, pp. 2021–2030, doi: 10.1016/j.jbiomech.2011.04.023.
- Reza, M. M. S., A. Arzani. 2019. A critical comparison of different residence time measures in aneurysms. *J Biomech.* 88:122–9.
- Roloff, C., Berg, P., Redel, T., Janiga, G., and Thévenin, D. 2017. Tomographic particle image velocimetry for the validation of hemodynamic simulations in an intracranial aneurysm. in: *2017 39th Annual International Conference of the IEEE Engineering in Medicine and Biology Society (EMBC)*), 1340-1343.
- Roloff, C., Stucht, D., Beuing, O., and Berg, P. 2018. Comparison of intracranial aneurysm flow quantification techniques: standard PIV vs stereoscopic PIV vs tomographic PIV vs phase-contrast MRI vs CFD. *Journal of NeuroInterventional Surgery*, neurintsurg-2018-013921. doi: 10.1136/neurintsurg-2018-013921.

- Ryan, A.J., Brougham, C.M., Garcarena, C.D., Kerrigan, S.W., and O'Brien, F.J. 2016. Towards 3D in vitro models for the study of cardiovascular tissues and disease. *Drug Discovery Today* 21(9), 1437-1445. doi: <https://doi.org/10.1016/j.drudis.2016.04.014>.
- San, O. and Staples, A. E. 2012. An improved model for reduced-order physiological fluid flows. *J. Mech. Med. Biol.*, vol. 12, no. 3, doi: 10.1142/S0219519411004666.
- Saqr, K. M., Rashad, S., Tupin, S., Niizuma, K., Hassan, T., Tominaga, T. and Ohta, M. 2020. What does computational fluid dynamics tell us about intracranial aneurysms? A meta-analysis and critical review. *J. Cereb. Blood Flow Metab.*, vol. 40, no. 5, pp. 1021–1039, doi: 10.1177/0271678X19854640.
- Salman, H.E., Ramazanli, B., Yavuz, M.M. and Yalcin, H.C. 2019. Biomechanical Investigation of Disturbed Hemodynamics-Induced Tissue Degeneration in Abdominal Aortic Aneurysms Using Computational and Experimental Techniques. *Front. in Biotech and Bioeng.* vol. 7, no. May, pp. 1–27, doi: 10.3389/fbioe.2019.00111.
- Salsac, A.-V., Sparks, S.R., Chomaz, J.-M., and Lasheras, J.C. 2006. Evolution of the wall shear stresses during the progressive enlargement of symmetric abdominal aortic aneurysms. 560(august), 19-51. doi: 10.1017/s002211200600036x.
- Scott, R.A.P., Ashton, H.A., Lamparelli, M.J., Harris, G.J.C., and Stevens, J.W. 2002. A 14-year experience with 6 cm as a criterion for surgical treatment of abdominal aortic aneurysm. *BJS* 86(10), 1317-1321. doi: 10.1046/j.1365-2168.1999.01227.x.
- Scotti, C.M., Jimenez, J., Muluk, S.C., and Finol, E.A. 2008. Wall stress and flow dynamics in abdominal aortic aneurysms: finite element analysis vs. fluid–structure interaction. *Computer Methods in Biomechanics and Biomedical Engineering* 11(3), 301-322. doi: 10.1080/10255840701827412.

- Shibeshi, S. S. and Collins, W. E. 2005. The rheology of blood flow in a branched arterial system with three-dimensional model: A numerical study. *Appl. Rheol.*, vol. 25, no. 4, pp. 398–405, doi: 10.1017/s1727719100002951.
- Simão da Silva, E., Rodrigues, A.J., Magalhães Castro de Tolosa, E., Rodrigues, C.J., Villas Boas do Prado, G., and Nakamoto, J.C. 2000. Morphology and diameter of infrarenal aortic aneurysms: a prospective autopsy study. *Cardiovascular Surgery* 8(7), 526-532. doi: [https://doi.org/10.1016/S0967-2109\(00\)00060-0](https://doi.org/10.1016/S0967-2109(00)00060-0).
- Singh, J., Brunner, G., Morrisett, J. D., Ballantyne, C. M., Lumsden, A. B., Shah, D. J., Decuzzi, P. 2018. Patient-specific flow descriptors and normalised wall index in peripheral artery disease: a preliminary study. *Comput. Methods Biomech. Biomed. Eng. Imaging Vis.*, vol. 6, no. 2, pp. 119–127, doi: 10.1080/21681163.2016.1184589.
- Skiadopoulos, A., Neofytou, P. and Housiadas, C. 2017. Comparison of blood rheological models in patient specific cardiovascular system simulations. *J. Hydrodyn.*, vol. 29, no. 2, pp. 293–304, doi: 10.1016/S1001-6058(16)60739-4.
- Smith, C. R. C. 2018. *Introduction to Graduate Fluid Mechanics*.
- Soudah, E., Ng, E.Y.K., Loong, T.H., Bordone, M., Pua, U., and Narayanan, S. 2013. CFD modelling of abdominal aortic aneurysm on hemodynamic loads using a realistic geometry with CT. *Computational and mathematical methods in medicine* 2013, 472564-472564. doi: 10.1155/2013/472564.
- Soulis, J. V., Giannoglou, G. D., Chatzizisis, Y. S., Seralidou, K. V., Parcharidis, G. E. and G. E. Louridas. 2008. Non-Newtonian models for molecular viscosity and wall shear stress in a 3D reconstructed human left coronary artery. *Med. Eng. Phys.*, vol. 30, no. 1, pp. 9–19, doi: 10.1016/j.medengphy.2007.02.001.
- Stamatopoulos, C., Papaharilaou, Y., Mathioulakis, D.S., and Katsamouris, A. 2010. Steady and unsteady flow within an axisymmetric tube dilatation.

- Experimental Thermal and Fluid Science 34(7), 915-927. doi: <https://doi.org/10.1016/j.expthermflusci.2010.02.008>.
- Stringfellow, M.M., Lawrence, P.F., and Stringfellow, R.G. 1987. The influence of aorta-aneurysm geometry upon stress in the aneurysm wall. *Journal of Surgical Research* 42(4), 425-433. doi: 10.1016/0022-4804(87)90178-8.
- Swedenborg, J., and Eriksson, P.E.R. 2006. The Intraluminal Thrombus as a Source of Proteolytic Activity. *Annals of the New York Academy of Sciences* 1085(1), 133-138. doi: 10.1196/annals.1383.044.
- Tanweer, O., Wilson, T.A., Metaxa, E., Riina, H.A., and Meng, H. 2014. A Comparative Review of the Hemodynamics and Pathogenesis of Cerebral and Abdominal Aortic Aneurysms: Lessons to Learn From Each Other. *J Cerebrovasc Endovasc Neurosurg* 16(4), 335-349.
- Taubin, G. 1995. Curve and surface smoothing without shrinkage. in: *Proceedings of IEEE International Conference on Computer Vision*, 852-857.
- van 't Veer, M., Buth, J., Merckx, M., Tonino, P., van den Bosch, H., Pijls, N., et al. 2008. Biomechanical properties of abdominal aortic aneurysms assessed by simultaneously measured pressure and volume changes in humans. *Journal of Vascular Surgery* 48(6), 1401-1407. doi: <https://doi.org/10.1016/j.jvs.2008.06.060>.
- Vollmer, J., Mencl, R., and Müller, H. 2001. Improved Laplacian Smoothing of Noisy Surface Meshes. *Computer Graphics Forum* 18(3), 131-138. doi: 10.1111/1467-8659.00334.
- Vorp, D.A., Raghavan, M.L., Muluk, S.C., Makaroun, M.S., Steed, D.L., Shapiro, R.O.N., et al. 1996. Wall Strength and Stiffness of Aneurysmal and Nonaneurysmal Abdominal Aorta. *Annals of the New York Academy of Sciences* 800(1), 274-276. doi: 10.1111/j.1749-6632.1996.tb33330.x.

- Vorp, D.A., Raghavan, M.L., and Webster, M.W. 1998. Mechanical wall stress in abdominal aortic aneurysm: Influence of diameter and asymmetry. *Journal of Vascular Surgery* 27(4), 632-639. doi: [https://doi.org/10.1016/S0741-5214\(98\)70227-7](https://doi.org/10.1016/S0741-5214(98)70227-7).
- Vorp, D.A., Vande Geest, J.P. 2005. Biomechanical determinants of abdominal aortic aneurysm rupture. *Arterioscler Thromb Vasc Biol.* Aug;25(8):1558-66. doi: 10.1161/01.ATV.0000174129.77391.55. PMID: 16055757.
- Vorp, D.A. 2007. Biomechanics of abdominal aortic Aneurysm. *Journal of Biomechanics*, 40(9),1887-1902, doi: <https://doi.org/10.1016/j.jbiomech.2006.09.003>.
- Wang, Y., Joannic, D., patrick, j., Keromnes, A., Aurélien, M., Lalande, A., et al. 2016. Comparison of Flow Measurement by 4D Flow Magnetic Resonance Imaging and by Particles Image Velocimetry on Phantom of Abdominal Aortic Aneurysm. *SM Vascular Medicine*.
- Wei, Z.A., Huddleston, C., Trusty, P.M., Singh-Gryzbon, S., Fogel, M.A., Veneziani, A. and Yoganathan, A. P. 2019. Analysis of Inlet Velocity Profiles in Numerical Assessment of Fontan Hemodynamics. *Ann. Biomed. Eng.*, vol. 47, no. 11, pp. 2258–2270, doi: 10.1007/s10439-019-02307-z.
- Wolters, B.J.B.M., Rutten, M.C.M., Schurink, G.W.H., Kose, U., de Hart, J., and van de Vosse, F.N. 2005. A patient-specific computational model of fluid–structure interaction in abdominal aortic aneurysms. *Medical Engineering & Physics* 27(10), 871-883. doi: <https://doi.org/10.1016/j.medengphy.2005.06.008>.
- Womersley, J.R. 1955. Method for the calculation of velocity, rate of flow and viscous drag in arteries when the pressure gradient is known. *The Journal of Physiology* 127(3), 553-563. doi: 10.1113/jphysiol.1955.sp005276.
- Xenos, M., Alemu, Y., Zamfir, D., Einav, S., Ricotta, J.J., Labropoulos, N., et al. 2010. The effect of angulation in abdominal aortic aneurysms: fluid–structure

- interaction simulations of idealized geometries. *Medical & Biological Engineering & Computing* 48(12), 1175-1190. doi: 10.1007/s11517-010-0714-y.
- Yip, T.H., and Yu, S.C.M. 2002. Oscillatory flows in straight tubes with an axisymmetric bulge. *Experimental Thermal and Fluid Science* 26(8), 947-961. doi: [https://doi.org/10.1016/S0894-1777\(02\)00214-5](https://doi.org/10.1016/S0894-1777(02)00214-5).
- Young, D.F. 1979. Fluid Mechanics of Arterial Stenoses. *Journal of Biomechanical Engineering* 101(3), 157-175. doi: 10.1115/1.3426241.
- Youssefi, P., Gomez, A., Arthurs, C., Sharma, R., Jahangiri, M. and Figueroa, C. A. 2018. Impact of patient-specific inflow velocity profile on hemodynamics of the thoracic aorta. *J. Biomech. Eng.*, vol. 140, no. 1, doi: 10.1115/1.4037857.
- Yu, S.C.M. 2000. Steady and pulsatile flow studies in Abdominal Aortic Aneurysm models using Particle Image Velocimetry. *International Journal of Heat and Fluid Flow* 21(1), 74-83. doi: [https://doi.org/10.1016/S0142-727X\(99\)00058-2](https://doi.org/10.1016/S0142-727X(99)00058-2).
- Zheng, E. Z., Rudman, M., Singh, J. and Kuang, S. B. 2019. Direct numerical simulation of turbulent non-Newtonian flow using OpenFOAM. *Appl. Math. Model.*, vol. 72, pp. 50–67, doi: 10.1016/j.apm.2019.03.003.
- Zhou, J., Adrian, R.J., Balachandar, S., and Kendall, T.M. 1999. Mechanisms for generating coherent packets of hairpin vortices in channel flow. *Journal of Fluid Mechanics* 387, 353-396. doi: 10.1017/S002211209900467X.

APPENDICES

APPENDIX A

Womersley Velocity Profile Boundary Condition with OpenFoam

Over several decades, intense research on physiologic flow inside the arteries have been performed. At 1955, Womersley [1] derived the exact solution of incompressible, Newtonian fluid flow through a cylindrical and rigid blood vessel, in which a pressure gradient which is periodic function of time drives the flow, by using the equations of motion and continuity. Assuming the motion is laminar, axisymmetric, and parallel to the longitudinal axis of the tube in addition to the vessel is horizontal, and gravitation has no effect on the flow, the Navier-Stokes equations, and the equation of continuity are simplified to the following under the conditions named above:

$$\frac{\partial u}{\partial x} = 0 \quad (\text{A. 1})$$

$$0 = -\frac{\partial p}{\partial r} \quad (\text{A. 2})$$

$$0 = -\frac{\partial p}{\partial \theta} \quad (\text{A. 3})$$

$$\rho \frac{\partial u}{\partial t} = -\frac{\partial p}{\partial x} + \mu \left(\frac{\partial^2 u}{\partial r^2} + \frac{1}{r} \frac{\partial u}{\partial r} \right) \quad (\text{A. 4})$$

The boundary conditions are the axisymmetric condition at the center and no-slip on the wall, at radius R:

$$\frac{\partial u}{\partial r} = 0 \quad \text{at } r = 0 \quad (\text{A. 5})$$

$$u = 0 \quad \text{at } r = R \quad (\text{A. 6})$$

Here p is for pressure, x , r and θ are cylindrical polar coordinates with x in the axial and r in the radial direction, u is the velocity component in the direction of x , and t is time. According to Eqs. (A.2) and (A.3), p is a function of x and t only. According to (A.4), u is a function of r and t . On differentiating Eq. (A.4) with respect to 'x', one obtains

$$\frac{\partial}{\partial x} \left(\frac{\partial p}{\partial x} \right) = 0 \quad (\text{A. 7})$$

This shows that the pressure gradient must not vary with x . It can be a function of t . For simplicity, the form of the pressure gradient will be taken as a simple harmonic motion and written in complex form:

$$\frac{\partial p}{\partial x} = Ae^{i\omega t} \quad (\text{A. 8})$$

On substituting into Eq. (A.4), one obtains

$$\rho \frac{\partial u}{\partial t} = -Ae^{i\omega t} + \mu \left(\frac{\partial^2 u}{\partial r^2} + \frac{1}{r} \frac{\partial u}{\partial r} \right) \quad (\text{A. 9})$$

After solving Eqn (A.9) in accordance with the stated boundary conditions, one can obtain

$$u(r, t) = \frac{A}{i\omega\rho} \left[1 - \frac{J_0 \left(\alpha \frac{r}{R} i^{3/2} \right)}{J_0(\alpha i^{3/2})} \right] e^{i\omega t} \quad (\text{A. 10})$$

where ν is kinematic viscosity and α is a dimensionless quantity known as the Womersley number

$$\alpha = R \sqrt{\frac{\omega}{\nu}} \quad (\text{A. 11})$$

If the flow rate inside the blood vessel is known, the term A can also be determined from the given formula

$$Q = 2\pi \int_0^R u r dr \quad (\text{A. 12})$$

Substituting the u in Eqn (A.10) to flow rate integral and writing $y = r/R$,

$$Q = \frac{2\pi A}{i\omega\rho} \left(\frac{R^2}{2} - \frac{R^2}{J_0(\alpha i^{3/2})} \int_0^1 J_0(\alpha y i^{3/2}) y dy \right) e^{i\omega t} \quad (\text{A. 13})$$

From known properties of Bessel functions, $\int x J_0(x) dx = x J_1(x)$, therefore

$$Q = \frac{\pi R^2 A}{i\omega\rho} \left(1 - \frac{2\alpha i^{3/2} J_1(\alpha i^{3/2})}{i^3 a^2 J_0(\alpha i^{3/2})} \right) e^{i\omega t} \quad (\text{A. 14})$$

To find u , it is necessary to write the flow rate and u on the same harmonic form. Assuming the flow rate is also a harmonic function and substituting into Eqn (A.14)

$$Q = \sum_{n=0}^N C_n e^{in\omega t} \quad (\text{A. 15})$$

$$\sum_{n=0}^N C_n e^{in\omega t} = \sum_{n=0}^N \frac{\pi R^2 A_n}{i\omega_n \rho} \left(1 - \frac{2\alpha_n i^{3/2} J_1(\alpha_n i^{3/2})}{i^3 a_n^2 J_0(\alpha_n i^{3/2})} \right) e^{i\omega_n t} \quad (\text{A. 16})$$

After canceling out $e^{i\omega t}$, A_n becomes

$$A_n = \frac{C_n i \omega_n \rho}{\pi R^2 \left(1 - \frac{2J_1 \left(i^{\frac{3}{2}} \alpha_n \right)}{i^{\frac{3}{2}} \alpha_n J_0 \left(i^{\frac{3}{2}} \alpha_n \right)} \right)} \quad (\text{A. 17})$$

To determine A_n , a Fourier series decomposition of the flow rate waveform should be performed to obtain Fourier coefficients (which is C_n in that case). For that purpose, Fast Fourier Transform (FFT) method can be applied to the available flow rate data. After determining C_n , $u(r, t)$ can be calculated from following formula

$$u(r, t) = \sum_{n=0}^N \frac{C_n}{\pi R^2 \left(1 - \frac{2J_1 \left(i^{\frac{3}{2}} \alpha_n \right)}{i^{\frac{3}{2}} \alpha_n J_0 \left(i^{\frac{3}{2}} \alpha_n \right)} \right)} \left[1 - \frac{J_0 \left(\alpha_n \frac{r}{R} i^{3/2} \right)}{J_0 \left(\alpha_n i^{3/2} \right)} \right] e^{i\omega_n t} \quad (\text{A. 18})$$

where the term $n = 0$ corresponds to a steady pressure gradient, which is actually simple Poiseuille's flow

$$u(r, t) = \frac{2C_0}{\pi R^2} \left(1 - \left(\frac{r}{R} \right)^2 \right) + \sum_{n=1}^N \frac{C_n}{\pi R^2 \left(1 - \frac{2J_1 \left(i^{\frac{3}{2}} \alpha_n \right)}{i^{\frac{3}{2}} \alpha_n J_0 \left(i^{\frac{3}{2}} \alpha_n \right)} \right)} \left[1 - \frac{J_0 \left(\alpha_n \frac{r}{R} i^{3/2} \right)}{J_0 \left(\alpha_n i^{3/2} \right)} \right] e^{i\omega_n t} \quad (\text{A. 19})$$

C_0 and C_n 's are the FFT coefficients of flow waveform. The process is written on Matlab and velocity profiles are obtained. The code is given below.

```

% This script finds the velocity profiles inside a blood vessel for
a given
% flow rate waveform. First it reads the flow rate data from a txt
file and
% then finds the Fourier series coefficients by using FFT method.
Finally,
% by using those coefficients, velocity profile at different time
values
% are found by solving Womersley's equation.
% 04.10.2021, Burcu Ramazanlı

clear all; close all; clc;

R = 0.009; % Radius of vessel (m)
rho = 1000; % Density of working fluid (kg/m^3)
nu = 0.00000345; % Kinematic viscosity (m^2/s)
T = 1; % Period of the waveform (s)

f = dlmread('wave_values.txt', '\t');
%t = f(:,1);
f_k = f(:,2); % Flow rate values from txt file
(m^3/s)

interval= T/70;
t=0:interval:T-interval;
t=transpose(t); % Time instants corresponding to those
flow rates

% Now that we have the flow rate waveform, convert to fft and back
% to get Fourier coefficients, need to multiply fft coefficients by
2/N
% and then divide the DC coefficient by 2

N = size(t); N = N(1);
Cn = 2*fft(f_k)/N(:,1); % Fourier coefficients, obtained from
FFT
Cn(1) = Cn(1)/2; % DC coefficient (or, a0)

omega = 2*pi/T;
i = sqrt(-1);
ii = i^(3/2);

% Turn the signal back to time domain to see if it's correct
% Use it to check how many terms of the FT (Fourier modes) is
needed to
% reproduce the waveform accurately.

waveform_f = zeros(70,1);
for n = 1:35 % number of Fourier modes to include

```

```

    % waveform_f = waveform_f + real(Cn(n)*exp(i*omega*(n-1)*t));
    waveform_f = waveform_f + real(Cn(n))*cos(2*pi*(n-1)*t/T) -
    imag(Cn(n))*sin(2*pi*(n-1)*t/T);

end

figure(1); plot(t, f_k); hold on;
plot(t, waveform_f, 'r'); legend('f_k', 'waveform_f'); grid on;

x = linspace(0,R,N);
t = linspace(0,T,N);
u = zeros(70);

% Now insert Fourier coefficients to the Womersley's velocity
profile
% equation
for k = 1:N

    for y = 1:N

        r = x(y);
        u(y,k) = ((2*real(Cn(1)))/(pi*(R^2)))*(1-((r/R)^2)); % Cn(1)
is actually C0

        for n = 1:35

            a_n = R*sqrt(n*omega/nu);
            J0 = besselj(0, (a_n*(r/R))*ii);
            J0_c = besselj(0, (a_n*ii));
            J1_c = besselj(1, (a_n*ii));
            J = (1-(2/(a_n*ii))*(J1_c/J0_c));
            Kn(n) = Cn(n+1)/(pi*(R^2)*J);
            u(y,k) = u(y,k) + real(Kn(n)*(1-
(J0/J0_c))*exp(i*omega*n*t(k)));

        end

    end

end

figure(2); plot(u, x); grid on;

```

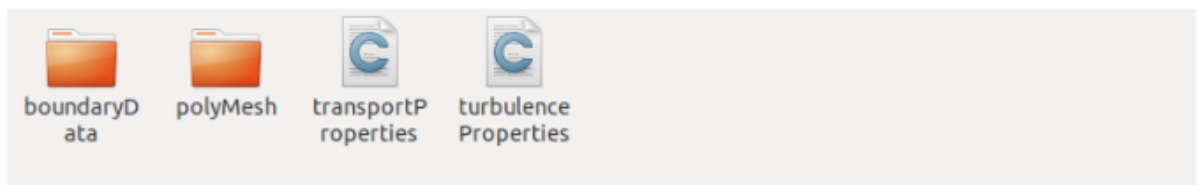

How to implement the obtained velocity profiles to OpenFOAM?

OpenFoam has a boundary condition called `timeVaryingMappedFixedValue`. To apply this condition, a bunch of files describing the points where you want to specify data in addition to the data at those points for specific times during your simulation should be generated. All of these files are stored in the constant directory of the case set up. OpenFOAM will then interpolate in space over time to transition from one set of data to the next when the case is running. A tutorial, which takes advantage of this boundary condition, is shipped with OpenFOAM. It can be found under `tutorials/incompressible/simpleFoam/pitzDailyExptInlet/`.

Let `inlet` be the name of the patch for which the inflow fields are generated. Then the following entry should be found in the U file.

```
inlet
{
    type            timeVaryingMappedFixedValue;
    offset          (0 0 0);
    setAverage      off;
    perturb         0;
}
```

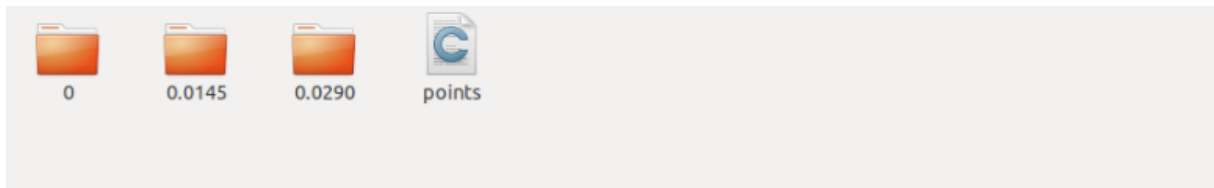
Then, a folder called `boundaryData` should be created under the constant directory.



The `boundaryData` folder should contain a sub-folder called with the name of the patch for which boundary condition is generated. In our case, let its name be `inlet`. Inside on this sub-folder, following should be placed

- points file
- time folders containing U files at those times.

The time folders should be named as the time of which velocity data is stored (for example, for zero time, it should be 0, like below picture).



[1] Womersley, J.R. Method for the calculation of velocity, rate of flow and viscous drag in arteries when the pressure gradient is known. *J. Physiol.* 1955, 127, 553–563.

APPENDIX B

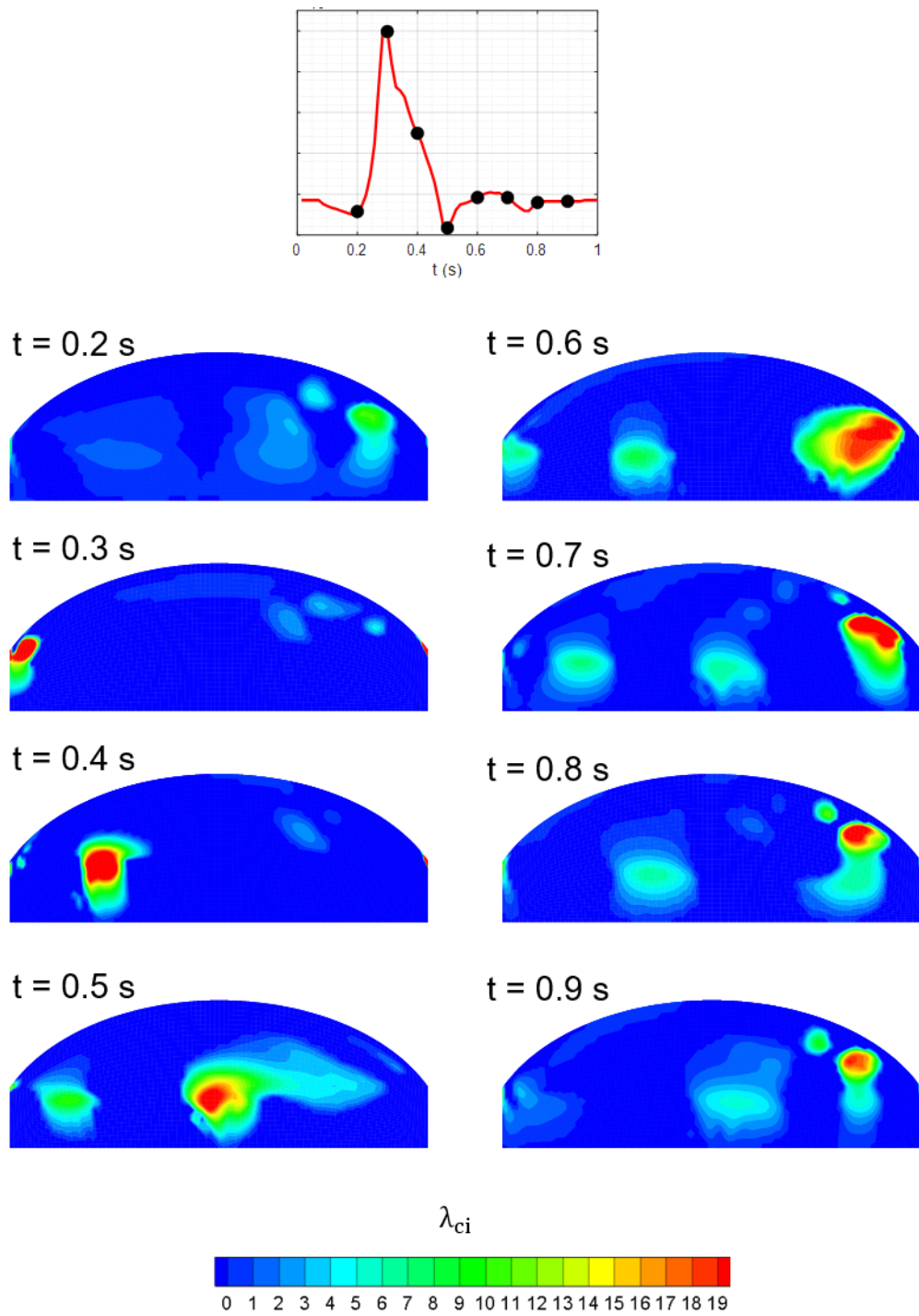


Figure B.1. Temporal evolution of swirling strength for Model 1 and $Re_m = 670$

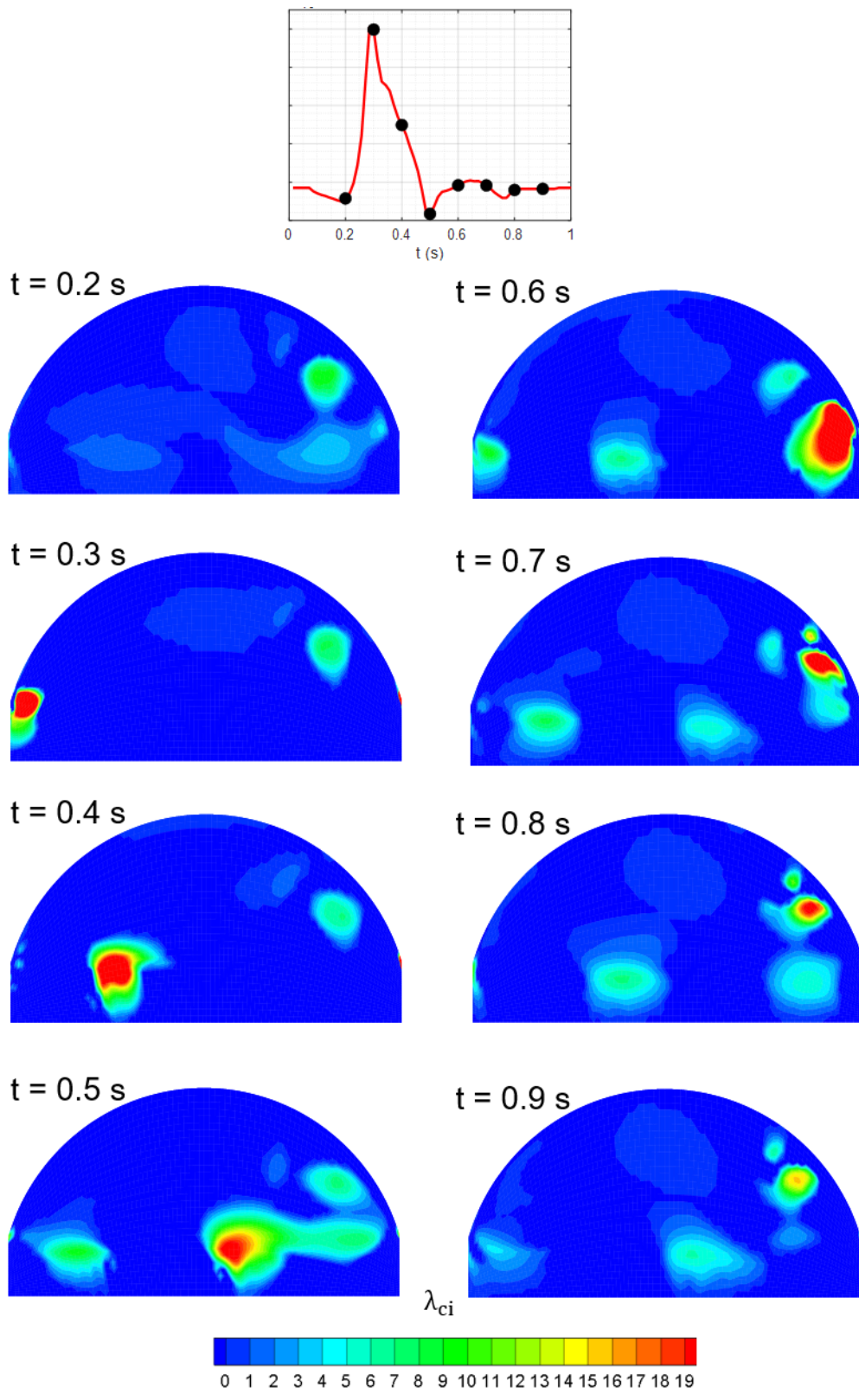


Figure B.2. Temporal evolution of swirling strength for Model 2 and $Re_m = 670$

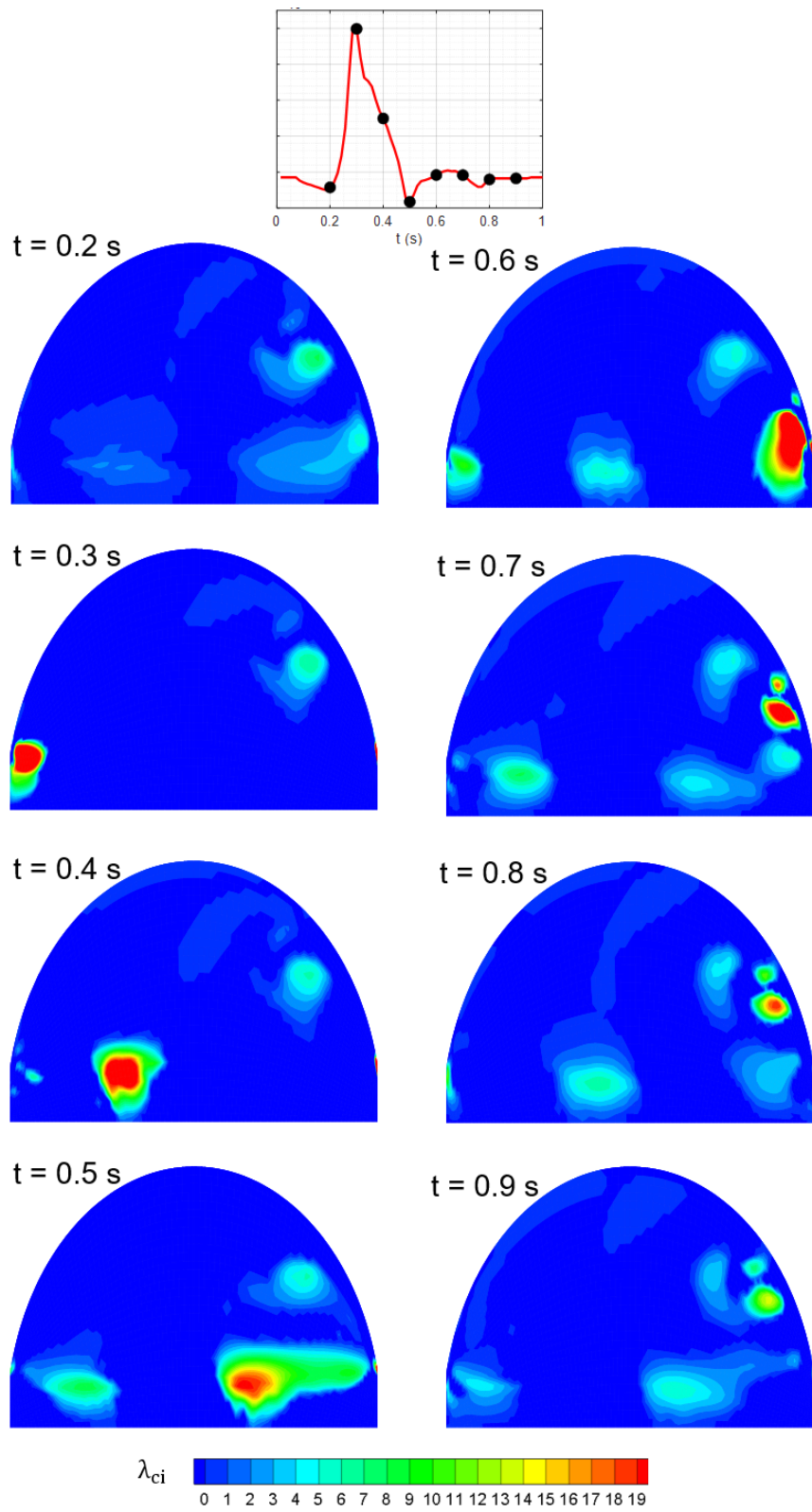


Figure B.3. Temporal evolution of swirling strength for Model 3 and $Re_m = 670$

APPENDIX C

Vortex Identification Methods

In literature, different vortex identification methods have been proposed. The most well-known vortex identification methods are Q-criterion, Δ -criterion, λ_2 -criterion and λ_{ci} -criterion. All of those methods require different requirements to define a vortex. Q-criterion, Δ -criterion, and λ_{ci} -criterion are called as velocity gradient based vortex identification criteria, while λ_2 -criterion utilizes local pressure minimum to define a vortex.

Velocity gradient tensor $\mathbf{D} = \nabla \vec{u}$ can be partitioned into symmetric and antisymmetric parts

$$\mathbf{D} = \mathbf{S} + \mathbf{\Omega} \quad (\text{C. 1})$$

$$\mathbf{S} = 1/2[\mathbf{D} + \mathbf{D}^T] \quad (\text{C. 2})$$

$$\mathbf{\Omega} = 1/2[\mathbf{D} - \mathbf{D}^T] \quad (\text{C. 3})$$

which are called the strain rate tensor, \mathbf{S} , and the angular rotation rate tensor, $\mathbf{\Omega}$. The trajectory of a fluid particle can be determined by solving the differential equation

$$\frac{d\vec{y}}{dt} = \mathbf{D} \cdot \vec{y} \quad (\text{C. 4})$$

with an initial condition $y(0) = y_0$. Eigendecomposition of the above ordinary differential equation can be written as

$$\mathbf{D} = \mathbf{V}\mathbf{\Lambda}\mathbf{V}^{-1} \quad (\text{C. 5})$$

where the columns of \mathbf{V} are eigenvectors v_i , and the diagonal of $\mathbf{\Lambda}$ gives the eigenvalues λ_i . The general solution of above equation is

$$y(t) = v_1 \exp(\lambda_1 t) c_1 + v_2 \exp(\lambda_2 t) c_2 + v_3 \exp(\lambda_3 t) c_3 \quad (\text{C. 6})$$

where constants c_i are determined from initial condition. According to the above equation, if all eigenvalues are real, then the point obtained is called as a node or a saddle. However, if one of the eigenvalues is real but the other two are complex conjugates, the point obtained become a focus, with closed or spiraling streamline trajectories, which is an indication of vortex.

To find the eigenvalues of diagonal, characteristic equation can be solved

$$\det \left[\frac{\partial u_i}{\partial x_j} - \lambda I \right] = 0 \quad (\text{C. 7})$$

which obtains

$$\lambda^3 + P\lambda^2 + Q\lambda + R = 0 \quad (\text{C. 8})$$

$$P = -\text{tr}(\mathbf{D}) \quad (\text{C. 9})$$

$$Q = \frac{1}{2}([\text{tr}(\mathbf{D})]^2 - \text{tr}(\mathbf{D}^2)) = \frac{1}{2}([\text{tr}(\mathbf{D})]^2 + \|\mathbf{\Omega}\|^2 - \|\mathbf{S}\|^2) \quad (\text{C. 10})$$

$$R = -\det(\mathbf{D}) = \frac{1}{3}(-P^3 + 3PQ - \text{tr}(\mathbf{D}^3)) \quad (\text{C. 11})$$

where P, Q and R are invariants of the velocity gradient tensor. For an incompressible flow, $tr(\mathbf{D})$ is zero. The discriminant of the characteristic equation gives an idea whether the eigenvalues are real or complex, which can be written as

$$\Delta = (Q/3)^3 + (R/2)^2 \quad (\text{C. 12})$$

If $\Delta \geq 0$, one eigenvalue is real, and the other two eigenvalues are complex conjugates, which indicates the swirling flow having a spiraling or closed streamline pattern, and this is called as Δ -criterion. Actually, Chong et al. stated that,

“a vortex core is a region of space where the vorticity is sufficiently strong to cause the rate-of-strain tensor to be dominated by the rotation tensor, i.e., the rate-of-deformation tensor has complex eigenvalues”

which is called as the Q-criterion to define a vortex, but it is nearly equal to Δ -criterion. Q is the second invariant of the velocity gradient tensor, and for an incompressible flow, it is written as

$$Q = \frac{1}{2} (\|\boldsymbol{\Omega}\|^2 - \|\mathbf{S}\|^2) > 0 \quad (\text{C. 13})$$

For a 2D flow, velocity gradient tensor diminishes to

$$\frac{\partial u_i}{\partial x_j} = \begin{bmatrix} \frac{\partial u}{\partial x} & \frac{\partial u}{\partial y} \\ \frac{\partial v}{\partial x} & \frac{\partial v}{\partial y} \end{bmatrix} \quad (\text{C. 14})$$

The strain rate tensor, \mathbf{S} , and the angular rotation rate tensor, $\mathbf{\Omega}$, for a 2D flow can be written as

$$\mathbf{\Omega} = \frac{1}{2} \begin{bmatrix} 0 & \frac{\partial u}{\partial y} - \frac{\partial v}{\partial x} \\ \frac{\partial v}{\partial x} - \frac{\partial u}{\partial y} & 0 \end{bmatrix} \quad (\text{C. 15})$$

$$\mathbf{S} = \frac{1}{2} \begin{bmatrix} 2 \frac{\partial u}{\partial x} & \frac{\partial u}{\partial y} + \frac{\partial v}{\partial x} \\ \frac{\partial v}{\partial x} + \frac{\partial u}{\partial y} & 2 \frac{\partial v}{\partial y} \end{bmatrix} \quad (\text{C. 16})$$

$$\|\mathbf{\Omega}\|^2 = \frac{1}{2} \left(\frac{\partial u}{\partial y} \right)^2 + \frac{1}{2} \left(\frac{\partial v}{\partial x} \right)^2 - \frac{\partial u}{\partial y} \frac{\partial v}{\partial x} \quad (\text{C. 17})$$

$$\|\mathbf{S}\|^2 = \frac{1}{2} \left(\frac{\partial u}{\partial y} \right)^2 + \frac{1}{2} \left(\frac{\partial v}{\partial x} \right)^2 + \frac{\partial u}{\partial y} \frac{\partial v}{\partial x} + \left(\frac{\partial u}{\partial x} \right)^2 + \left(\frac{\partial v}{\partial y} \right)^2 \quad (\text{C. 18})$$

Inserting these values to definition of Q-criterion gives

$$Q = \frac{1}{2} (\|\mathbf{\Omega}\|^2 - \|\mathbf{S}\|^2) = -\frac{\partial u}{\partial y} \frac{\partial v}{\partial x} - \frac{1}{2} \left(\frac{\partial u}{\partial x} \right)^2 - \frac{1}{2} \left(\frac{\partial v}{\partial y} \right)^2 > 0 \quad (\text{C. 19})$$

Zhou et al. (1999) also utilized the complex eigenvalue of the velocity gradient tensor to visualize vortices. For that purpose, they decompose velocity gradient tensor with the help of diagonalization by using eigenvalues and eigenvectors in the following manner

$$\frac{\partial u_i}{\partial x_j} = \begin{bmatrix} v_r & v_{cr} & v_{ci} \end{bmatrix} \begin{bmatrix} \lambda_r & 0 & 0 \\ 0 & \lambda_{cr} & \lambda_{ci} \\ 0 & -\lambda_{ci} & \lambda_{cr} \end{bmatrix} \begin{bmatrix} v_r & v_{cr} & v_{ci} \end{bmatrix}^{-1} \quad (\text{C. 20})$$

where λ_r is the real eigenvalue with as corresponding real eigenvector v_r , and $\lambda_{cr} \pm \lambda_{ci}i$ are the conjugate pair of the complex eigenvalues with complex eigenvectors $v_{cr} \pm v_{ci}i$. The local streamlines can be expressed in a local coordinate as

$$y_1(t) = C_r \exp(\lambda_r t) \quad (\text{C. 21})$$

$$y_2(t) = \exp(\lambda_{cr} t [C_c^1 \cos(\lambda_{ci} t) + C_c^2 \sin(\lambda_{ci} t)]) \quad (\text{C. 22})$$

$$y_3(t) = \exp(\lambda_{cr} t [C_c^2 \cos(\lambda_{ci} t) - C_c^1 \sin(\lambda_{ci} t)]) \quad (\text{C. 23})$$

where C_r , C_c^1 and C_c^2 are constants and can be determined from initial conditions. Along the axis of eigenvector v_r , flow is either stretched or compressed, while flow is swirling on the plane of eigenvectors v_{cr} and v_{ci} . Hence, the imaginary parts, λ_{ci} , of complex eigenvalues might be evaluated as a vortex indicator, and connected regions having non-zero λ_{ci} can be specified as vortex structures. The complex eigenvector, λ_{ci} , is known as strength of the swirling motion and it is called as the swirling strength of a vortex.

λ_2 -criterion based on local pressure minimum across a vortex core. Jeong and Hussain (1995) derived a transport equation for the strain rate tensor by taking gradient of the incompressible Navier Stokes equation, and obtain the symmetric part as following

$$\frac{d\mathbf{S}}{dt} + \nu \nabla^2 \mathbf{S} + \mathbf{S}^2 + \mathbf{\Omega}^2 = -\frac{1}{\rho} \nabla(\nabla P) \quad (\text{C. 24})$$

The term at the right hand side is called as pressure Hessian matrix. According to λ_2 -criterion, the vortex core is located to the local pressure minimum, except in the presence of unsteady and viscous effects. Therefore, by neglecting the rate of change of irrotational straining and viscous effects, pressure Hessian can be found as

$$\mathbf{S}^2 + \mathbf{\Omega}^2 \approx -\frac{1}{\rho} \nabla(\nabla P) \quad (\text{C. 25})$$

Local pressure minimum can be obtained where the pressure Hessian has two positive eigenvalues, which requires $S^2 + \Omega^2$ term has two negative eigenvalues. In 3D flows, ordering the eigenvalues of this matrix should satisfy the two of them must be negative inside a vortex core

$$\lambda_1 \leq \lambda_2 \leq \lambda_3 \quad \& \quad \lambda_2 < 0 \quad (\text{C. 26})$$

In 2D flows, $\lambda_1 \leq \lambda_2$ should be two eigenvalues of the matrix. According to λ_2 -criterion, λ_2 must be negative, which identifies connected vortex zones. For 2D flows, λ_2 -criterion can be written in the following form

$$\begin{aligned} \lambda_2 &= \left(\frac{\partial u}{\partial y} \frac{\partial v}{\partial x} - \frac{\partial u}{\partial x} \frac{\partial v}{\partial y} \right) + \frac{1}{2} \left(\frac{\partial u}{\partial x} + \frac{\partial v}{\partial y} \right)^2 \\ &+ \frac{1}{2} \left| \frac{\partial u}{\partial x} + \frac{\partial v}{\partial y} \right| \sqrt{\left(\frac{\partial u}{\partial x} + \frac{\partial v}{\partial y} \right)^2 + \left(\frac{\partial u}{\partial y} + \frac{\partial v}{\partial x} \right)^2} \\ &< 0 \end{aligned} \quad (\text{C. 27})$$

Overall, for 2D axisymmetric flows, Q -criterion, λ_{ci} -criterion and λ_2 -criterion can be written in the following form

$$Q = -\frac{\partial u_r}{\partial x} \frac{\partial u_x}{\partial r} - \frac{1}{2} \left(\frac{\partial u_r}{\partial r} \right)^2 - \frac{1}{2} \left(\frac{\partial u_x}{\partial x} \right)^2 > 0 \quad (\text{C. 28})$$

$$\lambda_{ci} = \frac{1}{2} \sqrt{-4 \frac{\partial u_r}{\partial x} \frac{\partial u_x}{\partial r} - \left(\frac{\partial u_x}{\partial x} - \frac{\partial u_r}{\partial r} \right)^2} > 0 \quad (\text{C. 29})$$

$$\lambda_2 = \frac{\partial u_r}{\partial x} \frac{\partial u_x}{\partial r} + \frac{1}{2} \left[\left(\frac{\partial u_x}{\partial x} \right)^2 + \left(\frac{\partial u_r}{\partial r} \right)^2 \right. \\ \left. + \left| \frac{\partial u_x}{\partial x} + \frac{\partial u_r}{\partial r} \right| \sqrt{\left(\frac{\partial u_x}{\partial x} - \frac{\partial u_r}{\partial r} \right)^2 + \left(\frac{\partial u_r}{\partial x} + \frac{\partial u_x}{\partial r} \right)^2} \right] < 0 \quad (\text{C. 30})$$

B. P. Epps, "Review of vortex identification methods," AIAA SciTech Forum - 55th AIAA Aerosp. Sci. Meet., no. January, pp. 1–22, 2017, doi: 10.2514/6.2017-0989.

APPENDIX D

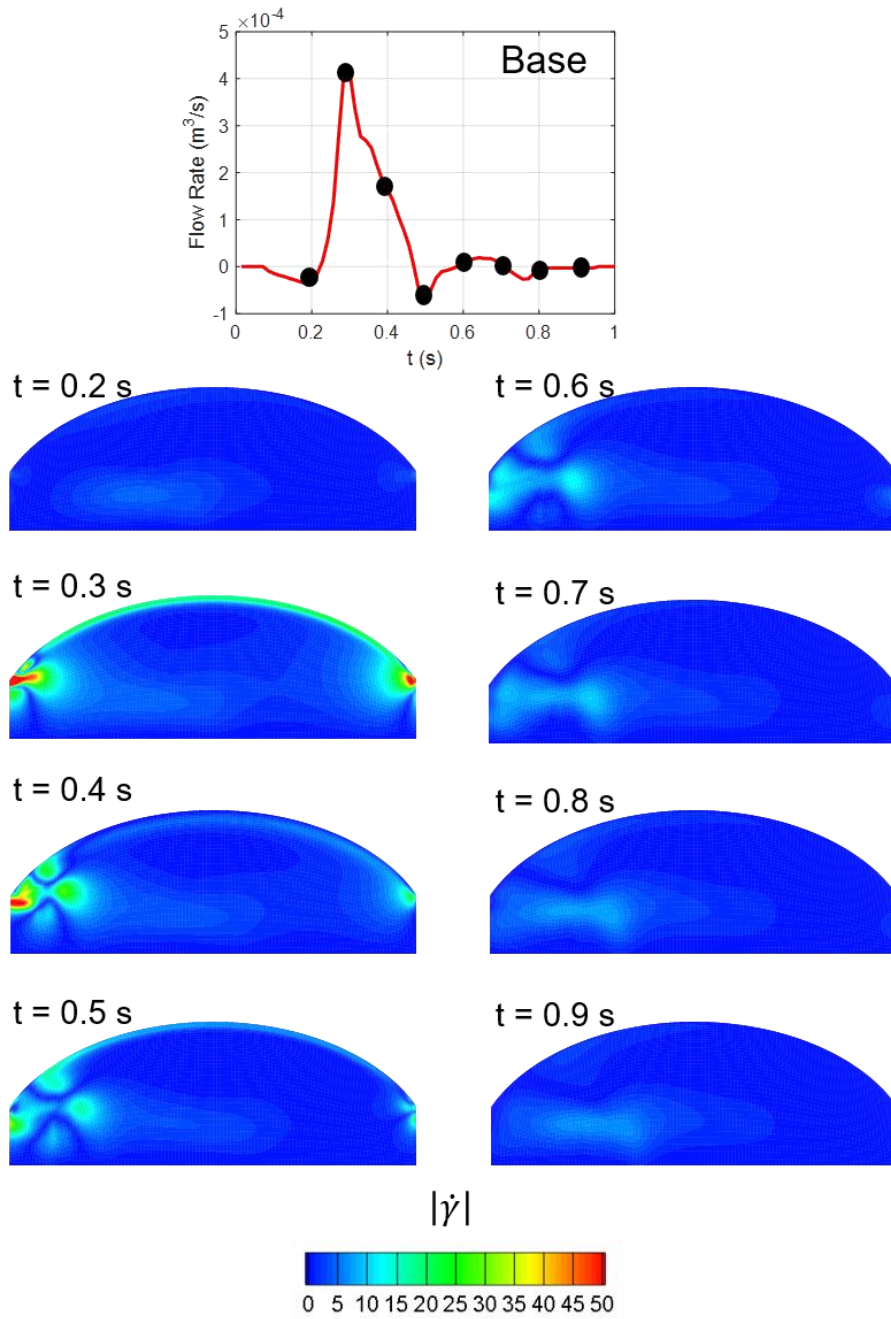


Figure D.4. Temporal evolution of shear rate for Base case

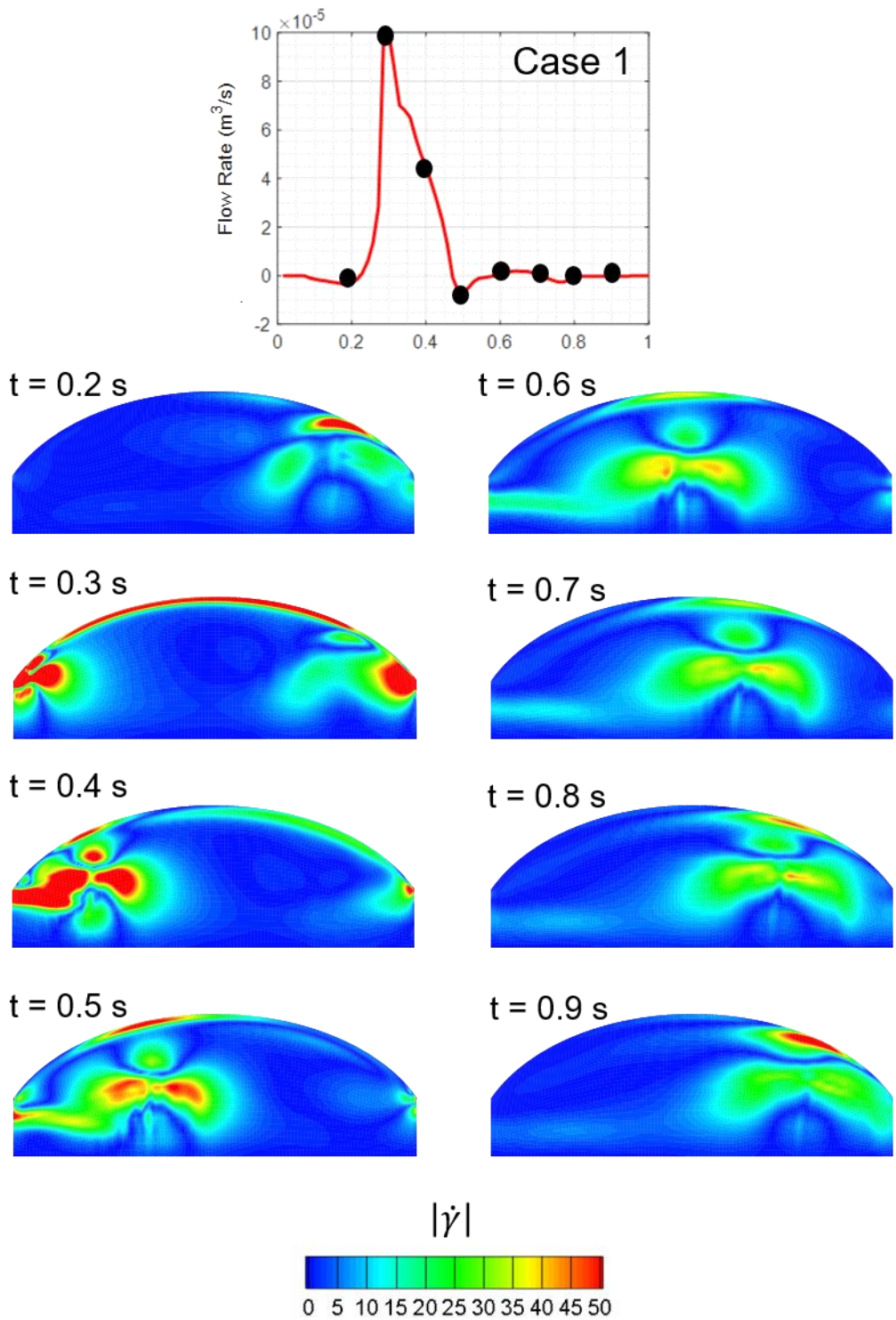


Figure D.5. Temporal evolution of shear rate for Case 1

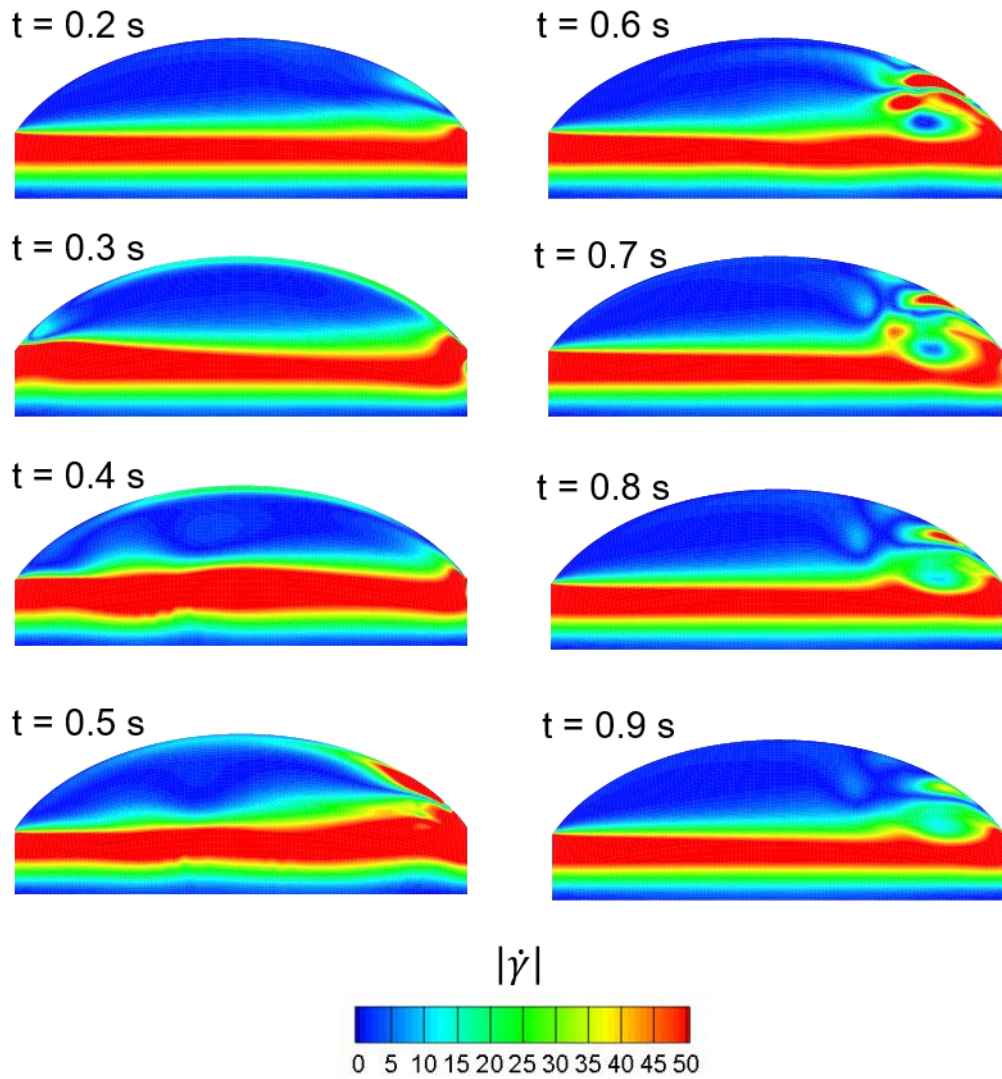
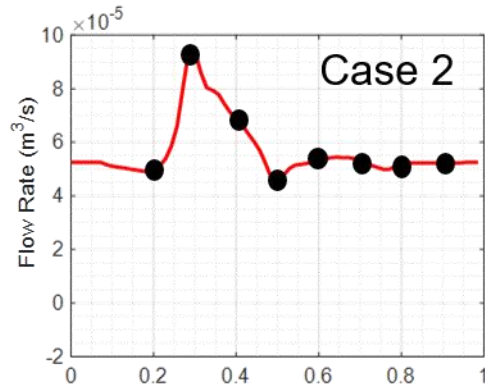


Figure D.6. Temporal evolution of shear rate for Case 2

CURRICULUM VITAE

Surname, Name : Ramazanlı, Burcu
Address: : Mechanical Eng. Dept., METU

EDUCATION

Degree	Institution	Year of Graduation
MS	METU Mechanical Engineering	2017
	<i>Control of flow structure on 45 degree swept delta wing using passive bleeding</i>	
BS	METU Mechanical Engineering	2014
High School	Meriç Anatolian High School, Bursa	2009
	<i>1st Ranking Student</i>	

FOREIGN LANGUAGES

Advanced English, Advanced Azerbaijani Language, Beginning French

JOURNAL PUBLICATIONS

1 - Salman, H.E., Ramazanlı, B., Yavuz, M. M., Yalcin, H. C., “Biomechanical Investigation of Disturbed Hemodynamics-Induced Tissue Degeneration in Abdominal Aortic Aneurysms Using Computational and Experimental Techniques,” *Front. In. Bioeng. and Biotech.*, vol. 7, no. May, pp. 1–27, 2019, doi: 10.3389/fbioe.2019.00111.

- 2 - Kestel, K., Ramazanlı, B., Yavuz, M. M., "Control of flow structure over a non-slender delta wing using passive bleeding," *Aerosp. Sci. Technol.*, vol. 106, p. 106136, 2020, doi: <https://doi.org/10.1016/j.ast.2020.106136>.
- 3 - Ramazanlı, B., Sert, C., Yavuz, M. M., "Correlation between vortex identification methods and wall shear stress parameters for flows inside aneurysms", *submitted to Int. J. Numer. Methods Biomed. Eng.*
- 4 - Ramazanlı, B., Yavuz, M. M., Sert, C., "Effect of Infrarenal Flow Waveform Pattern on Rheology Model Selection and Abdominal Aortic Aneurysm Hemodynamics" – *submitted to J. Non-Newton. Fluid Mech*
- 5 - Ramazanlı, B., Yavuz, M. M., Sert, C., "Effect of Inlet Velocity Profile and Entrance Length on Abdominal Aortic Aneurysm Hemodynamics Simulations" – *submitted to J. Therm. Sci. Technol.*

CONFERENCES

- 1 – Ramazanlı, B., Kestel, K., Yavuz, M. M., 2018, "Control of Three-dimensional Separation on Non-slender Delta Wings Using Passive Bleeding", 12th EFMC, Vienna, Austria.
- 2 – Yavuz, M. M., Ramazanlı, B., Kestel., K., 2018, "Control of Flow Structure on Non-slender Delta Wing using Passive Bleeding: Effects of Orientation, Angle, and Solidity Ratio", 71st APS, Atlanta, GA, US.
- 3 – Ramazanlı, B., Kestel, K., Yavuz, M. M., 2018, "Düşük ve Orta Ok Açılı Delta Kanatlar Üzerindeki Akışın Pasif Akıtma Yöntemi ile Kontrolü", 7th UHUK (National Aeronautical and Aerospace Conference), Samsun, Turkey.

WORK EXPERIENCE

1 - Teaching and Research Assistant at METU Mechanical Engineering Department from January 2016 to December 2022. Some of the courses assisted are: Fluid Mechanics I-II, Heat Transfer I-II, Thermodynamics I-II, Mechanical Engineering Systems Laboratory.

2 - Teaching Assistant at Turkish Aeronautical Association University Astronautical Engineering Department from October 2015 to January 2016. Some of the courses assisted are: Statics, Thermodynamics I-II.